Spectroscopic and Structural Properties of Galaxies in a Cluster Environment 5.3 Billion Years Ago

by

George Ridgeway

A Thesis Submitted to Saint Mary's University, Halifax, Nova Scotia in Partial Fulfillment
of the Requirements for the Degree of MSc in Astronomy
(Department of Astronomy and Physics)

August, 2023, Halifax, Nova Scotia

Approved: __________________________

Dr. Ivana Damjanov

Supervisor

Approved: __________________________

Dr. Marcin Sawicki

Committee Member

Approved: __________________________

Dr. Luigi Gallo

Examiner

Date: August 9th, 2023

Acknowledgements

Firstly, I would like to thank my supervisor, Dr. Ivana Damjanov, for her guidance throughout my research and for teaching me to become a better researcher. I extend my thanks to Dr. Jubee Sohn for providing information and measurements crucial to completing this project and to Dr. Percy Gomez and Dr. Sherry Yeh for their feedback and suggestions throughout the data reduction process. I would also like to thank all members of the extragalactic group for their valuable input.

I want to thank my committee members for providing constructive criticism to improve my final thesis. I would also like to thank my fellow graduate students for their support and camaraderie throughout these past two years.

I also would like to express how grateful I am for the lifelong friendships I have made in Halifax and for their support and encouragement throughout the past years. I would like to especially thank Meghan McLean for being my light, without her this thesis would have not been possible. Lastly, I would like to thank my parents for their constant support and encouragement.

Contents

List of Figures

List of Tables

Abstract

Spectroscopic and Structural Properties of Galaxies in a Cluster Environment 5.3 Billion Years Ago

by George Ridgeway

We study how environment affects the structural and spectroscopic properties of galaxies in a massive merging cluster at $z = 0.53$. We obtain follow up spectroscopic observations of the cluster, originally identified in the HectoMAP survey, and confirm an additional 25 galaxies as cluster members (increasing cluster membership by 78%). We calculate D_n4000, a proxy for galaxy stellar population age, for all cluster members. We perform a statistical correction using photometric cluster member candidates to account for missing spectroscopic members. We analyze the D_n4000 - clustercentric distance relation of the cluster and find that galaxies at all clustercentric distances have similarly aged stellar populations, implying a mixture of star forming and quiescent galaxies at all cluster radii. Using available measurements, we examine the size-stellar mass relation to find that non-star-forming cluster members and member candidates with $\log_{10}(M_*/M_\odot) > 10.5$ are, on average, larger in the cluster environment than in the field.

August 9, 2023

Author Contributions

The work presented in this thesis was a collaborative effort, with contributions from both the student author and collaborators. The division of contributions is outlined below:

Student Author (George Ridgeway):

- Reduced spectroscopic follow up observation of cluster HMRM 08268 (the focus of this thesis).
- Determined redshifts of objects in the follow up data and confirmed 25 new cluster members.
- Calculated D_n4000 for the 25 cluster members identified through follow up observations.
- Created catalog of photometric cluster member candidates and used them as a statistical correction.

Collaborator 1 (Dr. Ivana Damjanov):

- Collected follow up spectroscopic data of potential members of cluster HMRM 08268.
- Measured sizes for all spectroscopic members and photometric cluster member candidates.

Collaborator 2 (Dr. Jubee Sohn):

- Identified cluster HMRM 08268 in the HectoMap survey.
- Confirmed 32 spectroscopic cluster members.
- Measured stellar masses for all 57 spectroscopic cluster members.
- Calculated D_n4000 for the 32 original cluster members.

Chapter 1

INTRODUCTION

1.1 Formation of Structures in the ΛCDM Universe

Our current understanding of the Universe can be best described by the Lambda Cold Dark Matter (ΛCDM) model. This model has three main components: first, the cosmological constant Λ, also known as Einstein's cosmological constant (Einstein 1917), denotes the dark energy of the Universe; second, Cold Dark Matter denoted CDM; and third, baryonic matter (Spergel et al. 2003).

Einstein's cosmological constant, or dark energy, represents a component of the Universe that varies slowly with time and space (Peebles & Ratra 2003). Dark energy is responsible for the acceleration of the expansion of the Universe (Riess et al. 1998). One leading theory of what this component may be is the vacuum energy density (Ryden 2003). There are numerous astronomical proposals and observations that are attempting to further our understanding of dark energy (e.g. Dark Energy Survey Collaboration et al. 2016; DESI Collaboration et al. 2016). However, the true nature of dark energy is still currently unknown (Copeland et al. 2006; Li et al. 2011) even though it comprises $\approx 70\%$ of the Universe (Ryden 2003; Schneider 2006).

Dark matter is nonbaryonic matter that does not interact at all with electromagnetic radiation, rendering this form of matter completely invisible (Blumenthal et al. 1984; Davis et al. 1985; Navarro et al. 1996; Barkana 2018). We know that dark matter exists because we can detect it by measuring the orbital velocities of stars in spiral galaxies (Rubin 1983), the velocity dispersion of galaxy cluster members (Zwicky 1933), and through gravitational lensing (Zwicky 1937). The Universe consists of $\approx 25\%$ dark matter (Ryden 2003; Schneider 2006).

Dark matter particles are either cold or hot, where cold and hot refer to the thermal velocity of the dark matter particles approximately 12 years after the Big Bang. This timescale is chosen because that is when the mass within a Hubble volume is equal to $\approx\ 10^{12}M_{\odot}$, roughly the size of a large galaxy, which focuses on the seeds of structure formation (Peebles 1993; Ryden 2003; Weinberg 2008). Hot dark matter consists of particles that move at relativistic speeds long after $t = 12$ years. If the Universe consists primarily of hot dark matter, we would see large scale structures (such as clusters and superclusters) form first as a result of the free-streaming nature of hot dark matter (Schneider & Bartelmann 1995; Primack & Gross 2001; Barkana et al. 2001; Bennett et al. 2003; Schneider et al. 2013). However, we do not observe these large scale structures in the early Universe (e.g. Fan et al. 2003). Therefore, the dark matter content of the Universe must be primarily cold, or non-relativistic at $t = 12$ years. It is still uncertain as to what the nature of cold dark matter is, leading theories include Weakly Interacting Massive Particles (WIMPs) (e.g. Jungman et al. 1996; Pospelov et al. 2008; Arkani-Hamed et al. 2009) or theoretical elementary particles such as axions (e.g. Peccei & Quinn 1977; Kamionkowski 1998; Svrcek & Witten 2006; Kim & Carosi 2010). The main difference between WIMPs and axions is their mass. WIMPs are theorized to have masses on the order of GeV (Profumo et al. 2006; Archambault et al. 2012; Agnese et al. 2014), whereas axions are theorized to have masses below 10^{-4} eV (Turner 1986, 1988, 1990).

Lastly, baryonic matter consists of all of the matter that is composed of baryons or particles that are made up of three quarks. Baryonic matter includes protons and neutrons as well as electrons. Baryonic matter only accounts for $\approx 5\%$ of the Universe. These are the main components of the standard ΛCDM model. While there are some challenges to ΛCDM (e.g. Del Popolo & Le Delliou 2017; Perivolaropoulos & Skara 2022), there is no other cosmological model with more supporting evidence than ΛCDM (Planck Collaboration et al. 2020).

In the ΛCDM model, our Universe began with a Big Bang. This was initially a very dense and hot state that expanded rapidly, approximately 13.8 Gyr ago (Planck Collaboration et al. 2016). Since the Big Bang, the Universe has been expanding and cooling from these initial conditions. The elemental abundances (mainly hydrogen and helium) were set during the period of Big Bang Nucleosynthesis which lasted approximately 18 minutes (Fields et al. 2014). The Universe continued to expand and cool and after approximately 370,000 years since the Big Bang we begin to see the recombination of electrons and atomic nuclei, creating the first neutral atoms. At this time the Universe also became transparent to visible light and photons released by the decoupling of hydrogen and helium nuclei were able to travel freely (Ryden 2003; Schneider 2006; Sparke & Gallagher 2007; Hinshaw et al. 2009).

These photons, released billions of years ago, have been redshifted to microwave wavelengths and can now be seen as the Cosmic Microwave Background (CMB; Penzias & Wilson 1965). However, the CMB is not uniform and has small, but extremely relevant, anisotropies (Smoot et al. 1992). It is from these anisotropies that structure is able to form in the Universe. After the CMB photons are released the Universe enters a "dark age" until the first stars and subsequent galaxies form. During this time the Universe continues to expand and cool. While this is a very simplified explanation of the lengthy history of the Universe it serves as an important foundation for our future discussions.

ΛCDM is a relatively simple model in the sense that it can be described by six parameters. These parameters are as follows: dark energy density ($\Omega_{\Lambda,0} = 0.6911$), matter density ($\Omega_{m,0} = 0.3089$), baryon density ($\Omega_{b,0} = 0.0486$), fluctuation amplitude ($\sigma_8 = 0.8159$), scalar spectral index ($n_s = 0.9667$), and the dimensionless Hubble constant ($h = 0.6774$) (Planck Collaboration et al. 2016). With this model, we are able to better understand the early Universe as well as how large scale structure forms in the Universe. Throughout this thesis we assume the above presented ΛCDM cosmological model.

One of the fundamental assumptions in cosmology is that the Universe is both homogeneous and isotropic (Ryden 2003). We know this to be true on the largest cosmic scales $\approx 100 - 200$ Mpc (Guzzo 1997; Hogg et al. 2005). However, on scales smaller than $\approx 100 - 200$ Mpc, we do not observe a homogeneous and isotropic Universe. We see overdensities and underdensities of baryonic and dark matter in the form of galaxy clusters and voids, respectively. The large scale structure we see in the present Universe is thought to have grown gravitationally from extremely small density fluctuations (Blumenthal et al. 1984).

In the ΛCDM model, structure formation follows a hierarchical "bottom-up" scenario (Schneider 2006). In this formation history, small overdensities of dark matter (and subsequently baryonic matter) are able to overcome the expansion of the early Universe caused by dark energy (Λ) and collapse. The baryonic matter accumulates within the dark matter halos (Cole et al. 2000). The first dark matter halos are initially small but grow through mergers with other halos as the Universe evolves. Figure 1.1 shows a simplified diagram of these mergers. Looking from top to bottom, the initial dark matter halos are small, but over time they merge together to form larger and larger structures. It is through these mergers that the first galaxies, and subsequently galaxy clusters, are able to form.

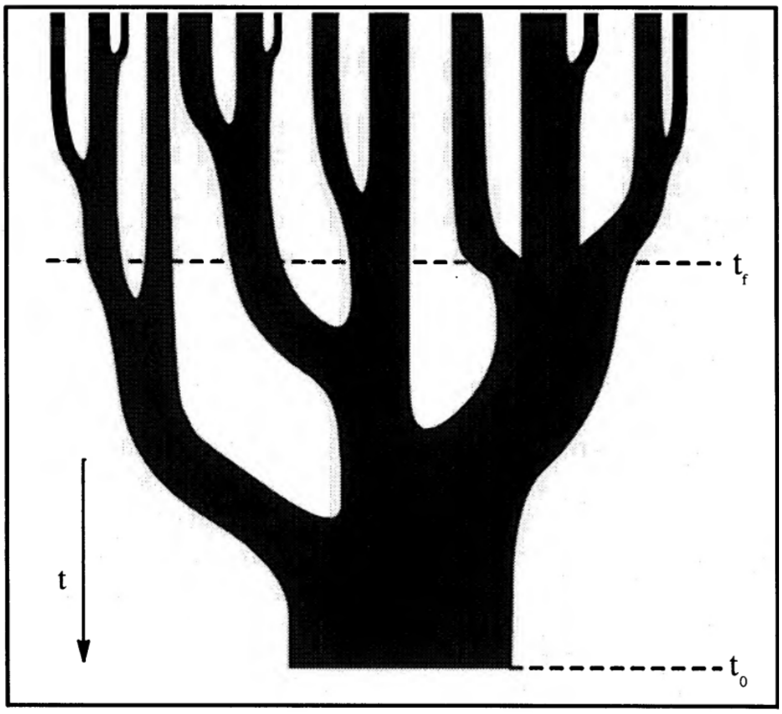

Figure 1.1: Merger Tree representing the hierarchical "bottom-up" structure formation adopted from (Lacey & Cole 1993). Time increases from top to bottom with t_0 being the present time and t_f the formation time, where the formation time is defined as the creation time of the parent halo containing at least half the mass of the final halo. We can see the initially small halos at the top merge together with each other and over time are able to form large scale structure that we observe today.

1.2 Galaxies and Galaxy Clusters

1.2.1 Galaxies

In the "bottom-up" formation scenario, the initial density perturbations result in the formation of dark matter halos where the first galaxies are able to form. Baryonic matter condenses and collapses into regions that are surrounded by dark matter halos (Larson et al. 1980; Blumenthal et al. 1984; Benson 2010). As this collapse occurs, the baryonic matter experiences shocks which increase the gas temperature (Evrard et al. 1994; Benson & Bower 2011). If the gas temperature were to remain virialized, we would not see any galaxy formation. Thus, various cooling processes take place (Mo et al. 2010). However, the dark matter particles do not experience the same shocks as baryonic matter. This is because dark matter is collisionless and does not interact with baryonic matter (e.g. White & Rees 1978; Blumenthal et al. 1984; Davis et al. 1985; Barkana 2018). At this point of galaxy formation, the dark matter and baryonic particles are still intermingled. As the gas cools it also starts to separate from the dark matter until there is cold dense gas in the middle of a dark matter halo. Regions within this gas cloud collapse under gravity and the first stars and galaxies are formed (e.g. White & Rees 1978; Blumenthal et al. 1984; Cole et al. 2000; Mo et al. 2010; Benson & Bower 2011).

In observations we see two distinct populations of galaxies, star forming and quiescent (Balogh et al. 2004b; Baldry et al. 2004; Menci et al. 2005; Mateus et al. 2006; Schneider 2006; Cassata et al. 2008; Whitaker et al. 2011). These two populations are identified by examining galaxy properties such as color (e.g. Strateva et al. 2001; Kauffmann et al. 2003; Blanton et al. 2003; Balogh et al. 2004b), morphology (e.g. de Vaucouleurs 1959; Dressler 1980; Conselice 1997), and star formation rate (e.g. Brinchmann et al. 2004; Balogh et al. 2004a).

Generally, star forming galaxies are rotationally supported flat systems (Mo et al. 2010). These galaxies typically have large fractions of molecular hydrogen and high star formation rates (Wong & Blitz 2002; Brinchmann et al. 2004; Feldmann et al. 2017). The stellar populations of star forming galaxies are dominated by young massive stars. These young massive stars output most of their flux at shorter (bluer) wavelengths. This results in star forming galaxies having a blue color (Blanton et al. 2003; Pecaut & Mamajek 2013). Conversely, quiescent galaxies are not rotationally supported and have minimal star formation occurring (Benson 2010). The low star formation is a result of quiescent galaxies containing very hot gas (T $\approx 10^7$ K), likely heated by AGN or stellar feedback (e.g. Mathews & Brighenti 2003; Croton et al. 2006; Bower et al. 2006; Ciotti et al. 2010; Conroy et al. 2015; Cheung et al. 2016; Li et al. 2020a,b). The stellar populations of quiescent galaxies primarily consist of older less massive stars. These older less massive stars output most of their flux at longer (redder) wavelengths. This results in quiescent galaxies having a red color (Balogh et al. 2004b; Thomas et al. 2010; Feldmann et al. 2017).

1.2.2 Intrinsic Properties of Galaxies

By observing the light emitted from a galaxy we are able to quantify a variety of intrinsic properties. In this thesis we focus on the size, mass, and stellar population age of galaxies that we are able to determine from photometric and spectroscopic measurements.

Using photometric data we can measure the size of a galaxy. The size, or effective radius, of a galaxy is defined as the radius in which half of a galaxy's luminosity is contained (Ryden 2003; Schneider 2006; Sparke & Gallagher 2007). The size of a galaxy can give us information on the assembly history as well as the dark matter halo (Shen et al. 2003a; van Dokkum et al. 2008; van der Wel et al. 2014). A galaxy's size is directly related to its surface brightness and morphological type (Kormendy 1977). In this work, the size of a galaxy is measured using 2D modeling of the galaxy's surface brightness (Damjanov et al. 2019). We discuss the size measurements of our galaxies in more detail in Section 2.4.

Photometric data is also used to measure the stellar mass of a galaxy. By fitting the galaxy's observed spectral energy distribution (SED), we can compare the observed fit to model SEDs and calculate the stellar mass (e.g. Tinsley 1968; Spinrad & Taylor 1971; Faber 1972; Bolzonella et al. 2000; Walcher et al. 2011; Mitchell et al. 2013; Mobasher et al. 2015; Lower et al. 2020). From the SED, we obtain the stellar mass-to-light ratio (M/L). It is generally assumed that the ratio of stellar mass-to-light is constant throughout a galaxy. However, this can prove to be an inaccurate assumption due to dark matter not contributing to the measured light (Marchesini et al. 2009; Conroy et al. 2009; Wilkins et al. 2013). Even with these discrepancies when measuring the mass of a galaxy, we can still obtain masses with reasonable uncertainties (Faber & Gallagher 1979; Gallazzi & Bell 2009; Mitchell et al. 2013). We discuss the stellar mass measurements for our galaxies in Section 2.3.1.

It has been shown that size evolution varies between star forming and quiescent galaxies. To understand this size evolution, we can examine the sizes of galaxies at a fixed stellar mass over a range of redshifts. The size-stellar mass relation of star forming galaxies can be described by a single power law for all masses (Shen et al. 2003a; Williams et al. 2010; van der Wel et al. 2014; Mowla et al. 2019a; George et al. in prep.). At higher redshifts ($z > 1$), star forming galaxies grow rapidly in size. However, at lower redshifts ($z < 1$), star forming galaxies are found to have little to no size evolution (Giavalisco et al. 1996; Lilly et al. 1998; Ferguson et al. 2004; Ravindranath et al. 2004; Barden et al. 2005; Oesch et al. 2010; Mosleh et al. 2012; van der Wel et al. 2014; Mowla et al. 2019a).

Conversely, observations show that quiescent galaxies at a fixed stellar mass of $\approx 10^{11} M_\odot$ have roughly doubled in size from $z = 1$ to $z = 0$ (Daddi et al. 2005; Trujillo et al. 2006; van der Wel et al. 2008, 2014; Damjanov et al. 2011; Huertas-Company et al. 2013; Mowla et al. 2019a). Quiescent galaxies also have a more complex size-stellar mass relation than star forming galaxies. Low mass quiescent galaxies ($\log_{10}(M_*/M_\odot) \leq$ 10.5), have a nearly flat size-stellar mass trend. However, high mass quiescent galaxies ($\log_{10}(M_*/M_\odot) \geq$ 10.5), have been found to have a strong, positive correlation between size and stellar mass (Shen et al. 2003a; Williams et al. 2010; van der Wel et al. 2014; Mowla et al. 2019a; George et al. in prep.).

Depending on the galaxy type (quiescent or star forming) and evolutionary history (e.g. mergers, tidal interactions), we will see differences in the growth of a galaxy's size (e.g. Conselice 2014; Sellwood 2014; Genel et al. 2018; Mowla et al. 2019b; Wilman et al. 2020). The size growth of star forming galaxies is theorized to be the result of star formation occurring throughout the galaxy (Mowla et al. 2019a). However, quiescent galaxies are theorized to grow in size primarily through mergers (White et al. 2007; McLure et al. 2013; van de Sande et al. 2013; van Dokkum et al. 2015). If a galaxy has had a major merger (Section 1.3), we will see a large increase in both the size and stellar mass of the resultant galaxy. However, minor mergers play a larger role in the size evolution of a galaxy than major mergers. This is due to the many minor mergers that a galaxy can experience throughout its existence. These minor mergers cause the outer radius to "puff up", resulting in a larger change in size for a small change in stellar mass (Bezanson et al. 2009; Naab et al. 2009; Nipoti et al. 2009; Newman et al. 2012; Faisst et al. 2017; Hamadouche et al. 2022; Damjanov et al. 2023). The "puffing up" of galaxies after minor mergers is the result of newly created material forming an envelope around the galaxy that continues to grow over time (Schweizer & Seitzer 1992; Naab et al. 2007).

With spectroscopic data, we use spectral indices as a proxy for the average stellar age of a galaxy. As a galaxy evolves over time, the stellar population within the galaxy also evolves. This change in the galaxy's stellar population is detected in the galaxy spectrum. In this thesis we measure the D_n4000 ratio (Balogh et al. 1999) of cluster member galaxies. D_n4000 is the spectral ratio of the red side (4000Å to 4100Å) to the blue side (3850Å to 3950Å) of a galaxy spectrum. It is centered around 4000Å due to the spectral break at that wavelength from metal absorption lines (Kim et al. 2022). The spectral break at 4000Å is caused by metal line blanketing of cooler (lower mass and older) stars. The metal line blanketing in the atmosphere cooler stars absorbs light at blue wavelengths (< 4000Å). However, hotter (higher mass and younger) stars ionize these metals, preventing them from absorbing light (Balogh et al. 1999; Kauffmann et al. 2003; Mendel et al. 2013). Because hotter stars move off the main sequence faster, we are able to trace the stellar population age of a galaxy by measuring the strength of the 4000Å break. A $D_n4000 <$ 1.5, indicates a younger, more recently formed ($<$ 1 Gyr) stellar population, whereas a $D_n4000 >$ 1.5, indicates an older ($>$ 1 Gyr) stellar population (Kauffmann et al. 2003). By measuring the D_n4000 of cluster galaxies we can better understand the evolution of galaxies within the cluster environment (Sohn et al. 2019).

1.2.3 Galaxy Clusters

The formation of galaxy clusters is a direct product of the hierarchical "bottom-up" formation structure. Galaxy clusters are formed from the gravitational collapse of rare primordial high density peaks (Rosati et al. 2002a). As a result of repeated merging of dark matter halos, galaxy clusters are the largest gravitationally bound structures in the Universe. With this hierarchical formation scenario in mind, we are able to produce simulations that closely resemble observations of galaxy clusters (e.g. Davis et al. 1985; Navarro et al. 1996, 1997; Springel et al. 2005; Schaye et al. 2015; Springel et al. 2018; Pillepich et al. 2018).

Figure 1.2 shows the simulated evolution of the dark matter density field through four redshift bins from $z = 3$ to $z = 0$. We can see that clusters form at the intersection of filaments within the cosmic web, the large-scale structure of the Universe. These filaments also continue to provide new material to the cluster. Clusters can contain tens to hundreds of galaxies, with the most massive clusters containing thousands of individual galaxies (e.g. Fisher et al. 1998; Romer et al. 1999; Ebeling et al. 2001; Böhringer et al. 2004; Stanford et al. 2005; Mei et al. 2007; Wilson et al. 2009; Cava et al. 2009; Rines et al. 2013; Knowles et al. 2022).

When examining the mass within a cluster, we assume a radius out to which we are able to state the cluster is in dynamical equilibrium or virialized. The mass contained out to the specified radius is known as the virial mass of the galaxy cluster. The most common radii used for clusters are R_{200} or R_{500}, where R_{200} and R_{500} represent the distance from the cluster center where the average density is 200 or 500 times the critical density at that redshift (Ryden 2003; Schneider 2006). Depending on the cluster radii, the virial mass of galaxy clusters can range from 10^{13} to 10^{15} $M_{\odot}$. However, only 10 - 15% of the total cluster mass is in the form of baryonic mass (Rosati et al. 2002a), the rest is dominated by dark matter. Of the baryonic mass only $\approx 2\%$ is associated with the stellar mass of galaxy cluster members (Chiu et al. 2016; Gonzalez et al.

2013; Sparke & Gallagher 2007; Ryden 2003; Schneider 2006). The other 13% is extremely hot gas (10^7 K) within the Intra Cluster Medium (ICM) (Mohr et al. 1999; Fouqué et al. 2001; Rosati et al. 2002b; Sparke & Gallagher 2007; Ryden 2003; Schneider 2006).

Most clusters contain a massive quiescent galaxy near the kinematic and gravitational center of the cluster (Abell 1965; Dubinski 1998; Lin & Mohr 2004; De Lucia & Blaizot 2007; O'Dea et al. 2008; Lauer et al. 2014). These Brightest Cluster Galaxies (BCG) are some of the most luminous and massive galaxies in the Universe. It is hypothesized that these massive galaxies have a formation history that is intimately intertwined with that of the cluster (e.g. Scott 1957; Hausman & Ostriker 1978; Geller & Postman 1983; Loh & Strauss 2006; Vale & Ostriker 2006). Early in the cluster's history, the BCG forms through mergers of several other massive galaxies (Dubinski 1998; De Lucia & Blaizot 2007). Typically, galaxy clusters will have a single BCG near the center of the gravitational potential. However, if a cluster has recently undergone a merger with another nearby cluster we may see two BCGs (Hatch et al. 2011; Lauer et al. 2014; Hung & Ebeling 2012; Sohn et al. 2019; Furnell et al. 2021).

An important property of galaxy clusters is the ICM. Not only does the ICM contain most of the baryonic mass of a cluster, it is also heated to temperatures so extreme that it emits strong X-ray radiation. Closer to the cluster center, the density of the gas increases. The cooling rate of a gas depends on the density of that gas, the more dense, the faster the gas cools. This process is known as radiative cooling and occurs due to the gas emitting thermal radiation (Fabian 1994, 2003). Therefore the center of clusters should be expected to host dense cool gas. With lots of dense cool gas, we should observe blue colored galaxies indicating active star formation. However, the star formation rates observed in the cluster center are lower by an order of magnitude compared to predictions (McNamara & O'Connell 1989; O'Dea et al. 2008; McDonald et al. 2011; Hoffer et al. 2012). It is now widely accepted that feedback from Active Galactic Nuclei (AGN) is reheating the ICM and preventing cooling and star formation within cluster

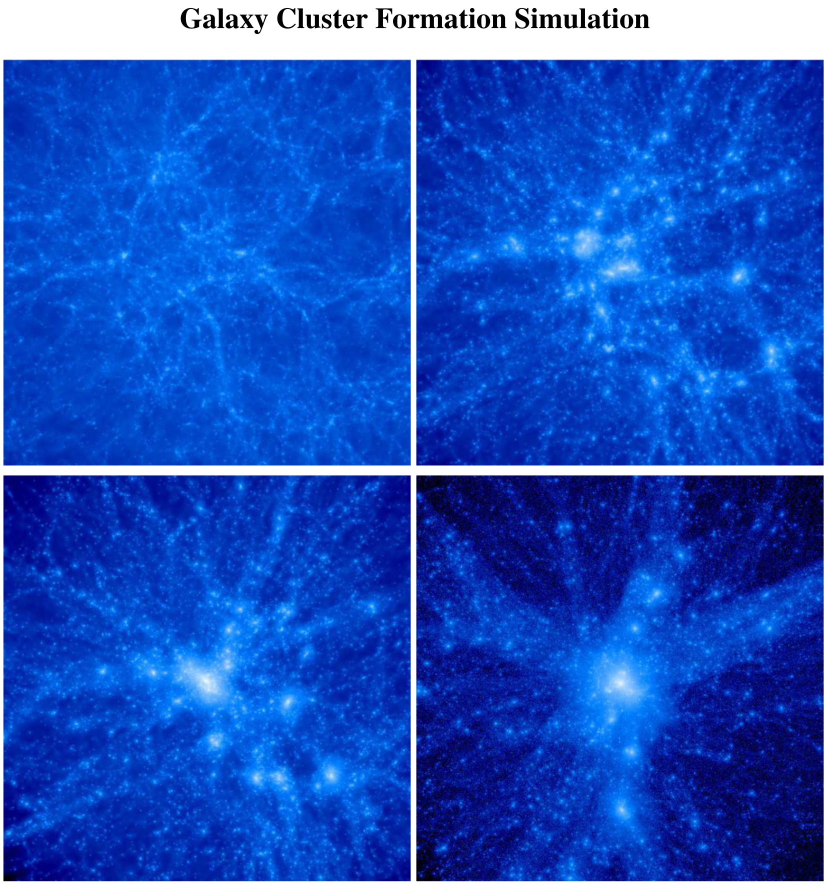

Figure 1.2: Adopted from (Kravtsov & Borgani 2012). Simulation showing the evolution of dark matter density in a comoving region of 15 h^{-1} Mpc. The four panels show different snapshots redshift where top left is $z = 0.3$, top right is $z = 1$, bottom left is $z = 0.5$, and bottom right is $z = 0.0$. It is clear that small density perturbations in the early Universe collapse and grow to large clusters by $z = 0.0$. Also shown is that galaxy clusters form at nodes of the cosmic web, with many filaments leading to a cluster.

centers. Jets of heated gas produced by the AGN propagate through the cluster and heat the ICM through shocks while mixing with the surrounding gas (Yang & Reynolds 2016; Mittal et al. 2009; Vernaleo & Reynolds 2006; Gitti et al. 2012; Sijacki & Springel 2006).

By observing the X-ray emission from the ICM, we can constrain the total cluster mass. To do this, astronomers typically use a model known as the β-model to fit the X-ray emission (Cavaliere & Fusco-Femiano 1976; Jones & Forman 1984; Evrard et al. 1996). The β-model operates under the assumption that the hot gas within the cluster is isothermal and in hydrostatic equilibrium. Hydrostatic equilibrium states that the internal pressure of the hot gas is equal to the gravitational force of the mass of the cluster, thus preventing the cluster from collapsing into itself. If the gas within a cluster is assumed to be isothermal, then it does not change temperature if the volume or pressure changes. Using the β-model, in conjunction with the brightness profile of the X-ray emission, we can calculate the gas density of the X-ray emission source. Under the assumption that the gas is in hydrostatic equilibrium, we can calculate the pressure and thus the gravitational force (Evrard et al. 1996; Piffaretti & Valdarnini 2008; Arnaud 2009; Ettori et al. 2013). While the total mass of a cluster can evolve with redshift, the total mass of galaxy clusters typically ranges from $10^{13}M_{\odot}$ for the smallest clusters to $10^{15}M_{\odot}$ for the most massive local Universe clusters (Schneider 2006; Vikhlinin et al. 2009; Bellstedt et al. 2016; Barnes et al. 2017).

The large amount of mass contained within a galaxy cluster also acts as a telescope. Galaxies positioned behind the cluster can have their light deflected and magnified due to the cluster's mass (Lewis & Challinor 2006; Bartelmann 2010). By measuring the deflection angle, we are able to directly investigate the distribution of dark matter within a galaxy cluster (Bartelmann & Schneider 2001; Schneider 2006; Hoekstra et al. 2013). By understanding the distribution of dark matter, we can estimate the total mass of a cluster. This can be done by simulating what mass an object would need to produce the lensing that we observe.

After the initial cluster structure has formed, it can gain mass through the accretion of gas and other galaxies from the cosmic web or through mergers with other galaxy clusters (Vallés-Pérez et al. 2020). Since clusters form at the intersection of cosmic web filaments, there is a near continuous stream of gas and other galaxies being accreted into the cluster. As the objects infall they can heat and mix the ICM, while also adding mass to the cluster. If two galaxy clusters are sufficiently close they may merge into a single massive cluster. These cluster-cluster mergers are the most energetic events to occur in the Universe since the Big Bang (Sarazin 2002). The shocks from these mergers heat the ICM and the observed X-rays can give an insight into the merger kinematics.

For galaxies that are within or near a cluster, we can measure the clustercentric radius of each galaxy. By measuring the clustercentric radius of cluster galaxies, we can analyze how galaxy properties (e.g. D_n4000, stellar mass, size) change as they approach the cluster center. The clustercentric radius is defined as the projected radius from the cluster center divided by the radius at which the cluster density is 500 (or 200, definitions vary) times greater than the critical density at a given redshift (Kim et al. 2022). As the clustercentric radius decreases, the fraction of quiescent galaxies increases (Balogh et al. 1999; Baldry et al. 2006; Muzzin et al. 2012; Wetzel et al. 2013). The opposite is true for star forming galaxies, as clustercentric radius increases (farther away from the cluster center) the fraction of star forming galaxies also increases (Goto et al. 2004; Kauffmann et al. 2004; Balogh et al. 2004b; Peng et al. 2010; Patel et al. 2012).

1.3 Quenching Mechanisms in Clusters

It has been well established that the environment in which a galaxy resides plays an important role in both its formation and evolution (Vaughan et al. 2020). Galaxy cluster environments have been shown to have very correlated relationships with fundamental properties of galaxies such as morphology (e.g. Postman & Geller 1984; Dressler 1980; Bamford et al. 2009), star formation (e.g. Kauffmann et al. 2004; Gómez et al. 2003; Peng et al. 2010; Noble et al. 2013), and gas content (e.g. Kenney et al. 2004; Chung et al. 2009; Cooper et al. 2010). These observations imply that clusters can affect galaxies through various processes such as ram-pressure stripping, strangulation, tidal interactions, and mergers. In this section, we will examine each of these processes and see how they can influence galaxy evolution.

The ICM has been discussed in Section 1.2.3, and here we examine how the ICM can work as a mechanism to strip gas from infalling cluster galaxies. As a galaxy infalls into the cluster it will experience a ram-pressure from the ICM as it flows past the galaxy (Gunn & Gott 1972). The ram-pressure is defined as

$$P_r \propto \rho_e \nu^2 \ , \tag{1.1}$$

where ρ_e is the density of the ICM and ν is the velocity of the galaxy. This causes a pressure front to build up on the galaxy as it moves through the cluster. The restoring gravitational force of a galaxy on its interstellar medium is

$$F = \Sigma_{gas} \nu_{rot}^2 R_{disk}^{-1} \ , \tag{1.2}$$

where Σ_{gas} is the gas surface density, ν_{rot} is the rotational velocity of a disk, and R_{disk} is the disk radius (Sohn et al. 2019). If the restoring gravitational force of the interstellar medium is greater than the ram-pressure, the ICM will be forced to flow around the galaxy. However, if the restoring gravitational pressure is less than the ram-pressure, then the ICM will flow through the galaxy and remove some, if not all, of the interstellar gas (Abadi et al. 1999). Once a galaxy has had most of its gas content removed it will cease to form stars and begin to appear redder in color.

Another process that cluster galaxies experience is strangulation. Strangulation occurs when the ram-pressure is not great enough to remove the interstellar medium (cold gas) from the infalling galaxy. Instead, during this process, the warm and hot gas in the galactic halo is stripped away (Kawata & Mulchaey 2008). Strangulation of galaxies is very effective, with up to 90% of a galaxy's hot gas within the halo being removed (Kawata & Mulchaey 2008). It is theorized that, in the absence of strangulation, the gaseous halos would eventually cool and turn into molecular gas which would then fuel future star formation (Balogh et al. 2000). This means that once a galaxy has had its gas stripped star formation does not immediately cease. The star formation will continue until all of the remaining cool gas has been consumed (Larson et al. 1980).

Ram-pressure stripping and strangulation are two processes that occur due to the effects of the hot ICM. However, tidal interactions between galaxies also play a role in altering an individual galaxy's star formation. Tidal interactions can occur between two galaxies or between a galaxy and the entire gravitational field of the cluster (Aguilar & White 1985; Byrd & Valtonen 1990). These interactions can affect the spiral structure, the plane of the disk, and the velocity dispersion of matter and gas (Eneev et al. 1973; Gnedin 2003). While there are a variety of tidal interactions, harassment is thought to be one of the most important drivers of galaxy evolution inside galaxy clusters (Bialas et al. 2015). Galaxy harassment can be defined as frequent high speed galaxy encounters (Moore et al. 1996). Harassment of galaxies within the cluster environment can alter the gas content and distribution, the orbital distribution of stars, and the overall shape of the galaxy (Moore et al. 1996).

Galaxies within the cluster environment also experience mergers with other galaxies. Mergers between galaxies can be broken into major and minor mergers. Major mergers are between two galaxies that have similar stellar masses. Exact mass ratios vary across studies, but major mergers between two galaxies typically have a mass ratio around 1:4 or 1:3 (Conselice 2014; Vallés-Pérez et al. 2020). Minor mergers involve two galaxies that have a large difference in their stellar mass. The common mass ratio for minor mergers is 1:10 (Planelles & Quilis 2009; Chen et al. 2019). When an object does not have enough mass to cause a merger event, it is classified as an accretion. These accretion events occur when the two halos have a mass ratio smaller than 1:10 (Planelles & Quilis 2009). The major merger rate for galaxies at redshifts ($z < 1$) is low (Hopkins et al. 2009; Lotz et al. 2011; Bois et al. 2011). As a result, it is likely the that main evolutionary driver for galaxy evolution comes from minor mergers and accretion events (White et al. 2007; Bezanson et al. 2009; Naab et al. 2009; Nipoti et al. 2009; Newman et al. 2012; McLure et al. 2013; van de Sande et al. 2013; van Dokkum et al. 2015; Faisst et al. 2017; Hamadouche et al. 2022; Damjanov et al. 2023).

It is also important to understand at what clustercentric radius these processes are most effective so we can quantify the influence of local density on galaxy evolution. Ram-pressure stripping and strangulation are most effective in the high density regions within the cluster, although it is still unclear whether one mechanism dominates over the other (e.g. Gunn & Gott 1972; Larson et al. 1980; Nulsen 1982; Abadi et al. 1999; Chung et al. 2009; Alberts & Noble 2022). Conversely, tidal interactions and mergers are more effective at large cluster radii where the local density of infalling galaxies dominates (e.g. Eneev et al. 1973; Byrd & Valtonen 1990; Gnedin 2003; Bialas et al. 2015). The above mechanisms do not represent an exhaustive list of quenching processes that can occur in clusters. They are however, theorized to be the leading ways in which galaxy clusters can affect individual galaxies (e.g. Balogh et al. 2000; Boselli & Gavazzi 2006; Haines et al. 2007; Kawata & Mulchaey 2008; Brodwin et al. 2013; Wetzel et al. 2013; Alberts et al. 2014; Kuchner et al. 2017).

1.4 Motivation and Goal of Thesis

We investigate the evolution of structural properties of galaxies within our strongly lensing cluster as a function of cluster radius. Our cluster of interest is located at z = 0.53 and is centered at a right ascension (R.A.) and declination (Dec.) of (R.A., Dec.) = (247.438, 43.823) deg. Our dataset consists of spectroscopic data we obtain from the HectoMAP survey, as well as follow up observations using Keck LRIS. With the follow up LRIS observations, we determine redshifts for all objects and confirm new spectroscopic cluster members. We calculate D_n4000 for both HectoMAP and LRIS spectroscopic cluster members. In addition to our spectroscopic data, we also select photometric cluster member candidates that are near the cluster. Using these photometric cluster member candidates, we calculate a statistical correction for missing spectroscopic cluster members. With this correction, our photometric cluster member candidates and spectroscopic cluster members represent a magnitude limited complete sample of the cluster galaxy population. We use this magnitude limited complete sample to analyze the relation of $D_n4000 - R_{cl}/R_{200}$. In the local Universe, galaxy clusters have been found to have a clear gradient of increasing $D_n4000 - R_{cl}/R_{200}$ (Yoon et al. 2017; Mahajan et al. 2012; Smith et al. 2019). However, at higher redshifts (z > 0.2), the trend of increasing $D_n4000 - R_{cl}/R_{200}$ is not as strong (Muzzin et al. 2012; Kim et al. 2022; Vaughan et al. 2020). We aim to investigate the trend of $D_n4000 - R_{cl}/R_{200}$ for our cluster. We also examine the size-stellar mass relation for galaxies in our cluster and compare to the size-stellar mass relation of galaxies in the field. There are mixed results about whether the size of a galaxy depends on environment or not (e.g. Maltby et al. 2010; Rettura et al. 2010; Raichoor et al. 2012; Papovich et al. 2012; Poggianti et al. 2013). We aim to add clarification to the literature by examining the size-stellar mass relation of galaxies within our cluster. For both $D_n4000 - R_{cl}/R_{200}$ and the size-mass relation, we introduce and discuss potential mechanisms that may cause the relations we observe for galaxies within the cluster environment.

We structure this thesis as follows. We describe the datasets we use in our analysis in Chapter 2. We describe the process of spectroscopic data reduction in Chapter 3. We analyze our spectra to determine redshift, cluster membership, and calculate D_n4000 values for cluster members in Chapter 4. We calculate our statistical correction for missing spectroscopic cluster members in Chapter 5. We present our results and discussion in Chapter 6. Lastly, we summarize the main conclusions of this thesis and discuss potential avenues for future work in Chapter 7.

Chapter 2

Data

Our cluster of interest, identified as HMRM 08268 in Sohn et al. (2021b), is a strongly lensing cluster at a redshift of $z = 0.53$ with a median right ascension (R.A.) and declination (Dec.) of (R.A., Dec.) = (247.438, 43.823) deg. This cluster was originally identified by the HectoMAP survey (Sohn et al. 2021b). Figure 2.1 shows a 9.6 $\times$ 9.6 arcmin *RGB* image of our cluster field. We create this image using the *g, r,* and *i* band images which we obtain from the Hyper Suprime-Cam Subaru Strategic Program (HSC-SSP; Aihara et al. 2018a)[1]. At redshift $z = 0.53$, this image represents an area of approximately 14 proper (physical) Mpc^2 (pMpc^2). We can see that members of our cluster are spatially distributed over a large area on the sky. This cluster is also noted to have 2 brightest cluster galaxies (BCGs), circled in yellow in Figure 2.1, both exhibiting strong lensing arcs. BCGs are defined as being the most luminous and massive galaxies that typically reside within the core of a cluster (De Lucia & Blaizot 2007).

This system was selected for spectroscopic follow up because it is a potential merging cluster with two BCGs that both have strong lensing arcs (Sohn et al. 2021b). The lensed objects are at higher redshifts than the cluster itself. We can use the lens equation to determine the total mass (baryonic matter and dark matter) enclosed within a certain cluster radius. However, in order

---

[1] `https://hsc-release.mtk.nao.ac.jp/doc/`

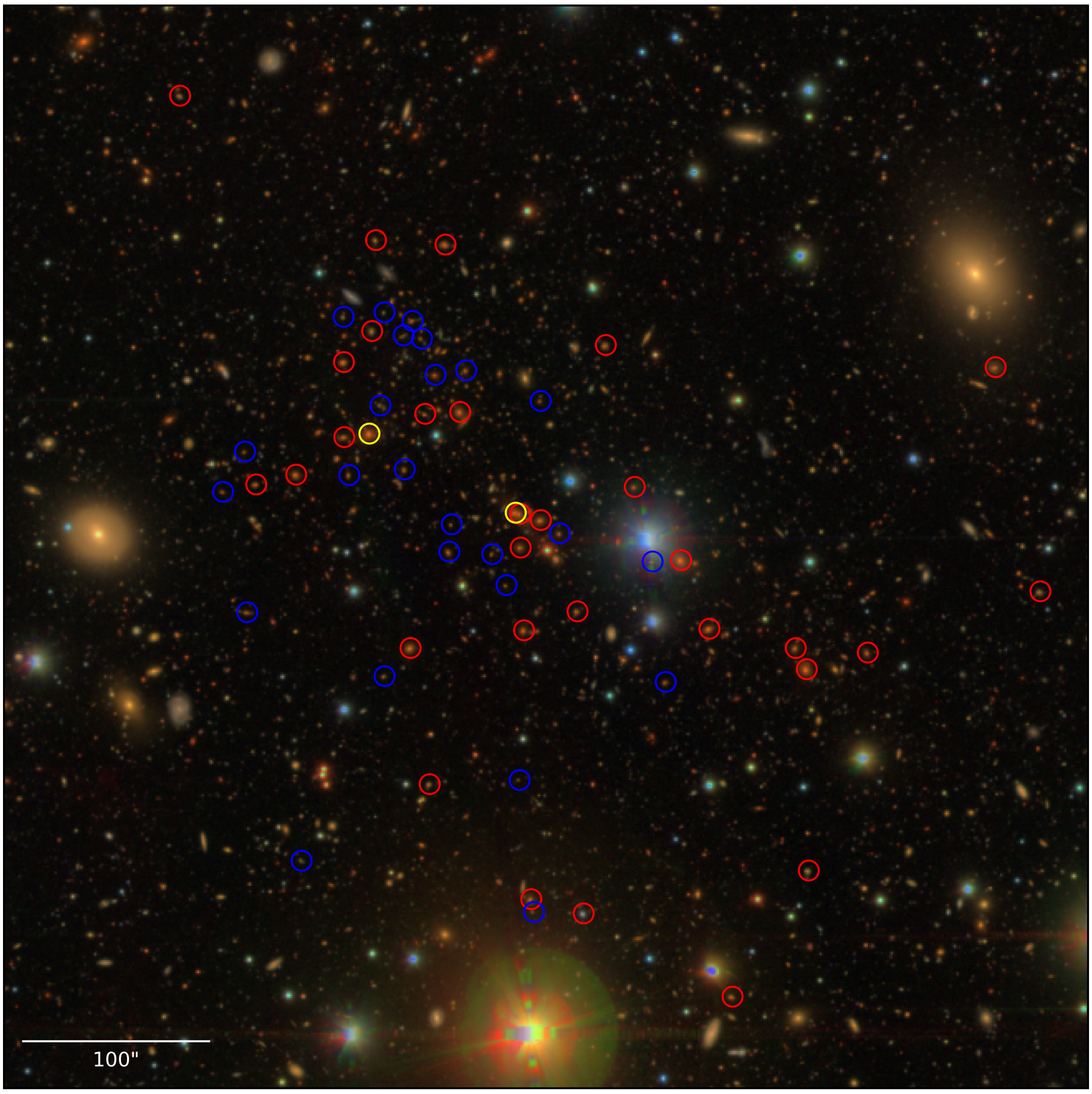

Figure 2.1: *RGB* image of our cluster field created using the *g, r,* and *i* photometric bands of HSC-SSP. Red circles indicate spectroscopic members identified by the HectoMAP survey. Blue circles indicate spectroscopic members confirmed through follow up observations. Yellow circles indicate the two BCGs identified by (Sohn et al. 2021b). The image is 9.6 × 9.6 arcmin. At $z = 0.53$ this corresponds to 3.7 × 3.7 pMpc. The orientation is North up and East left.

to better constrain the lens model, we need to know the redshift of the lensed objects. With the redshifts of the lensed objects, we are able to calculate their luminosity distance from the cluster. With this distance, we will be able to better constrain the lens model, and thus obtain a total mass estimate of the cluster.

Obtaining spectra of the lensed objects is the main goal of the follow up observations. However, the instrument we use is a multi-object spectrograph, allowing us to obtain spectra for galaxies within the cluster as well. This thesis focuses on the spectra we obtain of cluster member galaxies. We currently have 57 spectroscopically confirmed cluster members, out of which 32 were identified by the HectoMAP survey. Through our follow up observations, we identify an additional 25 spectroscopic cluster members.

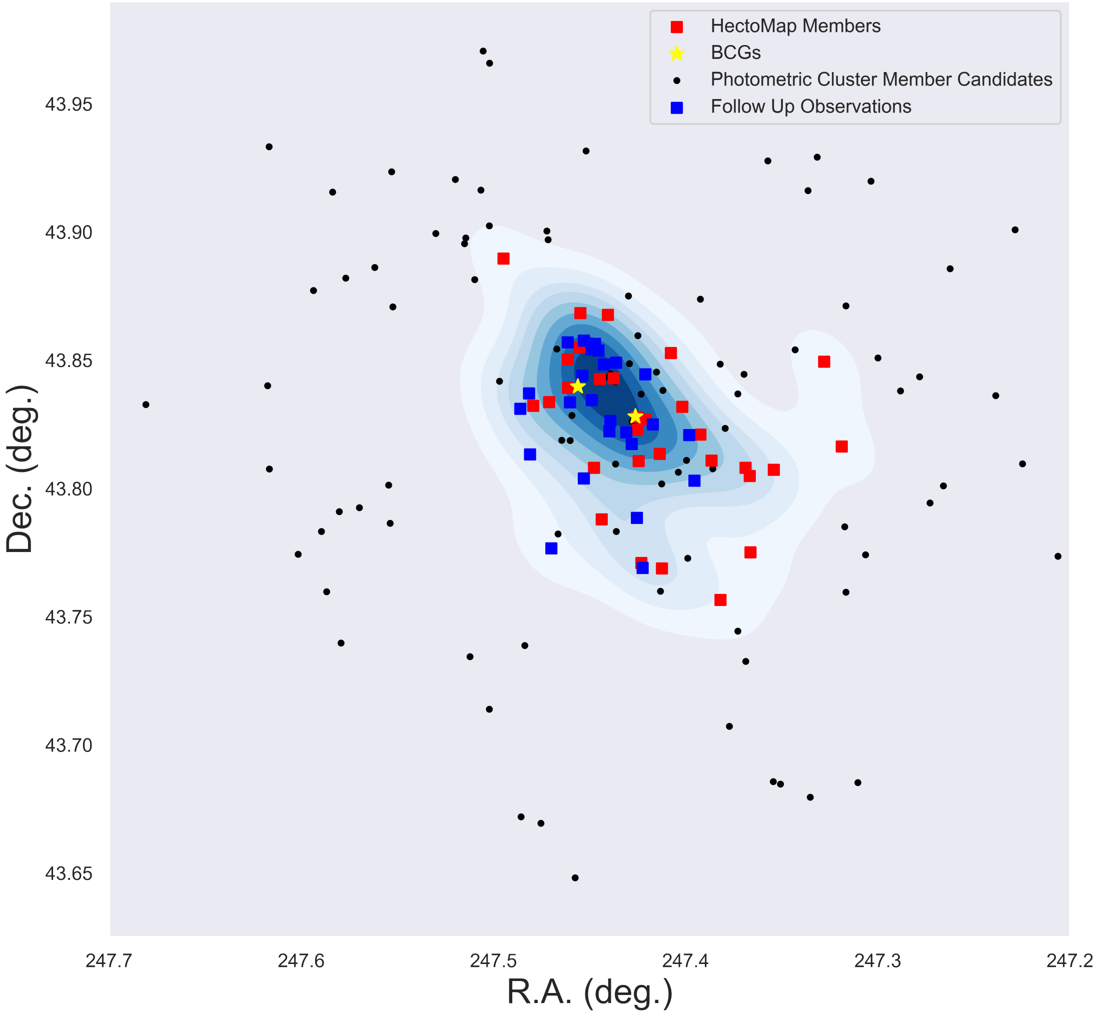

Figure 2.2: R.A. and Dec. density contours showing the non-uniform distribution of cluster members. Red squares indicate spectroscopic cluster members identified by HectoMAP. Blue squares indicate spectroscopic cluster members identified through follow up observations. Black points indicate photometric cluster member candidates. The blue regions show the density of spectroscopic cluster members. We can see that the shape of the density contours are non-uniform throughout the cluster.

In Figure 2.2 we show that the cluster members are not uniformly distributed in the 2D projection of R.A. and Dec. throughout the cluster field. As in Figure 2.1, the red and blue points correspond to HectoMAP members and members we confirm through follow up observations, respectively. The blue region in Figure 2.2 represents the density of all spectroscopic cluster members based on their R.A. and Dec. positions. As a result of having two BCGs and a non-uniform distribution of cluster members, it is highly likely that this cluster is a merging cluster.

We also select an additional 94 photometric cluster member candidates, shown in green in Figure 2.2. These are objects that are in the vicinity of the cluster center and have photometric redshifts close to that of the cluster redshift. We select these additional photometric cluster member candidates to perform a statistical correction for missing spectroscopic cluster members (Chapter 5).

In this chapter, we discuss our spectroscopic dataset (Section 2.1) consisting of both the original HectoMAP spectroscopic observations (Section 2.1.1) and follow up observations using the Low Resolution Imaging Spectrograph (LRIS) at the William Myron Keck Observatory (Section 2.1.2). We then discuss the selection of the photometric cluster member candidates (Section 2.2). Lastly, we describe previously obtained measurements of stellar masses (Section 2.3) and sizes (Section 2.4) for both spectroscopic and photometric cluster member candidates.

2.1 Spectroscopic Data

The HectoMAP survey is a dense, red-selected, redshift survey aimed at furthering our understanding of the evolution of quiescent galaxy populations and their dependence on the environment (Sohn et al. 2021b). The goal of HectoMAP is to obtain a uniformly complete redshift survey of the quiescent galaxy population (Damjanov et al. 2023), clusters of galaxies (Sohn et al. 2018, 2021a), and the cosmic web (Hwang et al. 2016). The full survey covers an area of 54.64 deg^2 within the bounds 200.00 $<$ R.A (deg) $<$ 250.00 and 42.50 $<$ Dec. (deg) $<$ 44.00. HectoMAP is a red-selected survey and is complete for objects with $g - r > 1.0$, and r

$\leq$ 21.3. The survey uses Hectospec (Fabricant et al. 2005), a 300-fiber wide-field instrument on the 6.5-meter Multi Mirror Telescope Observatory (MMTO).

2.1.1 HectoMAP Spectroscopic Data

Hectospec is a moderate-resolution, fiber-fed, optical spectrograph at the MMTO located near the summit of Mt. Hopkins in Arizona. MMTO consists of a single 6.5 meter primary mirror configured in the classic Cassegrain optical design (Fabricant et al. 2005). Hectospec consists of 300 optical fibers that cover a 1 deg^2 field-of-view with a wavelength range of 3700 - 9100 Å. In all, the complete HectoMAP spectroscopic catalog contains $\approx$ 95,000 galaxies.

Since HectoMAP is a red-selected survey, the main focus when collecting spectra is on absorption-line objects. The observed spectra are reduced using Hectospecs standard reduction pipeline, HSRED v2.0. Redshifts are calculated using the cross-correlation package RVSAO (Kurtz & Mink 1998). With the reduced and redshifted spectra, we calculate D_n4000 (Section 4.2) for all spectroscopic cluster member galaxies. We obtain measurements for cluster member galaxies stellar mass (Section 2.3.1), size (Section 2.4), and r band $k-$corrections (Section 5.4).

Figure 2.3 shows four examples of rest frame spectra from the HectoMap survey. In all four panels we can clearly see the CaII H and K absorption lines at 3968.47Å and 3933.66Å, respectively. The spectral resolution of our Hectospec observations is R$\approx$1300, allowing us to distinguish between the majority of spectral features (Fabricant et al. 2005). We smooth the spectra using `Specutils`[2] (Earl et al. 2023) to reduce noise and make spectral features more apparent.

Overdensities are identified in the HectoMAP spectroscopic catalog with the use of the friends-of-friends (FoF) algorithm (Sohn et al. 2021a). The FoF algorithm (Huchra & Geller 1982), starts at a galaxy and then finds other neighboring galaxies within a set distance. This

---

[2] `https://specutils.readthedocs.io/en/stable/index.html`

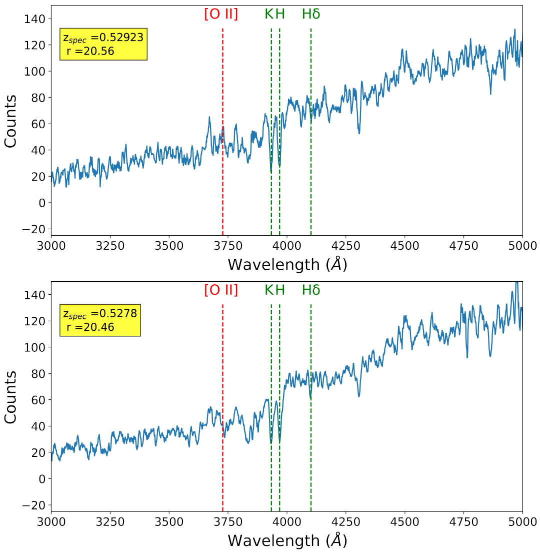

Figure 2.3: Example of rest frame spectra obtained with Hectospec. All four galaxies have clear CaII H and K absorption lines.

is repeated for neighbors of neighbors and results in a set of connected galaxies. Within the HectoMAP spectroscopic dataset, there are 346 galaxy overdensities with 10 or more spectroscopic members identified. Of the 346 galaxy overdensities, one cluster is identified to represent a unique example of a massive system that is in the stage of merging. It is this cluster that is the focus of this thesis work.

2.1.2 Keck Spectroscopic Data

Follow up observations on our cluster of interest use the LRIS spectrograph at the Keck 1 Observatory. LRIS has both a blue and red channel to give us a combined total wavelength coverage of 3,000 - 10,000Å. The spectral resolution of the red and blue channels is R≈940 and R≈560, respectively (Gomez 2022). In Section 2.1.2.1 we discuss the LRIS spectrograph. In Section 2.1.2.2 we discuss the slitmasks we use for our observations. Lastly, in Section 2.1.2.3 we describe details about the observing run.

2.1.2.1 LRIS Spectrograph

Keck 1 is a 10 meter Ritchey-Chrétien telescope (Oke et al. 1995), a variant of the Cassegrain design. LRIS is a visible-wavelength spectrograph that is designed to detect very faint objects up to the limiting magnitude of the telescope (Sprayberry 2002). Figure 2.4 shows the light path of LRIS, as well as the interchangeable dichroic, diffraction grating, and grism. Light entering the spectrograph first passes through its respective slit on the slitmask that sits in front of the field lens. From there the light is collimated and passes through the dichroic beamsplitter. The light split towards the red channel detector is then dispersed and passes through a red filter before finally reaching the detector. The red channel detector consists of a mosaic of two Lawrence Berkeley National Laboratory (LBNL) 2k x 4k fully depleted, high resistivity CCDs (Rockosi et al. 2010). Light split towards the blue channel passes through a grism and a blue filter before reaching the detector. The blue channel detector consists of a mosaic of two 2k x 4k Marconi CCDs (Rockosi et al. 2010). LRIS has a total field of view for both channels of 6×7.8 arcmin and can function using long slit or multi-slit modes. For our observations we use the multi-slit mode.

The diffraction grating that we use for our observations is the 400/8500 grating for the red channel. However, we are unable to use the red channel data in our analysis due to the CCD failing during observations. We account for the failure of the red channel CCD in our selection of the blue channel grism. For the blue channel, we use the 300/5000 grism as it has a high transmission efficiency around the Ca II H and K lines at the cluster redshift of $z = 0.53$. The 300/5000 grism also offers the reddest wavelength coverage available for use with the blue channel of Keck LRIS.

LRIS Spectrograph Layout

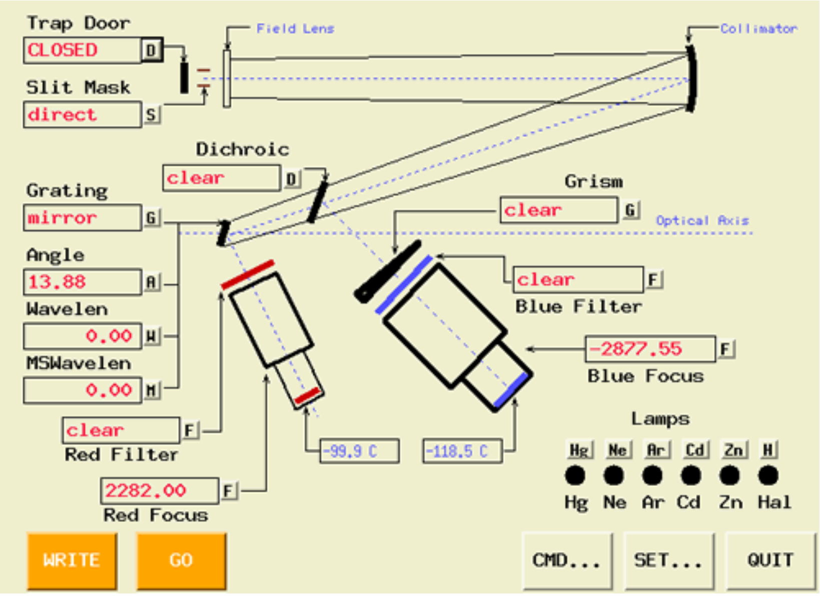

Trap Door CLOSED
Slit Mask direct
Dichroic clear
Grating mirror
Angle 13.88
Wavelen 0.00
MSWavelen 0.00
Red Filter clear
Red Focus 2282.00
Grism clear
Blue Filter clear
Blue Focus -2877.55
-99.9 C
-118.5 C

Figure 2.4: [Adopted from (Gomez 2022)] Light path and the instrument parts of the LRIS Spectrograph used to collect our data. For our observations we use the D680 dichroic at the beamsplitter. For the blue channel we used 300/5000 grism and for the red channel we used 400/8500 diffraction grating.

2.1.2.2 Slitmasks

We use 3 different multi-object slitmasks over the course of our observations. These masks are milled onto sheets of aluminum by the staff at Keck based on the submitted design (Gomez 2022). We design the slitmasks with two main goals in mind. We first want to obtain spectra of arc galaxies lensed by the cluster. These galaxies are our first priority because if we are able to determine the distance from the cluster to the lensed objects we will have better constraints on the distribution of dark matter in the cluster halo. After positioning the lensed arc galaxies on the slitmasks, we then look at our list of potential cluster members. We select potential cluster members by creating a list of objects around the cluster and then sorting by apparent magnitude. We begin by adding slits for those that are the brightest targets in the Field of View. We use these same goals for designing all of our slitmasks shown in Figure 2.5.

Figure 2.5 shows our slitmasks 1, 2, and 3 from left to right, respectively. Each panel in

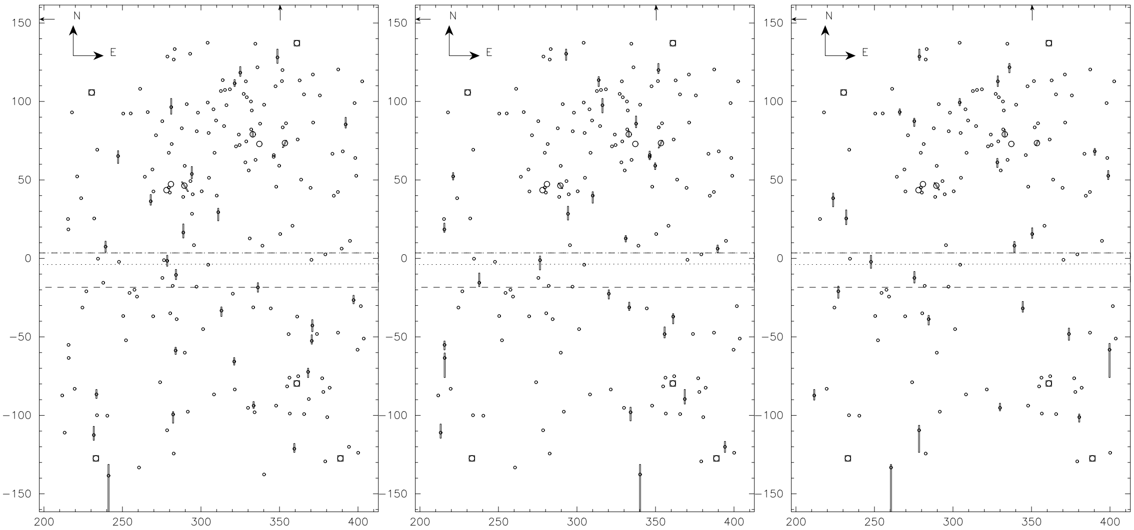

Figure 2.5: Slitmask 1, 2, and 3, respectively, showing the placement of target galaxies onto the CCD.

The small circles with a rectangle overlaid represent the galaxies we have chosen to observe and large circles with a rectangle overlaid represent arc galaxies. Large circles with a square overlaid represent guide stars. The vertical axis is the spatial position of the object and the horizontal axis is the direction along which the spectra will be dispersed. However, the horizontal and vertical axis shown here are the CCD pixel position of each object.

Figure 2.5 shows 203 galaxies that are candidates for observation. Of those 203 galaxies, we are able to put slits on and observe 83. We cannot put slits on all 203 galaxies as the spectra from different objects would overlap. Galaxies that we select to observe are those with a rectangular slit overlaying them. Slitmasks 1 and 2 have 28 targets each and slitmask 3 has 27 targets.

In Figure 2.5, the vertical axis is the spatial position of the object and the horizontal axis is the direction along which the spectra will be dispersed. The length of the slit on each object is maximized to collect as much sky emission spectra as possible without overlapping with other objects. The objects with squares overlaying them represent stars that are used to align the slits on the masks to the correct target galaxies. The vertical axis is centered about the break of the two CCD detectors with two dashed lines on each side representing the area in which data can no longer be obtained. The horizontal axis shows only the pixels from 200 - 400, that represents the offset of the CCD to the optical axis (Gomez 2022).

2.1.2.3 Data collection with LRIS

We collected our data using LRIS at Keck 1 on the night of June 22nd, 2020. Our observations ran for approximately 5 hours and in that time we collected 16 science frames from both the blue and red channel. The science frames had exposure times between 1300 - 1800 seconds, and we collected 6 frames with Mask 1, 6 frames with Mask 2, and 4 frames with Mask 3 (Table 2.1). We also collected numerous calibration frames consisting of arcs and dome flats for each slitmask (discussed in Section 3.1). It was important to collect many calibration frames before, during, and after the observation run because we can then stack the calibration frames during the data reduction. Stacking the calibration frames provides better background subtraction and wavelength mapping than using single exposures. We collected data in the same manner on both the red and blue channels. However, during the observation run the red channel CCD experienced an issue with its amplifier and the chip became unreadable. The blue channel did not experience any interruptions during our observation run. We show a summary of our data collection in Table 2.1.

2.2 Photometric Data

The HectoMAP survey field is also covered by HSC-SSP which has deep 5-band photometry (Section 2.2.1). We use data from HSC-SSP to select a catalog of photometric cluster member candidates. The motivation for doing so is to create a statistical correction for missing spectroscopic cluster member galaxies that are brighter than the magnitude completeness limit ($r \leq 21.3$) of HectoMAP.

HectoMAP is a red-selected survey complete for objects with $g - r > 1.0$ and $r \leq 21.3$. Throughout our photometric sample selection and analysis, we only include objects that have

Table 2.1: This table shows a summary of all data that was collected. For our data reduction we only used the data from the blue channel.

Slitmask	Frame	Exposure (s)	λ Range (Å)	λ_{cen} (Å)	Grism	Grating	$N_{targets}$
Mask 1	Science	3 x 1800	3500 - 7000	5000	300/5000	-	28
Mask 1	Arc	3 x 1	3500 - 7000	5000	300/5000	-	-
Mask 1	Flat	9 x 4	3500 - 7000	5000	300/5000	-	-
Mask 2	Science	3 x 1800	3500 - 7000	5000	300/5000	-	28
Mask 2	Arc	3 x 1	3500 - 7000	5000	300/5000	-	-
Mask 2	Flat	9 x 4	3500 - 7000	5000	300/5000	-	-
Mask 3	Science	2 x 1400	3500 - 7000	5000	300/5000	-	27
Mask 3	Arc	3 x 1	3500 - 7000	5000	300/5000	-	-
Mask 3	Flat	9 x 4	3500 - 7000	5000	300/5000	-	-
Mask 1	Science	3 x 1800	3700 - 9100	6500	-	400/8500	28
Mask 1	Arc	3 x 1	3700 - 9100	6500	-	400/8500	-
Mask 1	Flat	9 x 4	3700 - 9100	6500	-	400/8500	-
Mask 2	Science	3 x 1800	3700 - 9100	6500	-	400/8500	28
Mask 2	Arc	3 x 1	3700 - 9100	6500	-	400/8500	-
Mask 2	Flat	9 x 4	3700 - 9100	6500	-	400/8500	-
Mask 3	Science	2 x 1400	3700 - 9100	6500	-	400/8500	27
Mask 3	Arc	3 x 1	3700 - 9100	6500	-	400/8500	-
Mask 3	Flat	9 x 4	3700 - 9100	6500	-	400/8500	-

$g - r > 1.0$. However, HectoMAP also includes a $r - i > 0.5$ selection to increase completeness for faint ($20.5 < r \leq 21.3$) red galaxies at redshifts > 0.5 (Sohn et al. 2021a). We only use the $r - i > 0.5$ selection to compare our completeness to Sohn et al. (2023) in Section 2.2.1.

2.2.1 Photometric Cluster Member Candidates

We obtain our photometric data from HSC-SSP. HSC-SSP is a wide field multi-band imaging survey that was designed to address a broad field of astrophysical questions. Figure 2.6 shows the wavelength coverage and transmission curves of HSC-SSP. This program utilizes the Hyper Suprime-Cam (HSC) (Miyazaki et al. 2018) that is located at the focus of the Subaru 8.2m telescope in Maunakea, Hawaii. HSC-SSP consists of three survey layers: Wide, Deep, and UltraDeep. For our analysis we use the HSC-SSP Wide layer as it is the only layer that covers our cluster. To select our sample of photometric cluster member candidates we use the most recent release public data release (PDR) 3 (Aihara et al. 2022).

This PDR includes multiple methods of calculating photometric redshifts as well as stellar masses. The methods in PDR 3 are `DEmP`, `Mizuki` , and `DNNZ`. For our analysis we use photometric redshifts and stellar masses derived from the software using the Direct Empirical Photometric method (`DEmP`). We choose to use `DEmP` (Hsieh & Yee 2014) because it excels at estimating stellar mass for a limited number of optical bands. We discuss the `DEmP` method in more detail in Section 2.3.2.

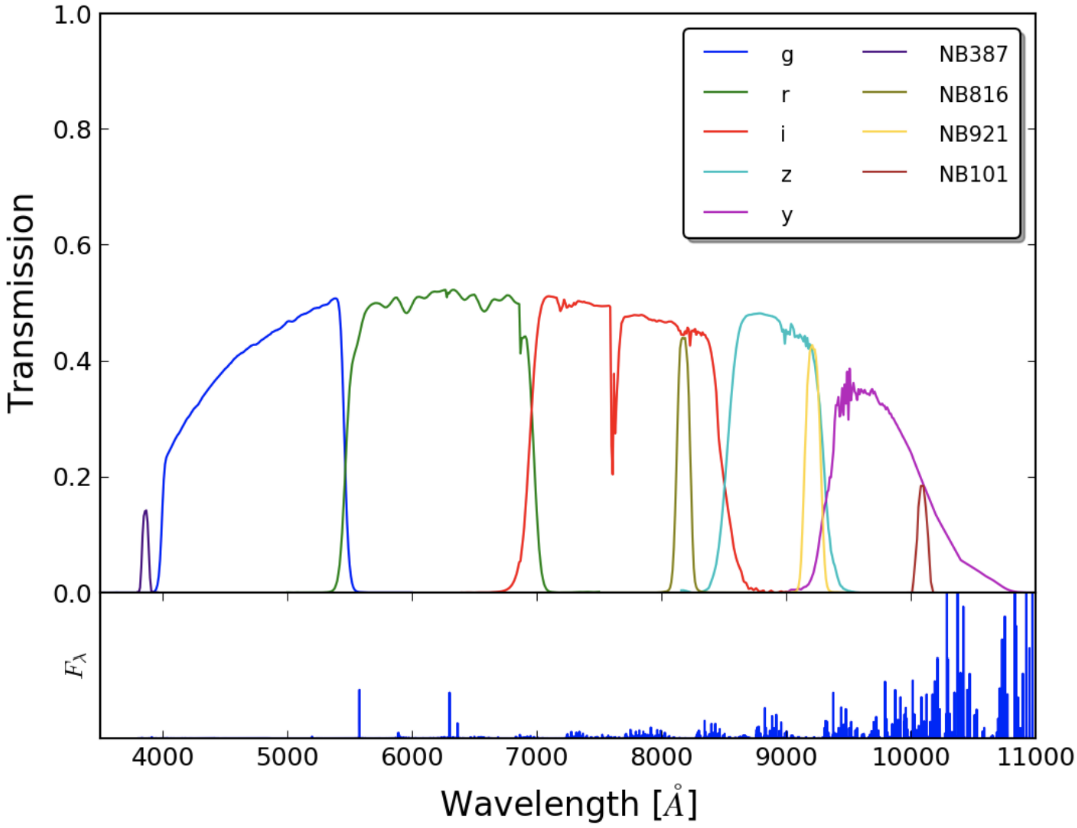

Figure 2.6: Transmission curve of HSC bandpass filters adopted from (Aihara et al. 2018b). Top panel shows the *g r i z y* broad band filters as well as several select narrow band filters sensitive to emission lines, such as Lyman-α, over a wide range of redshifts. The bottom panel shows sky spectrum emission lines. We use the *g, r,* and *i* bands of HSC-SSP for our photometric cluster member candidates.

We use the HSC-SSP photometric data to create a catalog of photometric cluster member candidates. We select the photometric cluster member candidates by doing a conesearch centered about the median R.A. and Dec. (R.A., Dec.) = (247.438, 43.823) deg. of the spectroscopic cluster members. The radius of our cone search is 630" or $7{\times}R_{200}$ (for our cluster R_{200} = 0.56 Mpc $\pm$ 0.03, see Section 1.2.3 for R_{200} discusssion), corresponding to approximately 4 pMpc at $z = 0.53$. We use a large search radius in order to include as many potential cluster members as possible. This radius has physical justification as clusters at this redshift are still assembling and thus cluster members are spread out over a large physical distance. We only select photometric objects that have r band apparent magnitudes brighter than the faintest spectroscopic member in our combined catalog of Hectospec and LRIS members.

To ensure the photometric redshifts of photometric cluster member candidates are not systematically biased, we compare photometric redshifts to the redshifts of spectroscopic cluster members with $g - r > 1.0$, $D_n4000 > 1.5$, and $\log_{10}(M_*/M_\odot < 10.87)$. We find the median offset between photometric redshifts and spectroscopic redshifts to be -0.0064. The median photometric redshift error of these objects is 0.027. The median photometric redshift error is much larger than the median photometric redshift offset. This ensures that photometric cluster member candidates are not being systematically included/excluded from our sample as a result of their photometric redshift.

We also compare stellar masses that we obtain from SDSS photometry to those from HSC photometry for spectroscopic cluster members with $g - r > 1.0$, $D_n4000 > 1.5$, and SDSS $\log_{10}(M_*/M_\odot < 10.87)$. We find the median difference between stellar masses to be 0.00 and the 16 and 84 percentiles to be -0.15 and 0.27, respectively. The median difference between stellar masses from SDSS and HSC is well within the median error (0.233) of our stellar mass measurements. Additionally, there is no systematic offset between stellar masses and no trend in the difference between stellar masses. As a result of this comparison, we are able to use the stellar masses for objects derived using SDSS photometry or HSC photometry together to analyze the size-stellar mass relation of our cluster (Section 6.2).

As a result of our selection criteria, we obtain a large number of photometric objects that are not associated with our cluster. We discuss removal of these objects in Chapter 5. In total, after removal of interlopers, we have 94 photometric cluster member candidates.

After obtaining our catalog of photometric cluster member candidates, we check the completeness of our sample and compare to that of the HectoMAP survey. We do this completeness comparison because HectoMAP target selection is based on Sloan Digital Sky Survey (SDSS) Data Release 16 (DR16) photometry (Ahumada et al. 2020). However, we create our catalog of photometric cluster member candidates using HSC-SSP photometry.

The top left panel of Figure 2.7 shows the 1D distribution of apparent r band magnitudes of our entire spectroscopic catalog (red) against our catalog of photometric cluster member candidates (blue). As expected, the distributions are very similar up until the apparent magnitude completeness limit $r = 21.3$ from HectoMAP (black dashed line). After the mass completeness limit, the number of spectroscopic members decreases while the number of photometric cluster member candidates increases. The other panels of Figure 2.7 show various magnitude cuts to examine how many photometric cluster member candidates are being added to each bin. The r band magnitude cuts follow those presented in (Sohn et al. 2023) and are: $r \leq 20.5$ (top right), $20.5 < r \leq 21.3$ (bottom left), and $r > 21.3$ (bottom right). In all bins we can see that the additional photometric cluster member candidates follow the distribution of the spectroscopic cluster members. This suggests that our photometric cluster member candidates have similar properties to our spectroscopic cluster members.

We now compare the completeness of our sample of spectroscopic members and photometric cluster member candidates to figure 8 of (Sohn et al. 2023). In Figure 2.8, we show the completeness of our sample using the same selections as in figure 8 of (Sohn et al. 2023). Completeness is calculated following the equation

$$C = \frac{N_{spec}}{(N_{spec} + N_{photo})} \, , \tag{2.1}$$

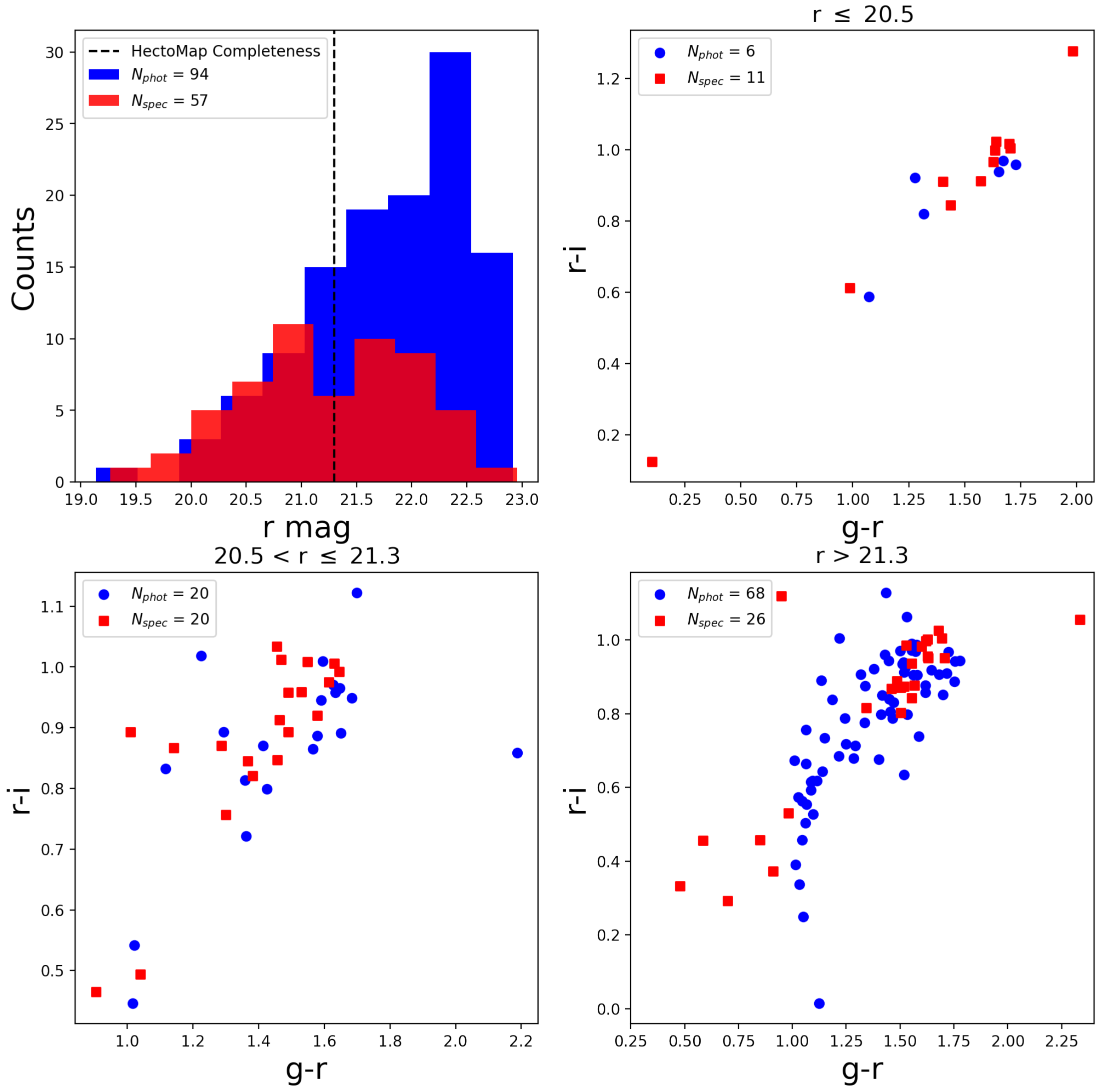

Figure 2.7: Comparison between magnitudes and colors of photometric cluster member candidates and spectroscopic members. Top left panel shows the histogram of r band magnitudes for both spectroscopic (HectoMAP and LRIS) members (red) and photometric cluster member candidates (blue). The black dashed line is the completeness limit of the HectoMAP survey. The other panels show color-color diagrams with various magnitude cuts. The photometric cluster member candidates have similar properties to the spectroscopic cluster members.

where N_{spec} is the number of spectroscopic objects from both HectoMAP and LRIS and N_{photo} is the number of photometric cluster member candidates. We propagate errors on our completeness in quadrature following the equation

$$\Delta C = \sqrt{\left(\frac{N_{photo}}{N_{photo}+N_{spec}}\right)^2 * N_{spec} + \left(\frac{-N_{spec}}{N_{photo}+N_{spec}}\right)^2 * N_{photo}}\,. \tag{2.2}$$

As expected, we find the first and second brightest magnitude bin to be the most complete and are within 2σ of the completeness found by Sohn et al. (2023). Due to the low number of additional photometric objects and their associated photometric errors in these bins, we consider our sample at these magnitudes to be complete and representative of the HectoMAP survey. However, our completeness for the faintest magnitude bin is only $\approx 23\%$. We cannot compare the faintest magnitude bin to HectoMAP as it is below the survey completeness. This low completeness provides the motivation to create a statistical correction to account for the missing cluster members. With our catalog of photometric cluster member candidates, we calculate a statistical correction to account for missing cluster members (Chapter 5).

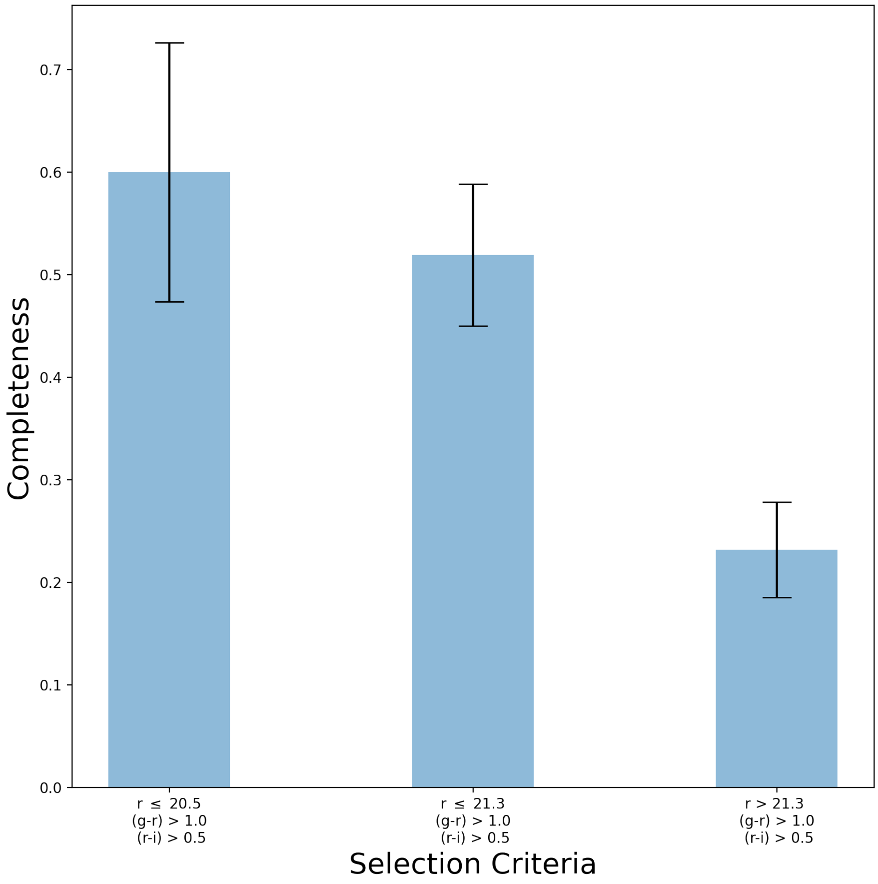

Figure 2.8: Completeness of our sample using the same r band magnitude and color selection as in figure 8 of (Sohn et al. 2023). We find that our completeness is within 2σ of the HectoMAP survey for the two brightest magnitude bins. The faintest bins have no comparable completeness as it is below the HectoMAP survey completeness magnitude. A goal of this thesis is to increase the completeness of the faintest bin using a statistical correction discussed in Chapter 5

2.3 Stellar Mass Measurement

Stellar masses are calculated separately for spectroscopic members and photometric cluster member candidates. This is necessary as we are able to use the spectroscopic redshift to better constrain the stellar mass. In this section we discuss the fitting procedure to obtain stellar masses for spectroscopic cluster members (Section 2.3.1) and photometric cluster member candidates (Section 2.3.2).

2.3.1 Spectroscopic Cluster Members

Stellar masses for spectroscopic cluster members are calculated by Sohn et al. (2021b) using the `LePhare` fitting code (Arnouts et al. 1999; Ilbert et al. 2006). Sohn et al. (2021b) uses the SDSS *u, g, r, i,* and *z* magnitude bands along with the spectroscopic redshift as inputs into `LePhare`. Sohn et al. (2021b) creates a grid of model spectral energy distributions (SED) using stellar population synthesis models (Bruzual & Charlot 2003) with a universal Chabrier (Chabrier 2003) initial mass function (IMF). The grid of models considers two metallicities and exponentially declining star formation rates. Each model SED is normalized to one solar mass. To determine the best fit model SED, `LePhare` performs χ^2 fitting of each model SED to the observed SED, this results in a distribution of best fit parameters. The median of the best fit stellar mass distribution is taken to be the stellar mass of the galaxy.

2.3.2 Photometric Cluster Member Candidates

The photometric redshifts and stellar masses of photometric cluster member candidates are provided by HSC-SSP and are derived using the `DEmP` software (Hsieh & Yee 2014). `DEmP` uses a machine learning approach with training sets to assign both photometric redshifts and stellar masses. The training sets are composed of publicly available deep spectroscopic and multi-band photometric data.

To assign a photometric redshift to a galaxy, `DEmP` selects a subset of the training data consisting of the 50 objects that are closest in a multi-dimensional color-magnitude space to the galaxy. From this subset of training data, `DEmP` uses an empirical quadratic polynomial to calculate the redshift. The empirical quadratic polynomial attempts to find a relation between spectroscopic and photometric properties of the training subset and then apply them to the photometric object (Hsieh et al. 2005). From this relation found using the empirical quadratic polynomial, the galaxy is assigned a photometric redshift. `DEmP` incorporates Monte Carlo simulations and bootstrapping to account for photometric uncertainties in the data and to estimate errors. In the end, each object now has a probability distribution of photometric redshifts. The median of that distribution represents the photometric redshift of the galaxy. The same method to calculate photometric redshifts is used to calculate stellar masses. A more in depth discussion about the `DEmP` method can be found in (Hsieh et al. 2005; Hsieh & Yee 2014).

2.4 Size Measurement

Sizes for both spectroscopic cluster members and photometric cluster member candidates are calculated by Damjanov et al. (2019) using the software Source Extractor (`SExtractor`) (Bertin & Arnouts 1996). `SExtractor` uses 2D modeling based on the HSC-SSP $i-$band images to fit the galaxy surface brightness using the intensity model

$$I(r) = I_0 exp\left(-b_n\left(\frac{r}{r_e}\right)^{1/n}\right) \tag{2.3}$$

introduced by Sersic (1968). The parameters of this model are the central surface brightness (I_0), the half-light radius along the major axis (r_e), and the Sérsic index (n). b_n is a coefficient that ensures that half of the light of the galaxy is enclosed in r_e. From this fit, Damjanov et al. (2019) obtain the parameter r_e for each of our spectroscopic members and photometric cluster member candidates. Damjanov et al. (2019) then calculate the angular diameter distance (Hogg 1999) at the respective redshift for each object. Multiplying the angular diameter distance by r_e results in the major axis radius R_e in kpc. We use R_e throughout our analysis as a measurement of a galaxy's size.

Chapter 3

Keck/LRIS Spectroscopic Data Reduction

In this chapter, we discuss the processing of our raw spectroscopic data. To reduce our spectroscopic data frames we use The Python Spectroscopic Data Reduction Pipeline or `PypeIt`[1]. This pipeline allows us to perform a semi-automated reduction of our LRIS data while also enabling us to use flags to fine tune reduction steps specific to our data set. The final products output by `PypeIt` are the 1D and 2D spectra, which we use to perform spectral analysis (Chapter 4).

To extract scientific data from our images, `PypeIt` performs the following steps:

1. Conversion to Counts
2. Read and Digitizations of Noise
3. Overscan Subtraction
4. Trimming Re-Organization
5. Spatial Flexure Shift
6. Flat-Fielding
7. Counting Statistics and Noise Floor
8. Cosmic Ray Identification and Masking

---

[1] `https://pypeit.readthedocs.io/en/release/index.html`

These steps are run in this order regardless of frame type (e.g. arc, bias, science). The steps listed above are specific to the LRIS spectrograph. At the end of the reduction process, `PypeIt` outputs several files containing calibration checks as well the reduced 2D spectra, from which we extract 1D spectra. By analyzing these calibration files we are able to fine tune the reduction process to our specific data set. Of the processing steps listed above, we can theoretically edit all steps, but this is not always the best practice. We discuss which steps have been edited and why in their respective sections.

In Section 3.1 we discuss the individual processing steps as well as modifications we make to specific steps. In Section 3.2 we examine the output calibration files from `PypeIt` which tell us how well our data are reduced. Lastly, we discuss coadding and extracting the 2D and 1D spectra in Section 3.3.

3.1 LRIS Reduction Pipeline

In this section, we discuss each step that `PypeIt` performs during the LRIS data reduction process as well as the modifications we make to specific steps. The first step that `PypeIt` performs is converting the pixel image units to electron counts. To do this, the reduction algorithm uses the gain of each CCD in units of e^-/ADU, where ADU stands for analog-to-digital units. This conversion allows us to represent the analog voltage generated from incident electrons as a digital number of counts (Howell 2000).

After converting the pixel values to electron counts, the next step `PypeIt` does is to account for the readnoise and digitization of noise. Readnoise or readout noise is a broad term that encompasses all of the noise that is generated when transferring charge from pixels within the CCD to the camera (Richmond 2002). To incorporate this noise, `PypeIt` uses the readnoise variance, which is calculated using the detector readnoise and gain of each amplifier. The readnoise and gain for LRIS are stored within the `PypeIt` subroutine. This accounts for read noise but we still have to address the digitization of noise which arises from converting electron counts into units of ADU. `PypeIt` follows a derivation for the digitization of noise and uses a fixed value of sqrt(1/12) ADU. However, this digitization of noise is negligible compared to the readnoise and is incorporated into the readnoise value.

After converting pixel values to counts and adding the noise values to the detector variance model, `Pypeit` begins to reduce our science frames. The next step in the algorithm is to perform overscan subtraction (Figure 3.1). The overscan frame or region is a section of the CCD that remains covered during the observation run. Since no photons reach this area of the CCD, the overscan region represents the real time noise level or bias of a detector during observations (Chromey 2016). For each science frame, `PypeIt` starts by using the overscan region and subtracting that region's noise level from the science frame. It is important to note that overscan subtraction is done individually for each science frame. This is due to the overscan region representing a "live" bias frame that is only valid for the science frame it was taken with (Littlefair 2020). Errors in the overscan subtraction are propagated through the reduction and added to the overall error budget (Prochaska et al. 2020).

After subtracting the overscan region from each science frame, `PypeIt` then trims the frames to include only the regions that include data. The convention within the algorithm is to orient the frames in such a way that bluer wavelengths are at smaller pixel coordinates and redder wavelengths are at larger pixel coordinates along the vertical axis.

In the next step `PypeIt` corrects for spatial shifts in the slit positions. This is due to flexure from within the instrument itself. LRIS is known to have significant flexure and this must be corrected during the reduction process (Perley 2019). This shift is corrected by calculating the spatial offset of each science frame compared to the flat field frames. This correction is then applied before extracting spectra (Prochaska et al. 2020).

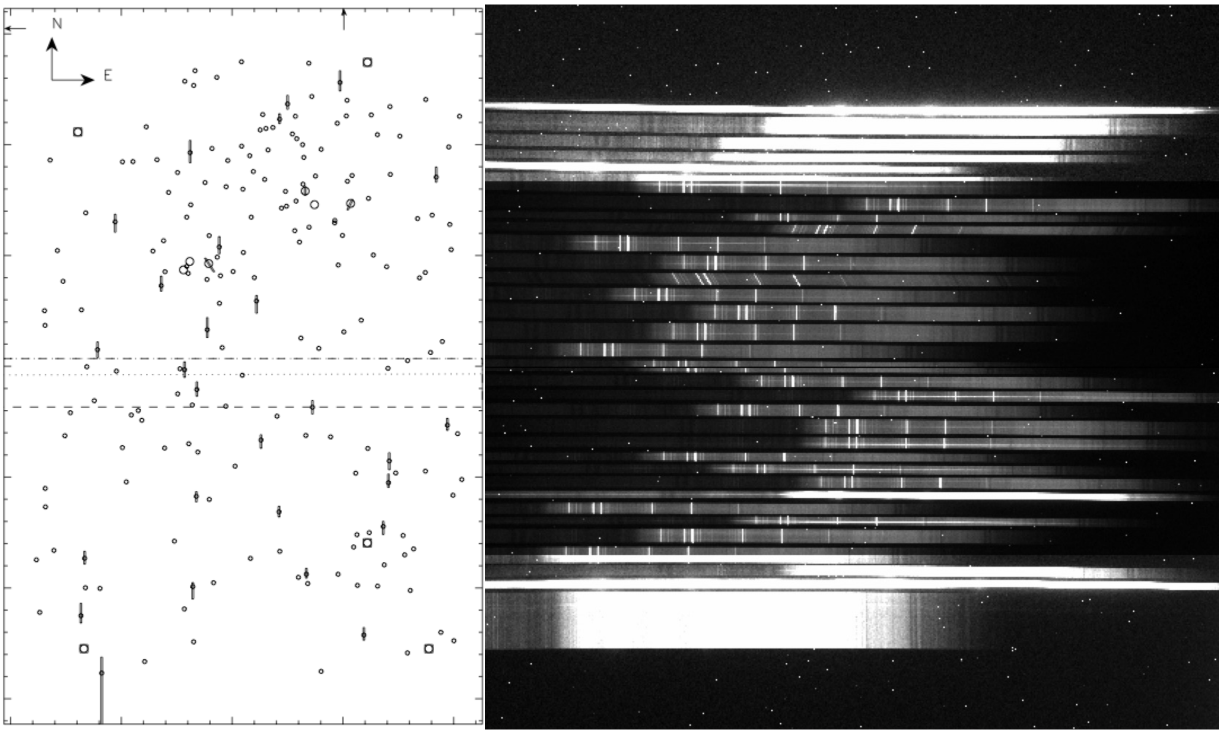

Figure 3.1: Mask 1 from Figure 2.5 shown with the corresponding science frame. On the science frame, we can see the overscan region on the top and bottom. The vertical axis is the spatial direction and the horizontal axis is the spectral direction. This frame contains 28 potential cluster members. Slits that are completely saturated in the spectral direction are guide stars used to align the slitmask when observing. Some slits are tilted as a result of being placed on lensed galaxies.

`Pypeit` then proceeds to use the flat field frames. Flat field frames are arguably the most important, yet difficult to obtain, calibration frames. As the name suggests the frames are of a "flat" or uniformly illuminated target and are taken with the same optical elements we use during the observation run. These frames are taken to correct pixel-to-pixel variations in the detector as well as dust or scratches on any of the optics of the instrument (Chromey 2016). To correct for these variations we take several flat field frames with exposures of 4 seconds.

The difficulty in obtaining accurate flat frames comes from being able to produce a uniformly illuminated target. Illuminating a uniform target can be difficult but is essential to obtaining useful flats. There are traditionally three potential targets that can be used to obtain flat frames: bright twilight sky, dark night sky, or a nearby object. For our observations, we use the inside of the telescope dome as our nearby object. Using the inside of the telescope dome allows us to control the intensity of illumination. The slits are illuminated in such a way in an attempt to match the illumination pattern of our target objects

The individual flat frames are overscan subtracted and averaged together to create a Master Flat. The Master Flat is then divided, or normalized, by the mean flux of the illuminating object. The science frames are then divided by the normalized Master Flat to obtain the flux corrected for the pixel-to-pixel variations of the detector (Littlefair 2020). For our spectrograph, `Pypeit` only applies the flat fielding correction to science and standard frames (standard frames are those that contain stars with well-known flux or standard stars). Errors in the flat field correction are propagated through the reduction and added to the overall error budget (Prochaska et al. 2020).

We also modify several of the flat field parameters within `Pypeit`. These parameters are executed during the flat fielding step because `Pypeit` uses these frames to trace the slits (Prochaska et al. 2020). First, we modify the `edge_thresh` parameter, shown in Figure 3.2. This lowers the threshold for the amount of light necessary for `Pypeit` to identify a slit (Prochaska et al. 2020). We find that in the reduction runs, some slits would be missed because their positioning on the CCD resulted in a lower number of counts than neighboring slits. This resulted in `PypeIt` skipping over the slit because it did not detect a slit there. By adjusting this threshold, `PypeIt` is able to identify the majority of slits.

However, this change did not work for all slits, especially those that were short (see Figure 2.5) and contained faint objects. Some slits were significantly shorter than others. This is done so that spectra from multiple objects do not overlap. For these slits, we adjusted the `minimum_slit_length` and `minimum_slit_length_sci` that `Pypeit` used for identifying slits. This changes the minimum length that `Pypeit` will detect and recognize as a slit in flat and science frames (Prochaska et al. 2020). For LRIS, the default values are 4.0 arcsec and 6.0 arcsec, respectively. We can see in Figure 3.2 that we had to use significantly smaller values. These values represent the length of the slit and short slits can be misinterpreted as alignment slits which do not have spectra extracted. However, for the shortest slits, we had to manually input where they were located using the `add_slits` parameter. This parameter allows us to enter the detector, spectral position, and left and right spatial position of slits. We use this parameter block to manually identify slits that `PypeIt` does not detect.

Lastly, we adjust the `sig_thresh` parameter which controls the threshold of flux used to identify objects within the slits (Prochaska et al. 2020). We have several slits that contain faint objects that are not detected with the LRIS default value for `sig_thresh`. By lowering this value from the default of 10 to 3 (Figure 3.2), `PypeIt` is able to detect and identify fainter objects.

One of the last steps `Pypeit` performs is counting statistics and noise floor. This is done after reducing all of the science frames. At this point, `Pypeit` calculates the shotnoise and the noise floor of the science frames. Shotnoise is related to the uncertainty of measurements when using a CCD and estimates the noise due to photon statistics (Richmond 2002). The shotnoise error is calculated by taking the square root of the number of detected electrons. This is done

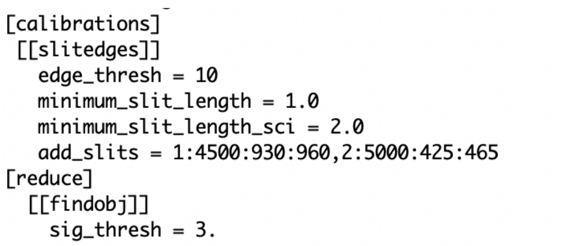

```
[calibrations]
 [[slitedges]]
   edge_thresh = 10
   minimum_slit_length = 1.0
   minimum_slit_length_sci = 2.0
   add_slits = 1:4500:930:960,2:5000:425:465
[reduce]
  [[findobj]]
    sig_thresh = 3.
```

Figure 3.2: `Pypeit` uses the flat field frames to trace and identify slits. This figure shows the parameters used to identify short and faint slits. `edge_thresh` changes the threshold amount of light needed to identify a slit. `minimum_slit_length` and `minimum_slit_length_sci` change the minimum length a slit can be to be detected by `Pypeit`. `add_slits` allows us to manually enter in a slits detector, spectral position, and spectral position bounds. `sig_thresh` changes the signal threshold needed to detect an object within a slit.

for all frames and is included in the final error of the image reduction. After this, `Pypeit` then applies a noise floor to all science and standard frames. The noise floor is essentially the lowest possible amount of noise a CCD can achieve. `Pypeit` adds a fractional value via the noise floor to the overall reduction error budget. The noise floor is calculated as

$$\epsilon \times c^2 \tag{3.1}$$

where c is the number of flat field corrected counts and ϵ is the `PypeIt` parameter `noise_floor`. For LRIS, the default `noise_floor` is set to 0.01, meaning the maximum signal-to-noise in a science image is 100.

The last step in the reduction process is cosmic ray identification and masking. This step removes cosmic ray strikes on the detector by following the L.A. Cosmic Ray Rejection algorithm [2]. This algorithm works by analyzing the edges of potential cosmic rays using a variation of Laplacian edge detection(van Dokkum 2001). `PypeIt` then masks the detected cosmic rays and filters out falsely identified cosmic rays. Cosmic ray strikes can bee seen in Figure 3.1 as single, bright, white pixels scattered randomly across the image.

---

[2] `http://www.astro.yale.edu/dokkum/lacosmic/`

3.2 Reduction Calibration Files

After a successful reduction run, `PypeIt` outputs numerous calibration files for each science frame that allow the user to check the accuracy of the data reduction. There are four different calibration files created for each slit within the science frames.

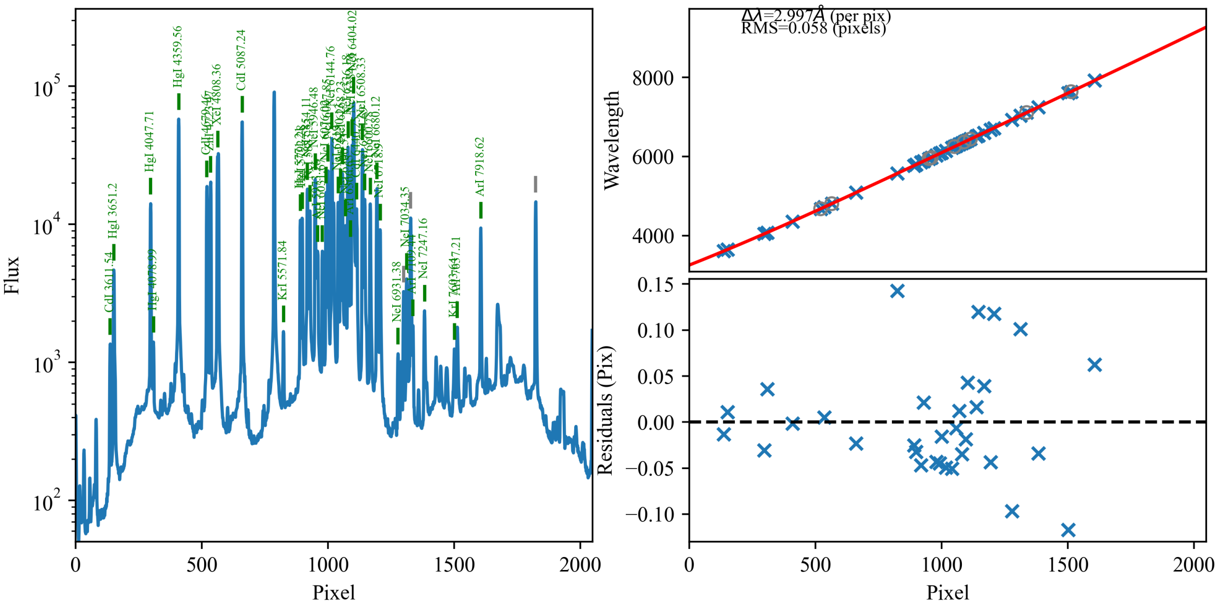

Figure 3.3: Left: An example of the spectrum produced by observed arc lamps (flux vs. the pixel number in the spectral direction). The green labels correspond to identified emission lines and their wavelengths. These identified emission lines are used in the two panels on the right to show 1) the best solution for the mapping between wavelength and spectral pixels (blue crosses and red line in the top panel), and 2) the distribution of residuals from the fit (bottom panel). This diagnostic diagram is produced for each slit on a given mask.

The first file to discuss is the wavelength calibration fit file. This file quantifies how well the emission lines observed from the arc frames match to the known emission lines from the elements within the arc lamp for each slit. Arc frames are the calibration frames that enable us to map wavelengths to pixel positions on the CCD. These frames are taken using the same optical setup that we use to collect the science frames. The target for arc frames is an arc lamp inside the dome of the telescope. The arc lamp contains a known assortment of elements and produces emission lines when observed. Once the arc frames are taken, the spectra are extracted using the same methods as we would for the science frames (Section 3.3).

The wavelength calibration is calculated by pattern matching the lines detected from the arc frames with the lines expected from the arc lamp (Prochaska et al. 2020). Figure 3.3 shows an example of the wavelength calibration. The left panel of Figure 3.3 shows the observed arc emission lines. The observed emission lines are in blue and identified lines have a green label. The horizontal axis shows the pixels along the spectral direction and the vertical axis shows the recorded flux in units of counts. Ideally, this panel would show the majority of the emission lines being identified. The top right panel of Figure 3.3 shows the best fit line between the wavelengths of identified lines and the pixel position along the spectral axis of those lines. A good fit will have a Root Mean Square (RMS)[3] less than 0.1 pixels. The bottom right panel of Figure 3.3 shows the residuals from the best fit line in the above panel as a function of pixel position along the spectral position. The residuals are calculated as the difference between actual wavelength values and pixel positions. This fit is accurate if we see most points scattered about similar values to the above RMS. If there is random scatter around the zero point there is very little difference between the model and the observed spectra. We visually inspect the wavelength calibration for all slits in all slitmasks. We find a median RMS of 0.302 pixels for all slitmasks. We find that `PypeIt` is able to accurately map wavelengths to pixel values for all frames.

The next file that `PypeIt` outputs is the 2D Arc Tilts file. This file contains both the spectral and spatial positions of all spectral lines (Figure 3.4). The horizontal axis is centered about the central trace point of the line and the vertical axis is the spectral pixel position of the line. This file is generated for each slit that is on the mask and shows how well different wavelengths are traced across the slit. The solid black points represent the 2D model that spatially maps identified arc emission lines across the detector. The hollow black circles correspond to points that match the tilt as described by the 2D model. The hollow red circles are those points that

---

[3] RMS is the square root of the mean of n squared values. It is typically used to measure imperfection of model fit to data and is given by the formula RMS = $\sqrt{\frac{1}{n}\sum_{i=1}^{\infty} x_i^s}$ (Jones 2018)

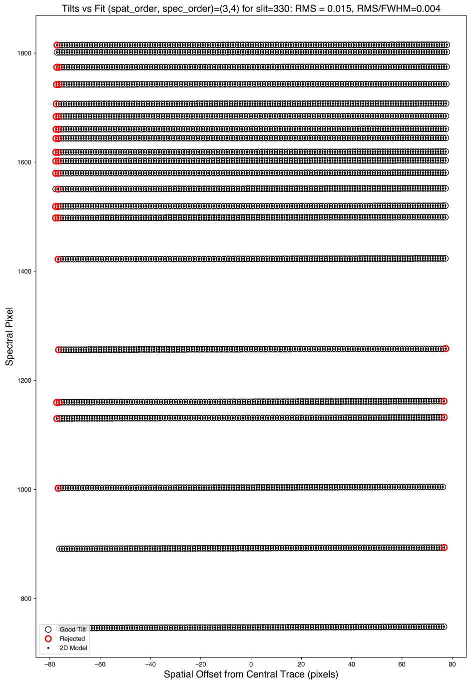

Figure 3.4: An example of wavelength tracing across each slit. The vertical xis is the spectral direction and the horizontal axis is centered about the spatial direction of the slit. The solid black points correspond to the 2D model mapping emission lines across the slit. The hollow black circles are points that match this model while the hollow red circles are points that disagree with this model. An ideal fit would have black points across the full detector length with the red points only appearing on the edges.

do not match the tilt as described by the 2D model and have been rejected. These points are primarily on the edges of the slit where it may be difficult to obtain an accurate wavelength to trace. It is acceptable to have these red points as long as they are mostly confined to the edges of the slit and not in the middle of the slit. We visually inspect the spectral and spatial positions of spectral lines for all slits in all slitmasks. We find that all slits have accurate wavelength tracing.

Once wavelengths have been traced across the detector, `Pypeit` then checks the spatial tilt of the slit. This shows whether or not there is significant spatial flexure that may effect the extracted spectra. This is shown in Figure 3.5, where the vertical axis is the tilt residuals (calculated from Figure 3.4) and the horizontal axis is the spatial offset from the slit center.

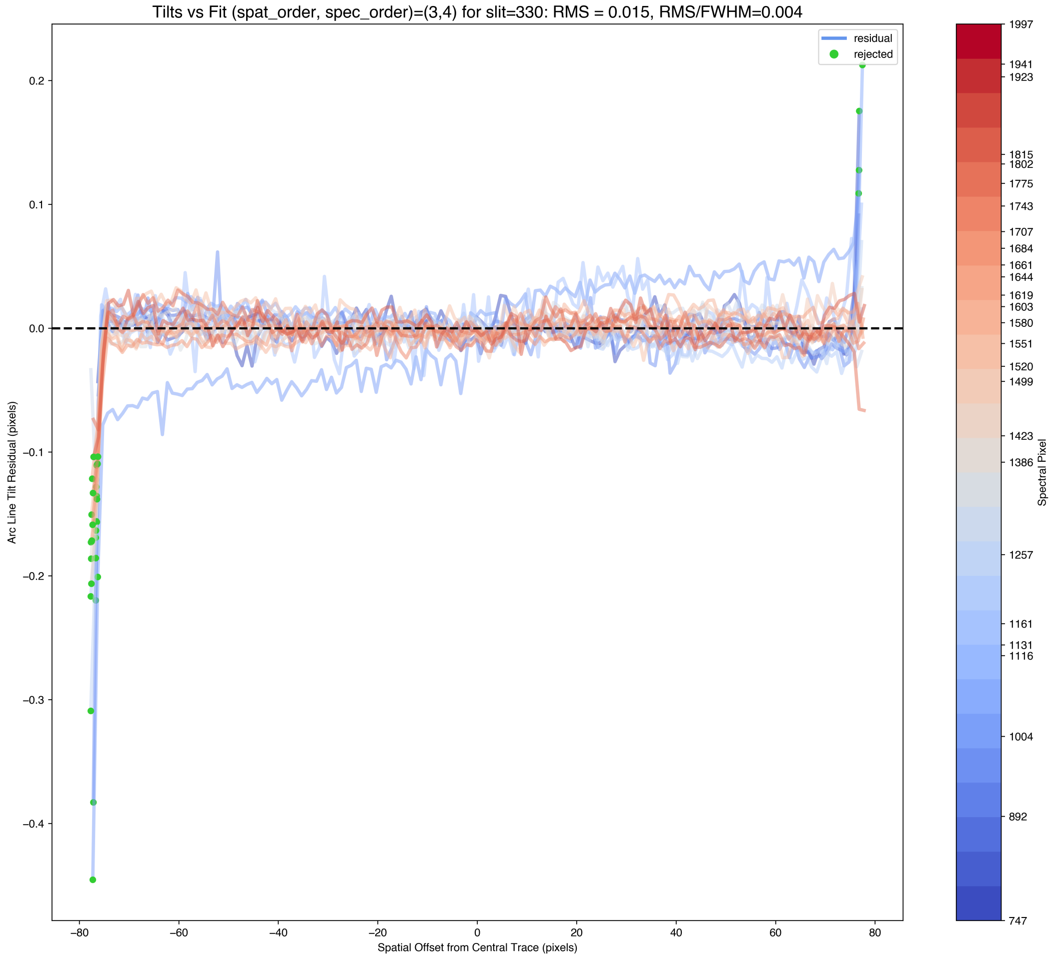

Figure 3.5: Residuals from the model and observed tilt in Figure 3.4 vs. the spatial position of the slit. Each line is colored by the spectral pixel position, which acts as the wavelength of each line. Inspecting this plot allows us to check for spatial flexure across slits. The green points are those that have been rejected for having significant residuals. Ideally, this plot shows small residuals centered about the zero point with no spectral bias. However, it is common to have significant residuals at the edges of each slit.

Residuals are calculated by taking the difference between the tilt of the slit and the 2D tilt model. The lines are colored by their spectral pixel positions, smaller pixel values indicate bluer wavelengths and larger pixel values indicate redder wavelengths. Residuals that have been rejected by `Pypeit` are shown as green circles. An acceptable fit will show most residual points plotted around the zero points, with no bias towards the wavelength of the line. However, it is important to note that it is common for there to be significant residuals on the spatial edges of the slits. We visually inspect the spatial flexure for all slits in all slitmasks. We find that `PypeIt` is able to accurately account for and correct the spatial flexure of LRIS for all slits.

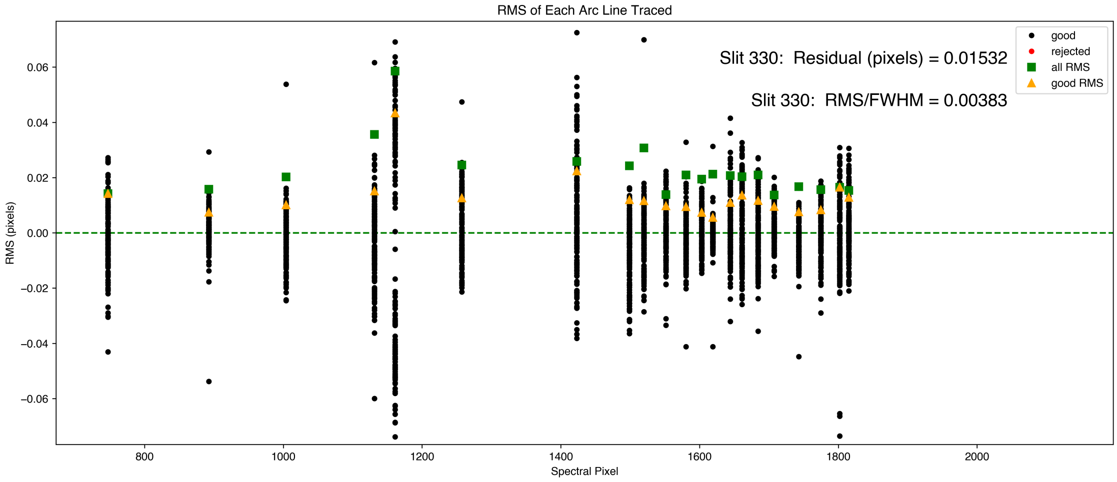

Figure 3.6: The spectral flexure of individual slits. The vertical axis is the residuals from Figure 3.4 and the horizontal axis is the spectral pixel position. The black points correspond to accepted residuals and the red points are rejected residuals. The green squares are the RMS of all residuals at that wavelength and the orange triangles are the RMS of all accepted residuals at that wavelength.

In addition to spatial tilts, `Pypeit` also analyzes the spectral tilts. Figure 3.6 has the same vertical axis as Figure 3.5 however the horizontal axis is the spectral position instead of the spatial position. When inspecting this plot we aim to see the black points, representing the accepted residuals from Figure 3.6, scattered about the zero point. We also want to ensure that the orange triangles, showing only the accepted residuals RMS, and the green squares, showing all residuals RMS, are close to the zero point. The red points are residual values that have been rejected. We visually inspect the spectral flexure for all slits in all slitmasks. We find that `PypeIt` is able to accurately account for and correct the spatial flexure of LRIS for all slits.

It is important to note that the `PypeIt` parameter (Section 3.1) changes we present here are the result of numerous data reduction runs. After each reduction run we inspect the output spectra and calibration files to ensure the accuracy of our data. The calibration figures shown above are examples from our data reduction. We show them as representative calibration files for all slits we have reduced. Naturally, there will be variation in the calibration files from slit to slit and even between the same slit over multiple reduction runs. Regardless, we ensure that each slitmask has been reduced to its most accurate form and that the spectra we extract (Section 3.3) are a true representation of the observed object.

3.3 1D and 2D Spectrum

The final set of files that `Pypeit` outputs are the 2D and 1D spectra. These are written as FITS files and contain spectra that are extracted from the science frames. The 2D spectra frames are reduced following the steps we describe in Section 3.1 and we ensure the optimal performance of the pipeline in each step in Section 3.2.

We show an example of the reduced 2D spectra frames in Figure 3.7. This frame corresponds to one detector with our slitmask 1. The slits that `PypeIt` is able to identify are shown with green and pink on the left and right sides, respectively. Objects identified within the slits are traced with an orange line and labeled with their spatial information. With the modifications made to the reduction pipeline (Section 3.1), `PypeIt` is able to identify all slits on every slitmask. However, as we can see in Figure 3.7, not every slit has an identified object. For intrinsically faint objects, a single exposure does not contain enough signal for `Pypeit` to identify the object.

To obtain the 1D spectra from our reduced science frames, `PypeIt` performs two final steps: sky subtraction and 1D spectra extraction. As a result of using a ground-based spectrograph, we not only collect the spectra of our target objects but we also collect spectra of the Earth's atmosphere. In order for our science frames to be useful we must remove the background sky spectra, this process is known as sky subtraction. For sky subtraction, `PypeIt` follows the standard Horne algorithm (Horne 1986). At each wavelength, the sky emission is interpolated on each side of the target object spectrum. The sky emission is then fit using a weighted least-squares polynomial, where the weights are inversely proportional to the pixel variance. A mask

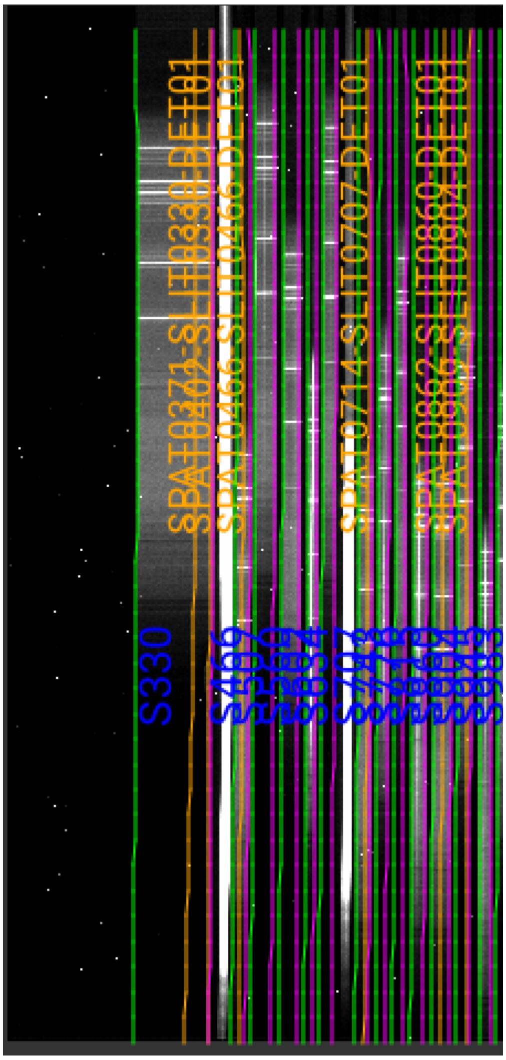

Figure 3.7: An example of 2D spectra extracted using `Pypeit`. Shown is one detector with slitmask 1. The slits identified by `Pypeit` have green and pink boundaries on the left and right of each slit, respectively. The slit names in blue are obtained from the center spatial pixel of each slit. Objects identified within the slits are shown with an orange line and label containing information on the spatial position. Inspecting the 2D spectra is essential to ensure all slits have been identified.

is then created to model the sky emission over the area of the slit that contains the target object spectra. This process is done for each slit as the sky spectra are unique for each slit. The result of this process is a frame that contains only the sky spectra for each slit.

Once the sky spectra are modeled for each slit, `PypeIt` then subtracts the sky subtraction frame from the reduced science image. This results in a science frame that contains only the 2D target object spectrum. However, we are interested in obtaining the 1D spectrum of our objects.

To extract the 1D spectrum, `PypeIt` defines the "object limits" or aperture for extraction. The aperture is the spatial width needed to enclose the object spectrum. `PypeIt` assumes a spatial Gaussian profile and sets the aperture at 3 times the full-width half maximum (FWHM) that is computed from the object's flux profile (Horne 1986). The result of this procedure is the 1D spectra of our target objects which we can then use to calculate redshifts (Section 4.1) and $D_n 4000$ values (Section 4.2).

To obtain spectra for all objects in each of our slitmasks, we perform an extra step in our reduction process known as coadding. Coadding is the process of combining multiple exposures of the same object into a single frame. By coadding the 2D science frames together, we are able to increase the signal-to-noise for all objects. This allows us to extract spectra for faint objects that `PypeIt` was unable to detect in a single exposure. Coadding multiple frames also helps correct for over/under subtraction sky lines in individual exposures. For slitmasks 1 and 2, we have 3 science frames, therefore the coadded science frames for these slitmasks are a composite consisting of 3 frames. For slitmask 3, we only have 2 science frames, and thus the coadded science frame is a composite consisting of 2 frames. Coadding different numbers of frames for each mask does not affect our results as caodding only increases the signal to noise, the intrinsic properties of the spectra are not altered. `PypeIt` contains an automated routine that coadds frames from the same slitmask together. After coadding the frames from each slitmask together, `PypeIt` then extracts the 1D spectrum for each object.

Figure 3.8 shows an example of a 1D spectrum from a single exposure (left panel) compared to the 1D spectrum from the coadded exposures (right panel). We smooth and plot the spectrum using the python package `Specutils`. Additionally, we utilize the bad pixel mask output by `PypeIt`. This mask covers pixels that have been flagged throughout the reduction process. The single exposure clearly has residual sky lines at ≈ 5600Å and 6300Å , whereas the coadded spectrum does not have as strong residual sky lines. It is important to note that since the coadded

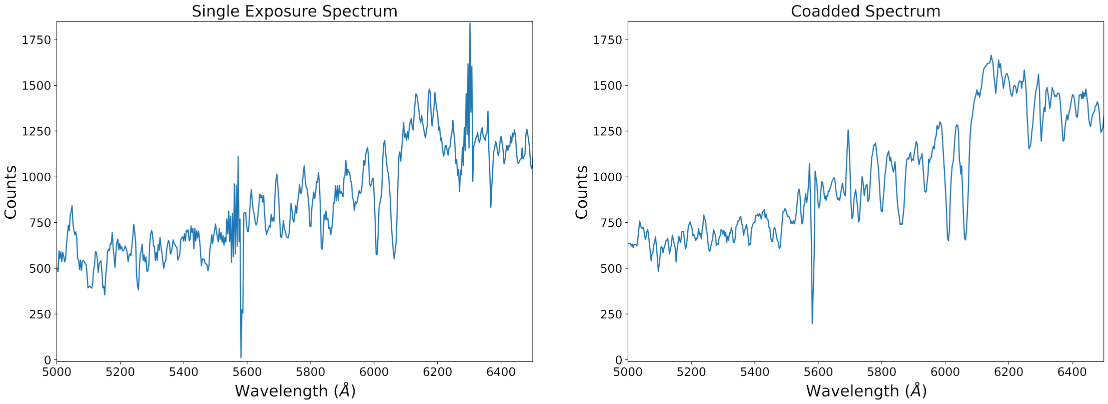

Figure 3.8: Left panel shows 1D spectrum extracted from a single 2D science frame. The average signal-to-noise of this single exposure is 4.2. Right panel shows 1D spectrum of the same object extracted from a coadded 2D science frame. The signal-to-noise of the coadded frames is 9.3.

spectrum is a result of combining single exposures, if all exposures for an object have bad sky subtraction then the coadded spectrum will also have bad sky subtraction. After coadding all science frames together, we find an average increase in signal-to-noise of 1.9. Throughout the remainder of our analysis we use 1D spectra extracted from the 2D coadded science frames.

We show a summary of our reduced spectrum in Figure 3.9 for a fiducial LRIS cluster member. The top panel is the 1D coadded spectrum. The second panel (1) shows the 2D coadded object model spectrum, which is collapsed along the spatial direction to get the 1D coadded spectrum. The following three pairs of panels show the 2D galaxy spectrum (A) and sky subtraction (B) frames from the individual exposures. Frames with the same number (i.e. frame 2A and 2B) are from the same exposure. We can see that prominent sky lines (such as the OI line at 5577.35Å) are sometimes over or under subtracted during the reduction process and that this over/under subtraction is not uniform across all science frames. By analyzing the spectra of our objects in this manner, we can better understand which spectral features are true to the object and which features are remnants of poor sky subtraction. Knowing which spectral features are residuals from sky subtraction and which are intrinsic to the object is important for redshift determination (Section 4.1). We present all LRIS cluster members spectra in the same format as Figure 3.9 in the Appendix A.1.

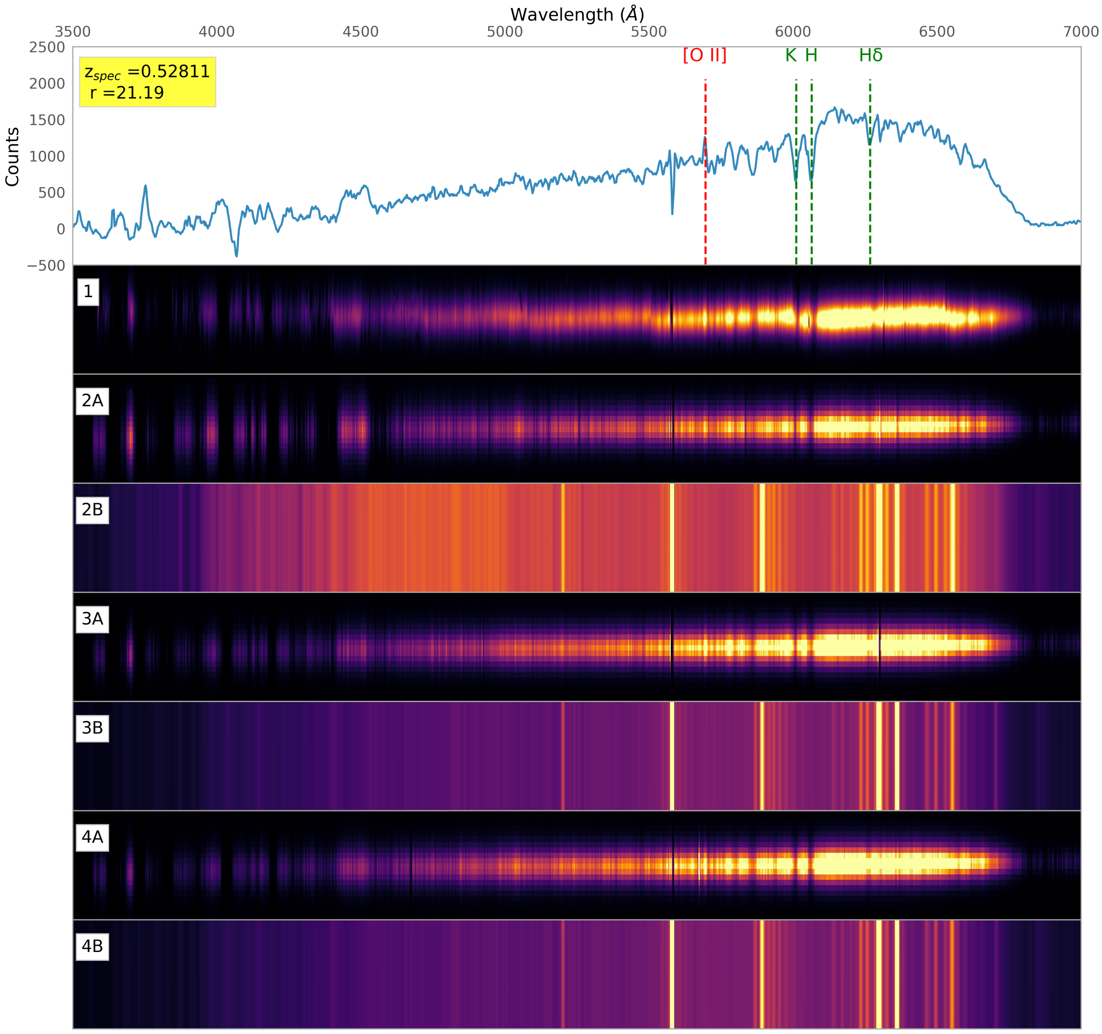

Figure 3.9: Top panel shows the 1D coadded spectrum with marked emission and absorption lines. The panel marked (1) shows the 2D coadded galaxy spectrum. The following three pairs of panels show single exposures of the 2D galaxy spectrum (A) and sky subtraction frames (B). Frames with the same number (i.e. frames 2A and 2B) are from the same exposure.

At the end of our data reduction, we are able to extract coadded 1D spectra for 72 out of 83 targeted objects. Of the spectra we cannot extract, 9 are lensed arcs and 2 are objects that have extremely poor sky subtraction. The 9 lensed arcs are very faint (average r band magnitude of 22.65) and are difficult to detect even when their spectra are coadded. As for the other 2 objects, both are relatively bright (r band magnitudes of 19.54 and 20.37) and are easy to detect on the individual science frames. However, the sky lines are over-subtracted in each individual frame and result in the subtraction of the object itself. We attempted several additional reduction runs and altered reduction parameters but were unable to remedy the over subtraction. As a result, we are able to successfully extract 87% of our target objects.

Chapter 4

Spectral Analysis

Using the reduced and coadded 1D spectra (Chapter 3), we measure the redshift of each galaxy from our Keck LRIS sample (Section 4.1). We do not recalculate the redshifts of galaxies from HectoMAP. We use two independent methods to measure the redshifts of the LRIS galaxies. Once we measure redshifts for the LRIS galaxies, we calculate the spectral ratio D_n4000 for both LRIS and HectoMAP galaxies (Section 4.2). We create our own `Python` script that calculates D_n4000 and propagates errors. Although the HectoMAP galaxies already have a D_n4000 value, we recalculate D_n4000 for consistency as a test for our own procedure.

4.1 Redshift Determination and Cluster Membership

Our first redshift determination method uses the Manual and Automatic Redshifting Software (`MARZ`) (Hinton et al. 2016). `MARZ` was originally developed for use with the Australian Dark Energy Survey (OzDES) to obtain accurate redshifts for a wide range of astronomical objects such as Type Ia supernova hosts, luminous red galaxies, and emission line galaxies, among others. OzDES uses the Anglo-Australian Omega (AAOmega) spectrograph which has a spectral resolution of R≈1000-10000 (Sharp et al. 2006). The resolution of AAOmega is on the same order of magnitude as LRIS, indicating `MARZ` should not have an issue resolving the spectral features of LRIS galaxies.

The `MARZ` software uses a modified cross-correlation algorithm from `AUTOZ` (Baldry et al. 2014). The cross-correlation function measures the similarity between two sets of data at different shifts or lags. In our case, the two sets of data are the observed and template spectra and the shift/lag is due to the redshifting of the observed spectra. To compute the cross-correlation function, the template and observed spectra are first discretely sampled into N bins. Both spectra are then continuum subtracted and filtered to remove low-frequency noise. The discrete Fourier transforms are then taken for the template and observed spectra (Tonry & Davis 1979). The template spectra are then slid along the observed spectra and the convolution product is calculated at each wavelength interval.

As a result, the `MARZ` cross-correlation function outputs a distribution of convolution values of the observed and template spectra as a function of wavelength. The peaks in the cross-correlation function represent wavelength shifts where the template and observed spectra match. The maximum correlation value represents the wavelength shift in which the template spectra and observed spectra are best aligned.

Once we know the wavelength shift of the observed spectra, we can calculate the redshift. The redshift of an object is calculated using the formula

$$z = \frac{\lambda_o - \lambda_e}{\lambda_e} \,, \tag{4.1}$$

where λ_o and λ_e are the observed and emitted wavelengths, respectively. The wavelength shift to redshift calculation is done automatically by `MARZ`.

Figure 4.1 shows an example of redshift determination using `MARZ`. Here we show a cluster member galaxy we observe with LRIS compared to a composite galaxy template. The composite

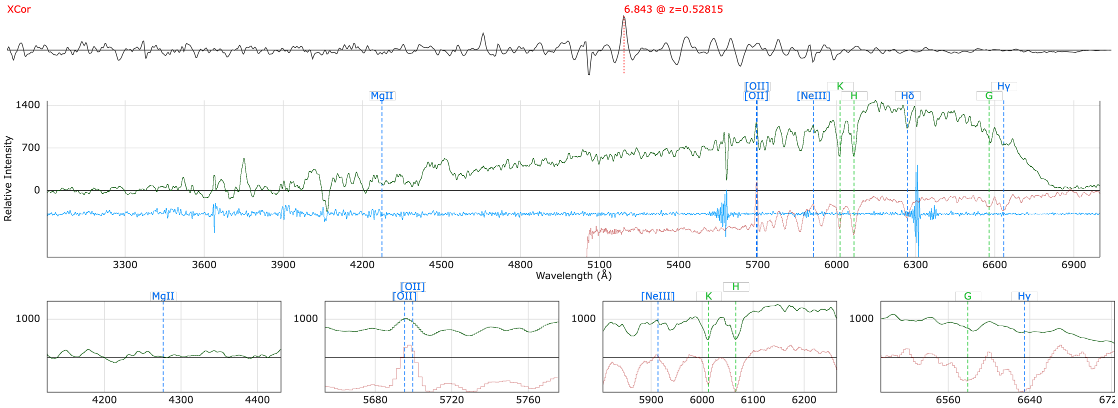

Figure 4.1: Example of redshfit determination using `MARZ`. The top panel shows the cross-correlation function (XCor) with a clear peak corresponding to a redshift of z = 0.528. The middle panel shows the observed spectrum (green), the template spectrum (red) and the sky subtraction of the observed spectrum (blue). Also in the middle panel are several prominent emission and absorption features. The bottom panel shows closeups of the prominent emission and absorption features.

template contains both emission and absorption features and represents a galaxy transitioning from star forming to quiescent. In our analysis, we use the template first selected by `MARZ` as the best match to our spectrum. We then also visually inspect other templates to confirm the best match template. In the top panel of Figure 4.1, we can see the convolution product from the cross-correlation algorithm. The peaks indicate wavelength shifts where the observed and template spectra are similar, with the largest peak representing the best match between the observed and template spectra.

All galaxy spectra templates used by `MARZ` can be found in Figure 6 of Hinton et al. (2016) and they range from stellar to galaxy to quasar spectra. One advantage of `MARZ` is the ability to zoom in on select regions of the spectra. This is especially useful for intrinsically faint objects. Depending on template selection, different spectral features will be used to match the template to the observed spectra.

In our analysis, we focus on matching absorption features as our sample consists of primarily quiescent galaxies. The most prominent absorption lines are the H and K CaII lines at rest frame wavelengths of 3968.47 Å and 3933.66 Å, respectively. The majority of galaxies (19) we find to be cluster members have visible H and K absorption lines, with most having very strong absorption at these wavelengths. Examples of these strong absorption galaxies can be found in the Appendix A.1.

A select few cluster member galaxies (6) have prominent OII doublet emission lines. Due to the resolution of our spectrograph, we can only observe the OII doublet as a single line at a rest frame wavelength of $\approx$ 3727.00 Å. Those with OII emission usually have weaker H and K absorption, resulting in us using the OII lines as the main spectral feature. Examples of these objects can be found in the Appendix A.1.

For some galaxy spectra, sky subtraction in `Pypeit` leaves residual sky line flux. The brightest sky emission line that is in our observational wavelength is the OI line at 5577.35 Å. This line is extremely prominent in all of our unreduced spectra. However, even after the data reduction process, some galaxy spectra still show remnants of this line. As a result, the OI sky line is sometimes misidentified as the OII doublet. This is not a major issue as we are aware of the poor sky subtraction and are able to visually identify remnant sky lines and avoid these lines when determining redshift.

The second method we use to measure redshifts is the `IDL` software `SpecPro`. `SpecPro` was developed to analyze faint spectra of galaxies and active galactic nuclei in the COSMOS field (Masters & Capak 2011). `SpecPro` uses an adapted cross-correlation algorithm that was originally written for SDSS. The functional form of the cross-correlation algorithm is likely marginally different from that of `MARZ`. However, we are unable to do a direct comparison as neither Hinton et al. (2016) nor Masters & Capak (2011) publish their cross-correlation algorithms. Even without a direction comparison of the algorithms, we know that both `SpecPro` and `MARZ` operate using the same cross-correlation theory (Tonry & Davis 1979).

One main difference between both software is in how they quantify the match between template spectra and observed spectra. Instead of reporting the convolution function as `MARZ` does, `SpecPro` reports the minimized χ^2 value. It is important to note that both the convolution values from `MARZ` and the χ^2 values from `SpecPro` both represent how well the template spectra match the observed spectra at each wavelength interval. The only difference is in the metric they use to report how well the template spectra match the observed spectra.

`SpecPro` also has a broad selection of templates ranging from strong emission galaxies to strong absorption galaxies to stellar spectra and quasars. As with `MARZ`, we mainly focus on matching the CaII H and K absorption lines, and if present the OII emission line, of observed spectra to template spectra.

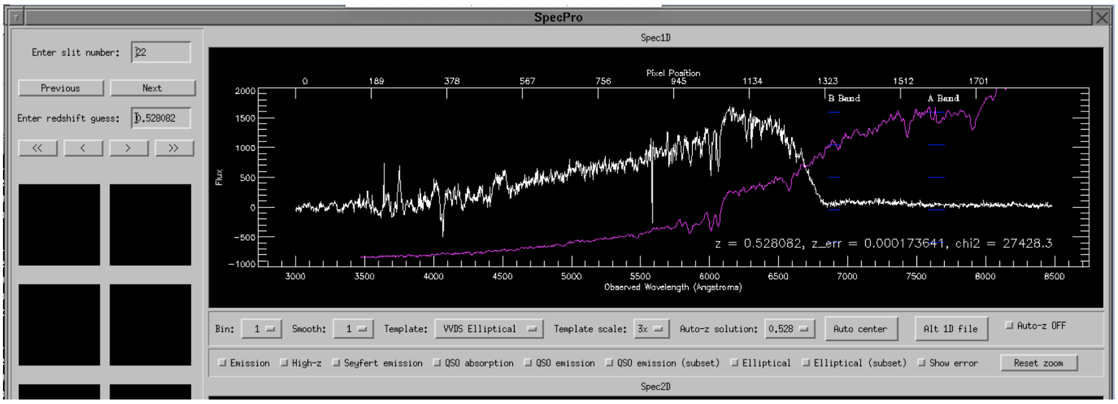

Enter slit number: 22

Enter redshift guess: 0.528082

z = 0.528082, z_err = 0.000173641, chi2 = 27428.3

Bin: 1 Smooth: 1 Template: VVDS Elliptical Template scale: 3x Auto-z solution: 0.528

Figure 4.2: Example of redshift determination using `SpecPro`. The observed galaxy spectrum (white) is shown against the template spectrum (purple). The automatic redshift solution along with errors and a χ^2 value are shown in the bottom right.

Figure 4.2 shows an example of redshift determination using `SpecPro`. The center panel shows the observed spectrum in white and the selected template spectrum in purple. When first loading a spectrum, the user can select the "Auto-z Solution" in which `SpecPro` will return the six best solution redshifts for the selected template. The user can easily cycle through the six best redshifts for that template and then switch to another template. For most of our objects, we would cycle through the templates and until we found one that matched the absorption or emission features of our observed spectra. We then would use the "Auto-z Solution" until the major features of the template overlapped with those of the observed spectra.

When comparing both `MARZ` and `SpecPro`, a drawback of `MARZ` is that there is no uncertainty associated with the calculated redshift. One of the major drawbacks of using `SpecPro` is the inability to zoom in on select regions of the spectrum. This was especially important when the observed spectrum had a low signal-to-noise ratio and the spectral features were very faint. It is because of this feature, that we use the `MARZ` redshift values for the remainder of our analysis. We use the `SpecPro` errors as an estimate of the redshift uncertainty.

Of the 72 objects for which we extract spectra (Section 3.1), we are able to calculate a redshift using either `MARZ` or `SpecPro` for all 72 objects. Out of 72 objects for which we calculate redshifts, 25 objects are at redshifts that are consistent with that of the galaxy cluster. Of the remaining 47, 10 are stellar interlopers, 6 are high redshift interlopers ($z \approx 0.6$), and 31 are low redshift interlopers ($0 \leq z \leq 0.5$). A spectroscopic redshift consistent with the cluster is sufficient to grant these galaxies cluster membership. The spectroscopic redshift error of these objects is much smaller than the velocity dispersion of the cluster. Therefore, we conclude all 25 of these objects are members of the galaxy cluster.

Our cluster of interest was initially identified in the HectoMAP survey and was found to have 32 spectroscopically confirmed members. With our follow up observations and data analysis we confirm 25 new spectroscopically confirmed cluster members. This represents a 78% increase in cluster membership and brings the total number of known cluster members to 57. We present all 57 spectroscopically confirmed cluster members in Table 4.1. We also show the 1D and 2D spectra for all LRIS cluster members in Appendix A.1.

Table 4.1: Properties of spectroscopically confirmed galaxy cluster members

R.A.	Dec.	$z_{MARZ}{}^1$	$z_{SpecPro}{}^2$	D_n4000^3	R_{cl}/R_{200}	$log_{10}(M_*/M_\odot)^4$	$log_{10}(R_{eff})^5$
247.439764	43.822285	0.52811	0.52808 ± 0.00017	1.52 ± 0.01	0.25 ± 0.03	$10.82^{+0.25}_{-0.26}$	0.678 ± 0.032
247.447263	43.856375	0.52705	0.52631 ± 0.00012	1.53 ± 0.01	1.19 ± 0.03	$10.88^{+0.21}_{-0.27}$	0.691 ± 0.058
247.460209	43.833598	0.53198	0.53184 ± 0.00011	1.70 ± 0.01	0.73 ± 0.03	$10.52^{+0.21}_{-0.23}$	0.401 ± 0.015
247.442601	43.848417	0.52967	0.52955 ± 0.00014	1.84 ± 0.02	0.85 ± 0.03	$11.05^{+0.29}_{-0.19}$	0.700 ± 0.020
247.417143	43.824986	0.53018	0.52973 ± 0.00012	1.71 ± 0.01	0.57 ± 0.03	$10.75^{+0.11}_{-0.17}$	0.389 ± 0.039
247.461386	43.856980	0.53094	0.53051 ± 0.00001	1.18 ± 0.01	1.36 ± 0.03	$9.51^{+0.30}_{-0.24}$	0.404 ± 0.031
247.436304	43.849075	0.52716	0.52606 ± 0.00047	1.76 ± 0.04	0.85 ± 0.03	$10.65^{+0.16}_{-0.20}$	0.523 ± 0.198
247.448858	43.834449	0.52959	0.52809 ± 0.00017	1.74 ± 0.03	0.45 ± 0.03	$10.62^{+0.27}_{-0.24}$	0.535 ± 0.045
247.453838	43.843891	0.53740	0.53805 ± 0.00001	1.06 ± 0.01	0.80 ± 0.03	$9.3^{+0.25}_{-0.26}$	0.558 ± 0.065
247.449075	43.854239	0.52822	0.52841 ± 0.00020	1.30 ± 0.04	1.11 ± 0.03	$9.75^{+0.34}_{-0.32}$	0.931 ± 0.075
247.452979	43.857650	0.52992	0.53000 ± 0.00001	1.06 ± 0.01	1.28 ± 0.03	$9.48^{+0.31}_{-0.32}$	0.473 ± 0.070
247.445343	43.853748	0.53792	0.53813 ± 0.00026	1.46 ± 0.03	1.07 ± 0.03	$9.97^{+0.46}_{-0.47}$	0.502 ± 0.009
247.421041	43.844545	0.52740	0.52706 ± 0.00032	1.49 ± 0.03	0.80 ± 0.03	$10.18^{+0.31}_{-0.32}$	0.326 ± 0.095
247.430965	43.821909	0.53307	0.53266 ± 0.00019	1.70 ± 0.02	0.29 ± 0.03	$10.25^{+0.29}_{-0.36}$	0.380 ± 0.084
247.428056	43.817335	0.52821	0.52783 ± 0.00018	1.61 ± 0.02	0.49 ± 0.03	$10.34^{+0.33}_{-0.31}$	0.237 ± 0.103
247.439267	43.826324	0.53196	0.53272 ± 0.00023	1.57 ± 0.02	0.11 ± 0.03	$10.38^{+0.18}_{-0.21}$	0.007 ± 2.577
247.481543	43.837080	0.53392	-	1.49 ± 0.03	1.37 ± 0.03	$7.02^{+0.09}_{-0.02}$	0.366 ± 0.141
247.395519	43.803017	0.53227	0.53041 ± 0.00035	1.57 ± 0.03	1.56 ± 0.03	$10.58^{+0.35}_{-0.37}$	0.643 ± 0.059
247.481079	43.813323	0.53293	0.53224 ± 0.00011	1.83 ± 0.02	1.43 ± 0.03	$10.78^{+0.29}_{-0.36}$	0.741 ± 0.038
247.453005	43.803898	0.52545	0.52475 ± 0.00011	1.63 ± 0.01	1.08 ± 0.03	$10.93^{+0.24}_{-0.24}$	0.351 ± 0.147
247.398146	43.820813	0.52728	0.52708 ± 0.00001	1.73 ± 0.03	1.18 ± 0.03	$11.23^{+0.49}_{-0.19}$	-
247.486052	43.831115	0.53235	0.53121 ± 0.00456	1.44 ± 0.03	1.45 ± 0.11	$9.98^{+0.35}_{-0.34}$	0.405 ± 0.062
247.469968	43.776610	0.52929	0.52954 ± 0.00011	1.14 ± 0.02	2.27 ± 0.03	$8.82^{+0.55}_{-0.41}$	0.614 ± 0.053
247.425366	43.788531	0.52993	0.52963 ± 0.00019	1.57 ± 0.02	1.62 ± 0.03	$10.14^{+0.33}_{-0.37}$	-0.292 ± -0.150
247.422468	43.769037	0.53131	0.53073 ± 0.00017	1.13 ± 0.03	2.41 ± 0.03	$8.86^{+0.55}_{-0.52}$	0.412 ± 0.097
247.318852	43.816336	0.52943 ± 0.00012	-	1.31 ± 0.07	3.45 ± 0.03	$10.42^{+0.25}_{-0.19}$	0.734 ± 0.029
247.327933	43.849471	0.52922 ± 0.00017	-	1.63 ± 0.11	3.27 ± 0.03	$11.31^{+0.14}_{-0.18}$	1.309 ± 0.061
247.354174	43.807326	0.53020 ± 0.00023	-	1.74 ± 0.12	2.53 ± 0.03	$10.97^{+0.19}_{-0.21}$	0.786 ± 0.006
247.366299	43.775129	0.53009 ± 0.00001	-	1.09 ± 0.03	2.97 ± 0.03	$10.15^{+0.17}_{-0.15}$	0.688 ± 0.027
247.366656	43.804872	0.53250 ± 0.00019	-	2.23 ± 0.23	2.23 ± 0.03	$11.77^{+0.08}_{-0.16}$	1.146 ± 0.030
247.368886	43.808024	0.52785 ± 0.00017	-	1.66 ± 0.09	2.11 ± 0.03	$11.25^{+0.16}_{-0.17}$	0.882 ± 0.021

Table 4.1 *continued*

R.A.	Dec.	$z_{MARZ}{}^1$	$z_{SpecPro}{}^2$	D_n4000^3	$log_{10}(M_*/M_\odot)^4$	$log_{10}(R_{eff})^5$	
247.381950	43.756516	0.52985 ± 0.00029	-	1.58 ± 0.16	3.28 ± 0.03	$10.76^{+0.17}_{-0.21}$	0.670 ± 0.357
247.386548	43.810869	0.52684 ± 0.00014	-	1.83 ± 0.11	1.60 ± 0.03	$11.34^{+0.09}_{-0.16}$	0.822 ± 0.214
247.392331	43.821022	0.52942 ± 0.00001	-	1.79 ± 0.05	1.31 ± 0.03	$12.08^{+0.05}_{-0.05}$	1.575 ± 0.043
247.401843	43.831851	0.52905 ± 0.00017	-	1.83 ± 0.11	1.02 ± 0.03	$11.47^{+0.14}_{-0.20}$	0.545 ± 0.009
247.407724	43.852781	0.53237 ± 0.00015	-	1.52 ± 0.06	1.30 ± 0.03	$10.91^{+0.22}_{-0.22}$	0.873 ± 0.035
247.412307	43.768818	0.52945 ± 0.00001	-	1.02 ± 0.01	2.49 ± 0.03	$9.62^{+0.06}_{-0.06}$	0.166 ± 0.065
247.413552	43.813461	0.52620 ± 0.00013	-	1.74 ± 0.13	0.88 ± 0.03	$10.94^{+0.19}_{-0.23}$	0.636 ± 0.050
247.421036	43.826942	0.52749 ± 0.00014	-	1.55 ± 0.09	0.45 ± 0.03	$11.16^{+0.10}_{-0.17}$	0.813 ± 0.023
247.423042	43.770951	0.52472 ± 0.00001	-	1.44 ± 0.04	2.32 ± 0.03	$10.86^{+0.14}_{-0.18}$	0.741 ± 0.063
247.424463	43.810664	0.52780 ± 0.00013	-	1.76 ± 0.06	0.78 ± 0.03	$10.90^{+0.11}_{-0.17}$	0.975 ± 0.102
247.425172	43.822893	0.52902 ± 0.00012	-	1.86 ± 0.12	0.38 ± 0.03	$11.07^{+0.12}_{-0.17}$	0.913 ± 0.085
247.425342	43.827910	0.52760 ± 0.00014	-	1.99 ± 0.14	0.32 ± 0.03	$10.95^{+0.13}_{-0.15}$	1.480 ± 0.238
247.426189	43.828055	0.52818 ± 0.00014	-	2.20 ± 0.19	0.29 ± 0.03	$11.91^{+0.17}_{-0.19}$	2.033 ± 0.628
247.437524	43.842935	0.52739 ± 0.00021	-	0.86 ± 0.05	0.61 ± 0.03	$11.37^{+0.11}_{-0.18}$	1.128 ± 0.034
247.440512	43.867679	0.53325 ± 0.00012	-	1.74 ± 0.07	1.61 ± 0.03	$11.22^{+0.21}_{-0.21}$	0.922 ± 0.032
247.443780	43.787934	0.53000 ± 0.00018	-	1.35 ± 0.05	1.62 ± 0.03	$10.63^{+0.21}_{-0.23}$	0.607 ± 0.025
247.444661	43.842634	0.52886 ± 0.00018	-	2.18 ± 0.14	0.64 ± 0.03	$10.82^{+0.20}_{-0.21}$	0.557 ± 0.134
247.447677	43.808048	0.52416 ± 0.00014	-	1.83 ± 0.20	0.87 ± 0.03	$11.49^{+0.11}_{-0.12}$	0.930 ± 0.026
247.454767	43.868353	0.52550 ± 0.00013	-	1.32 ± 0.07	1.72 ± 0.03	$10.75^{+0.21}_{-0.18}$	0.601 ± 0.022
247.455506	43.854911	0.52751 ± 0.00010	-	1.33 ± 0.05	1.21 ± 0.03	$10.54^{+0.13}_{-0.14}$	0.673 ± 0.025
247.456052	43.839631	0.53163 ± 0.00019	-	1.82 ± 0.10	0.74 ± 0.03	$11.78^{+0.11}_{-0.14}$	1.340 ± 0.128
247.461254	43.839240	0.52897 ± 0.00018	-	2.19 ± 0.15	0.86 ± 0.03	$11.17^{+0.11}_{-0.16}$	0.765 ± 0.037
247.461344	43.850295	0.52746 ± 0.00012	-	1.88 ± 0.13	1.16 ± 0.03	$11.22^{+0.10}_{-0.18}$	0.733 ± 0.014
247.471046	43.833668	0.52923 ± 0.00011	-	1.57 ± 0.06	1.03 ± 0.03	$11.62^{+0.15}_{-0.18}$	0.777 ± 0.029
247.479285	43.832218	0.53857 ± 0.00012	-	1.32 ± 0.08	1.26 ± 0.03	$10.66^{+0.23}_{-0.23}$	0.712 ± 0.031
247.494810	43.889651	0.53063 ± 0.00011	-	1.40 ± 0.07	3.02 ± 0.03	$10.36^{+0.22}_{-0.23}$	0.774 ± 0.017

[1] Redshift calculated using `MARZ` software, for HectoMAP galaxies value shown indicates the catalog spectroscopic redshift.

[2] Redshift calculated using `SpecPro` software. This value is left blank for HectoMAP galaxies.

[3] D_n4000 calculated for both LRIS and HectoMAP galaxies using our python script

[4] Stellar mass calculated using `LePhare` (Section 2.3.1)

[5] Effective radius, in units of kpc, calculated using `SExtractor` (Section 2.4)

A break is placed in the table to separate Keck LRIS objects (above the break) from HectoMAP objects (below the break).

4.2 D_n4000 Calculation

Over time, the stellar population within an individual galaxy evolves. This evolution can be detected in the galaxies spectrum. With our spectroscopic data, we can calculate the D_n4000 spectral index. D_n4000 is a spectral ratio of the red side (4000Å to 4100Å) to the blue side (3850Å to 3950Å) of a galaxy's spectrum (Balogh et al. 1999). This ratio is centered around 4000Å due to the spectral break at that wavelength from metal absorption lines (Kim et al. 2022). D_n4000 is defined as

$$D_n4000 = \frac{\overline{f^R}}{\overline{f^B}} = \frac{(\lambda_2^B - \lambda_1^B) \int_{\lambda_1^R}^{\lambda_2^R} f_\nu d\lambda}{(\lambda_2^R - \lambda_1^R) \int_{\lambda_1^B}^{\lambda_2^B} f_\nu d\lambda}, \tag{4.2}$$

where $\overline{f^R}$ and $\overline{f^B}$ are the average flux densities in the red (4000Å to 4100Å) and blue (3850Å to 3950Å) region of spectrum, respectively.

Figure 4.3 shows how D_n4000 evolves with stellar age and varies with different metallicities. This model of evolving D_n4000 and stellar age uses the Flexible Stellar Population Synthesis (FSPS) package (Conroy et al. 2009; Conroy & Gunn 2010). We create our model as a simple stellar population (SSP). In a SSP, all stars are created at the same time and have the same initial elemental composition. For the initial mass function (IMF), we use the widely accepted Kroupa (2001) IMF. Since D_n4000 is centered about a spectral break that is caused by metal absorption lines, the metallicity of a galaxy slightly affects the D_n4000 value (as shown by the different colored points in Figure 4.3). However, regardless of the metallicity, we can see in Figure 4.3 that D_n4000 evolves with stellar age at a similar rate.

By measuring D_n4000, we can estimate the age of the stellar population within cluster member galaxies. A smaller D_n4000 (<1.5), indicates that the stellar population of a galaxy is relatively young and recently formed ($<$ 1 Gyr), whereas a larger D_n4000 (>1.5), indicates that the stellar population of a galaxy is older ($>$ 1 Gyr) (Kauffmann et al. 2003).

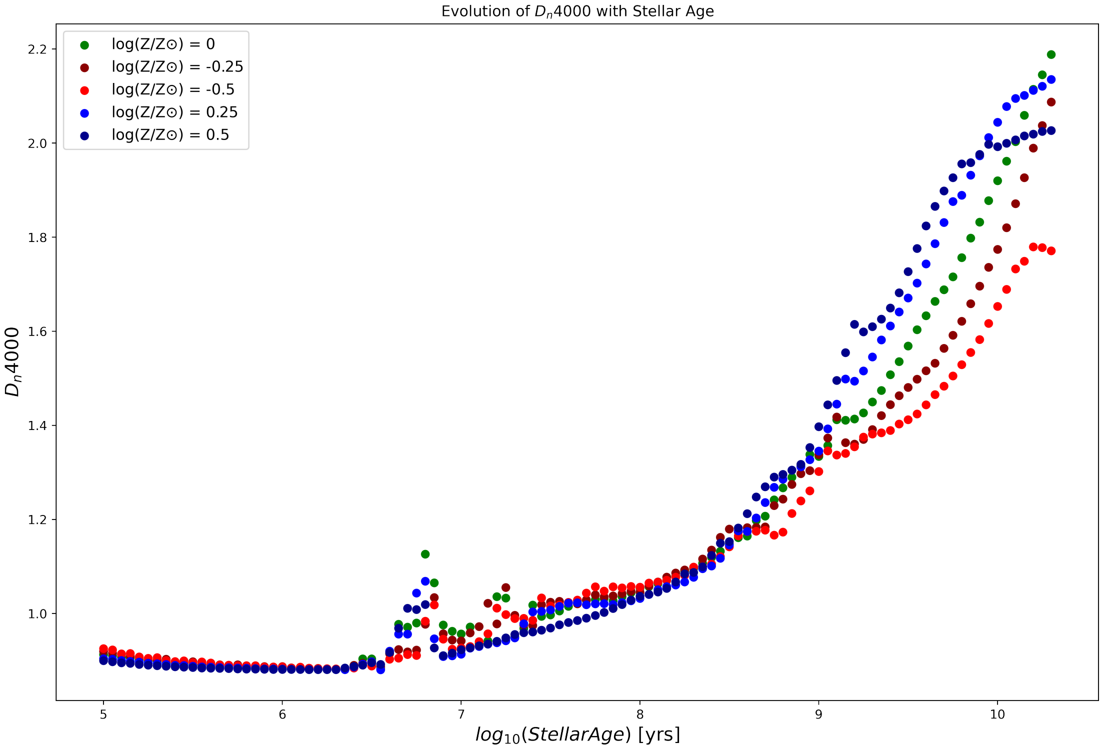

Figure 4.3: D_n4000 as a function of age of stellar populations created using `FSPS`. The different colored points represent different stellar metallicities of the stars produced in the model. We can see that as D_n4000 increases, regardless of metallicity, the stellar age also increases. We use the D_n4000 index of a galaxy as a proxy for the age of the stellar population within a galaxy. We can see that a D_n4000 of 1.5 corresponds to an average stellar population age of 1 Gyr.

We develop our own script to measure the D_n4000 of our spectroscopic cluster member galaxies. An example of how our script measures D_n4000 is shown in Figure 4.4. For both LRIS and HectoMAP cluster member galaxies, our D_n4000 script first reads in the masked 1D spectra and redshifts for all objects. For LRIS galaxies, we mask the spectra using the mask that is output from the `Pypeit` data reduction process. HectoMAP galaxies are masked using the mask that is output from the Hectospec data reduction pipeline. The observed spectra are then shifted to the rest frame. An example of the observed and rest frame masked spectra can be seen in the top panel of Figure 4.4.

It is important to note that the HectoMAP spectra are fluxed whereas the LRIS spectra are unfluxed. Fluxing corrects for the sensitivity as a function of wavelength of different spectrographs by using standard stars with well-known flux. To ensure that using fluxed and unfluxed

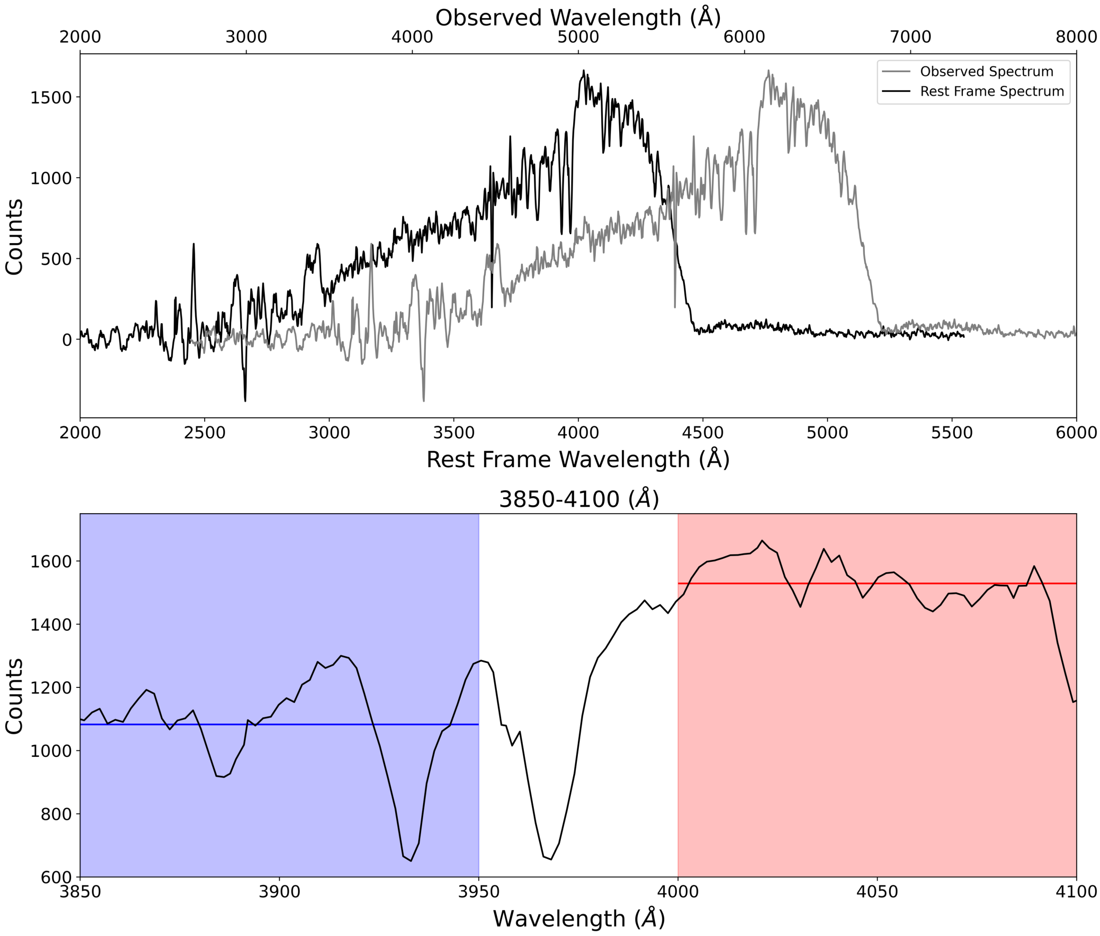

Figure 4.4: Galaxy spectrum shown as an example of how D_n4000 is measured for spectroscopic objects. The top panel shows both the observed spectrum (grey) and the rest frame spectrum (black). The bottom panel shows an example of how we calculate D_n4000 for each spectroscopic cluster member. We calculate the average flux density in both the red (4000Å to 4100Å) and blue (3850Å to 3950Å) parts of the spectrum. Taking the ratio of red to blue flux density gives us D_n4000. It is important to note that D_n4000 is calculated in units of frequency, although in this figure we show the galaxy spectrum in units of wavelength for familiarity.

spectra does not influence our results, we compare D_n4000 values obtained from fluxed and unfluxed HectoMAP spectra. We find that the median difference in D_n4000 between fluxed and unfluxed spectra is $\approx$ 0.05. However, the median D_n4000 error of all spectroscopic members (HectoMAP and LRIS) is $\approx$ 0.06. Assuming that the sensitivities of the two spectrographs are the same at the wavelengths used for D_n4000, the fact that the LRIS spectra are not fluxed does not affect our D_n4000 measurements.

Once in the rest frame, our script selects both the red (4000Å to 4100Å) and blue (3850Å to 3950Å) parts of the spectrum and converts these regions to units of frequency. The average flux density, f_ν, is calculated in both the red and blue parts of the spectrum. The bottom panel of Figure 4.4 shows our selection of the red and blue region of the spectrum as well as calculating the average flux density. It is important to note that in Figure 4.4 we show the spectrum in units of f_λ, we do so as spectra are commonly shown in units of wavelength. With the average flux density, f_ν, from both parts of the spectrum, we take the ratio of red to blue and the result is the D_n4000 of the galaxy. The uncertainty on our D_n4000 measurements is calculated by following the equation

$$\Delta D_n4000 = \sqrt{\left(\frac{1}{\overline{f^B}} * \sigma_B\right)^2 + \left(-\frac{\overline{f^R}}{\overline{f^B}^2} * \sigma_R\right)^2}, \tag{4.3}$$

where σ_B and σ_R are the uncertainty on the blue and red flux density, respectively.

We recalculate D_n4000 for the 32 cluster members from the HectoMAP survey and find that our values agree, within uncertainties, with the previously calculated D_n4000 values done by (Sohn et al. 2021a).

We show our results in the context of $g - r$ vs r in Figure 4.5. Each point is a spectroscopic object that is colored by its calculated D_n4000 value. We can see that, on average, as $g - r$ increases so does the D_n4000 of that object. Additionally, we also see that brighter objects typically have larger D_n4000 than fainter objects. We find that the majority of galaxies (37 out of 57) have D_n4000 greater than 1.5, indicating that these galaxies host stellar populations that are older than 1 Gyr. This is not surprising as galaxies within clusters are expected to have older stellar populations as we discuss in Section 1.2.3.

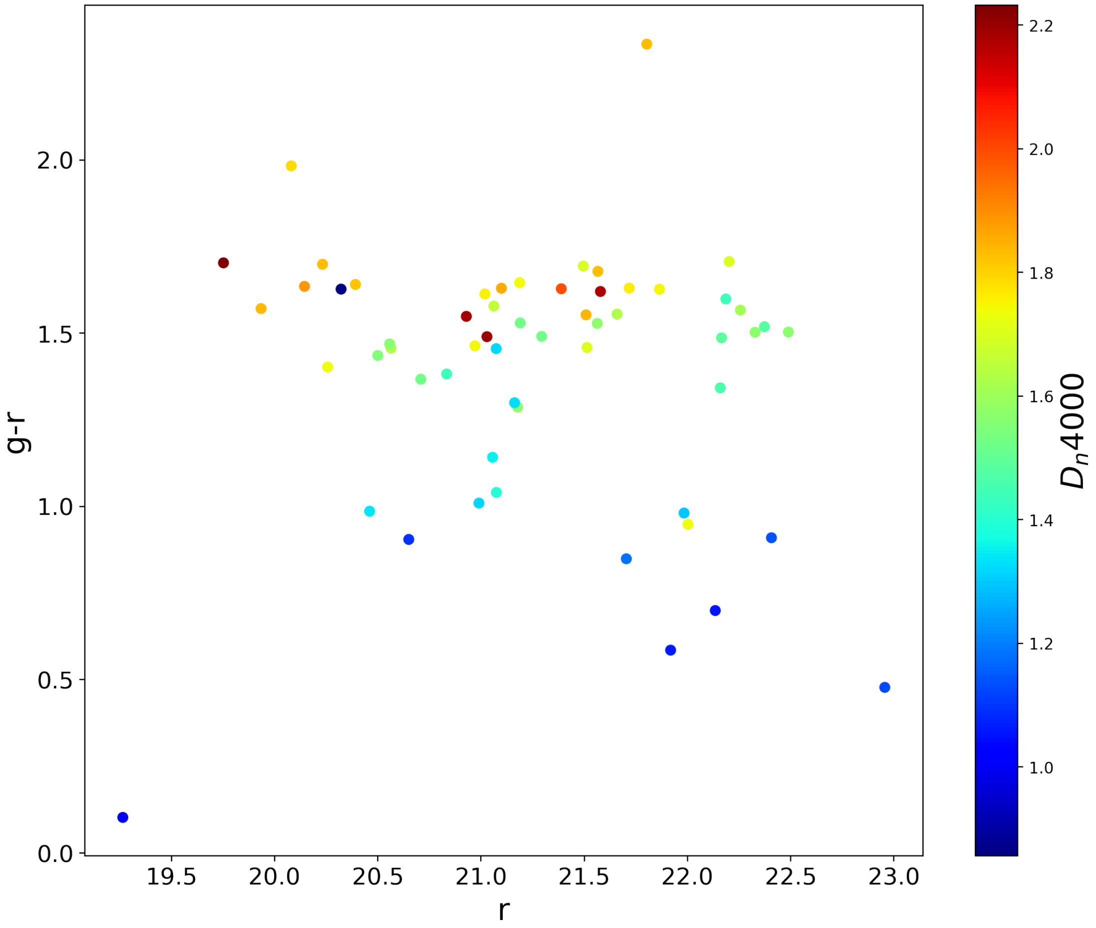

Figure 4.5: Color-magnitude diagram for all spectroscopic cluster members colored by D_n4000. We present the results of our D_n4000 values in the context of $g-r$ vs. r. We find that as D_n4000 of an object increases, so does this $g-r$ color and the r band apparent magnitude.

Chapter 5

Assignment of Spectroscopic Properties to Photometric Cluster Member Candidates

We select a sample of photometric cluster member candidates from the PDR 3 photometric catalog of HSC-SSP. We use these photometric cluster member candidates to create a statistical correction for the galaxy cluster members we are missing from our magnitude limited ($r \leq 21.3$) spectroscopic sample. Our statistical correction is based on assigning spectroscopic properties, such as D_n4000, to our sample of photometric cluster member candidates. In Section 5.1 we discuss how we use Kernel Density Estimation to assign properties. In Section 5.2 we show how outliers are removed from our sample of photometric cluster member candidates. In Section 5.3 we remove photometric cluster member candidates that have a high probability of being stellar interlopers. In Section 5.4 we assign r band $k-$corrections to photometric cluster member candidates. In Section 5.5 we calculate R_{cl}/R_{200}. Lastly, in Section 5.6 we assign D_n4000 values to photometric cluster member candidates.

5.1 KDE Sampling of Photometric Members

To create a statistical correction for missing cluster member galaxies, we the use photometric cluster member candidates discussed in Section 2.2.1. We use Kernel Density Estimation (KDE; Rosenblatt 1956) to assign spectroscopic properties to photometric cluster member candidates. This assumes that our sample of spectroscopic cluster members is representative of the cluster population. With this assumption, we can create a multi-dimensional probability density function (PDF) from our known spectroscopic cluster members. Using that PDF we are able to assign spectroscopic properties to photometric cluster member candidates.

KDE is a non-parametric approach that allows us to infer the PDF from a data sample. Since it is non-parametric, we do not have to assume that our data follow a specific model (e.g. Gaussian, Uniform, Epanechnikov). The KDE, given a set of measurements x_i, is defined as

$$\hat{f}_N(x) = \frac{1}{Nh^D} \sum_{i=1}^{N} K \frac{d(x, x_i)}{h} \ , \tag{5.1}$$

where N is the number of data points, h is the bandwidth, D is the number of dimensions, $K(u)$ is the kernel function (e.g. Gaussian, Uniform, Epanechnikov), and $d(x, x_i)$ is the distance between the data point x_i and the point x where we want to know the estimated density. We use a Gaussian kernel function for our KDE analysis. The bandwidth defines the smoothness of the resultant KDE distribution. If the bandwidth is too large, the data will be underfit and important features will be smoothed out. If the bandwidth is too small, the data will be overfit and features will become meaningless. It has been shown that the bandwidth is a more critical parameter than the kernel function (Pojmanski 2002; Ivezić et al. 2014). We use the Scikit-learn (Pedregosa et al. 2011) package `GridsearchCV` for bandwidth selection. The `GridsearchCV` package tries all combinations of the given range of bandwidth values. After trying each combination, the output is the bandwidth value with the best performance. By using `GridsearchCV` to find the bandwidth, we are ensuring that the data are not being over or underfitted.

To check how well our KDE follows the true distribution of data, we marginalize the KDE. Marginalizing a KDE is simply integrating across all dimensions except for the dimension of interest, resulting in a marginalized PDF representing the dimension of interest. By examining this PDF we are able to see how well the data is represented by the KDE.

Throughout our analysis we create multiple KDEs. We create a 4D KDE to assign r band $k-$corrections to photometric cluster member candidates (Section 5.4), in order to calculate absolute magnitudes for spectroscopic members and photometric cluster member candidates. We also create a 2D KDE that we use to assign D_n4000 to photometric cluster member candidates (Section 6.2). Lastly, we create a 2D KDE to represent the distribution of size-stellar mass slopes and zeropoints (Section 6.2).

5.2 Confirmining Photometric Cluster Member Candidates

The sample of photometric cluster member candidates we obtain in Section 2.2.1, contains many galaxies that are not associated with our cluster of interest. We remove clear outliers from our sample of photometric cluster member candidates based on their radial velocity in comparison to the clusters velocity dispersion. To do this, we first calculate the radial line of sight velocity, v, of our 57 spectroscopic members using the formula

$$v = \frac{z_{spec} - z_{cluster}}{1 + z_{cluster}} c \, , \tag{5.2}$$

where z_{spec} is the objects spectroscopic redshift, $z_{cluster}$ is the cluster redshift, and c is the speed of light.

Using the distribution of radial line of sight velocities for spectroscopic cluster members (Figure 5.1), we investigate two methods of calculating the clusters velocity dispersion. Our

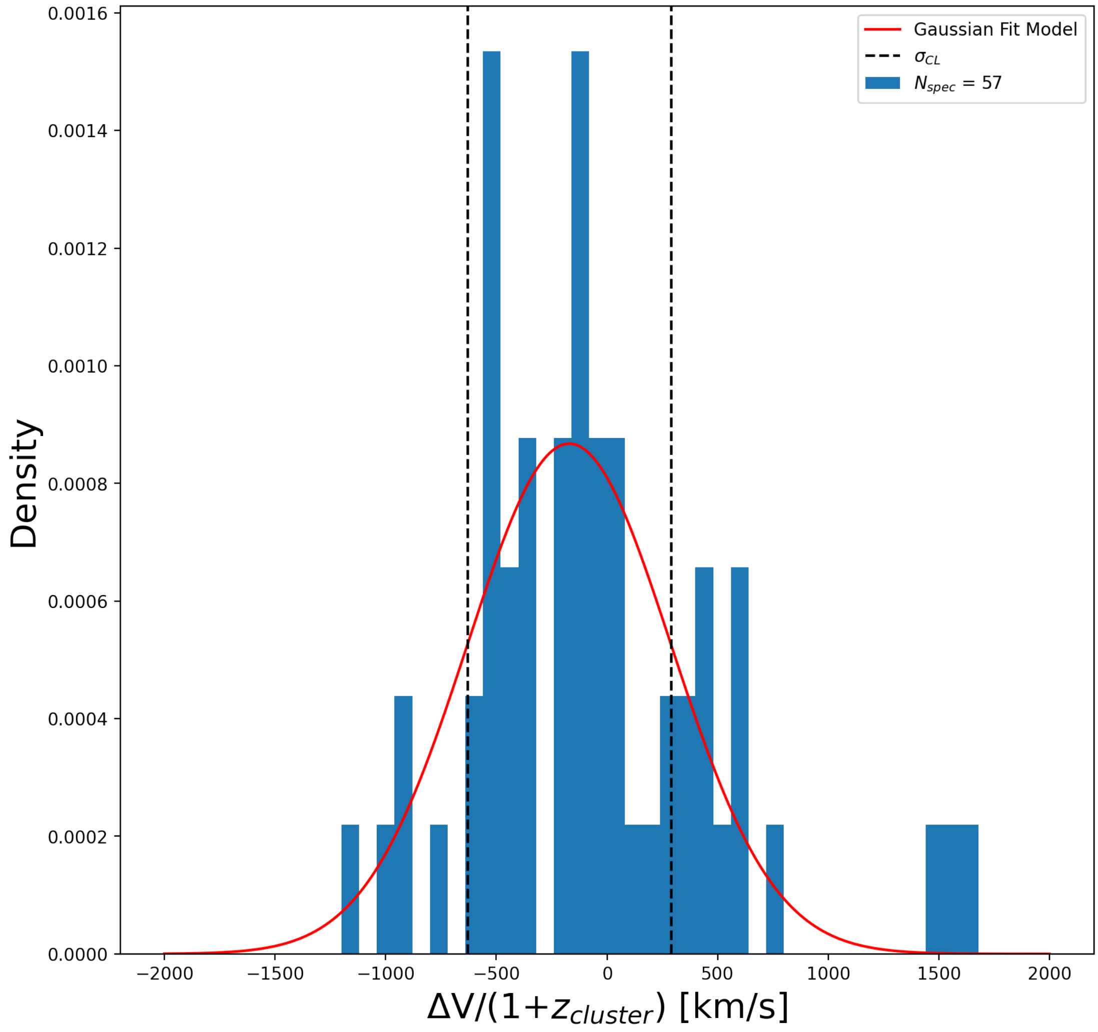

Figure 5.1: 1D histogram showing the distribution of radial line of sight velocities for all spectroscopic members. The Gaussian fit is shown in red. The width of the Gaussian, which we define here as the cluster velocity dispersion, is shown as the black dashed lines.

first method is simply fitting a Gaussian to the distribution of radial velocities of spectroscopic members. The Guassian fit is shown as the red curve in Figure 5.1, and the scale of the distribution is shown by the black dashed lines. We define the scale of the distribution of spectroscopic members radial line of sight velocities to be the cluster velocity dispersion ($\sigma_{CL-Gauss}$). We find the cluster velocity dispersion to be $\sigma_{CL-Gauss} = 459 \pm 85$ km/s.

By modeling the the distribution of radial line of sight velocities of cluster members as a Gaussian, we are assuming that the cluster is in a state of dynamical equilibrium. This may not be the most realistic assumption as we know that clusters at $z \approx 0.5$ are still actively assembling

(Cohn & White 2005; Berrier et al. 2009; Kravtsov & Borgani 2012). Furthermore, there are indications that our cluster is a merging cluster. If our cluster is still assembling and undergoing a merger, it is likely that the population distribution of line of sight radial velocities is non Gaussian.

Our second method of calculating the cluster velocity dispersion takes into account the possibility of having a non Gaussian distribution. To do this, we use the biweight estimate of scale, as presented by Beers et al. (1990). The biweight estimate of scale, $\sigma_{CL-biweight}$, is given by the formula

$$\sigma_{CL-biweight} = n^{\frac{1}{2}} \frac{[\Sigma_{|u_i|<1}(v_i - M)^2(1 - u_i^2)^4]^{\frac{1}{2}}}{|\Sigma_{|u_i|<1}(1 - u_i^2)(1 - 5u_i^2)|} \ , \tag{5.3}$$

where n is the sample size, v_i is the radial line of sight velocity for each spectroscopic member, and M is the sample median. u_i is defined as

$$u_i = \frac{(v_i - M)}{c * MAD} \ , \tag{5.4}$$

where c is a 'tuning constant', set to 9.0 as recommended in Beers et al. (1990), and $MAD = median(|v_i - M|)$. Using Equation 5.3, we find the cluster velocity dispersion to be $\sigma_{CL-biweight} = 466 \pm 60$ km/s.

Both methods, the Gaussian fit and the biweight, give similar results for the cluster velocity dispersion. However, for the remainder of our analysis, we use the cluster velocity dispersion obtained from the Gaussian fit. We do so in order to be conservative when confirming photometric cluster member candidates.

We then use the cluster velocity dispersion ($\sigma_{CL-Gauss} = 459 \pm 85$ km/s) to remove outliers from the sample of photometric cluster member candidates. We consider photometric cluster member candidates that are within $\pm 3\sigma_{CL-Gauss}$. This corresponds to a line of sight radial velocity range of ± 1377 km/s and a redshift range of $z = 0.53 \pm 0.007$. This is a narrow redshift range and photometric cluster member candidates have redshift uncertainties much larger than this range. To account for this, we look at the most probable redshift from the PDR 3 photometric catalog of the HSC-SSP, as well as the upper 68th and 95th percentile and the lower 68th and 95th percentile of the photometric redshift distribution. By doing so, we calculate 5 radial velocities for each photometric cluster candidate. If any of those 5 radial velocities are within $\pm 3\sigma_{CL-Gauss}$ of the cluster center, we add that object to our photometric cluster member candidate catalog. After selecting photometric objects based on redshifts that fall within the cluster redshift interval, we have a catalog of 266 photometric cluster member candidates. From this point forward when we reference photometric redshifts we use the most probable redshift from PDR 3 HSC-SSP.

As a result of this approach, we have a wide distribution of photometric redshifts. Figure 5.2 shows the distribution of photometric cluster member candidate redshifts (pink histogram) in comparison to the cluster redshift interval (blue hashed region), defined by the maximum and minimum redshift of spectroscopic members. To make our sample more resilient against these outliers, we used the `Astopy` (Astropy Collaboration et al. 2022) tool `Sigma Clip`. `Sigma Clip` calculates the mean photometric redshift of our sample and then removes objects that are more than a certain number of standard deviations away from the photometric mean. The mean photometric redshift of the photometric cluster member candidates is recalculated, and again objects more than a certain number of standard deviations away from the mean are removed. This process is repeated until there are no more objects to be removed. In our case we choose to remove objects that are more than 3 standard deviations away from the mean. Figure 5.2 shows the results of `Sigma Clip`. The pink histogram is the photometric catalog before sigma clipping, the blue histogram is the photometric catalog after sigma clipping. The black dashed line is the redshift of the cluster.

Before sigma clipping, our sample of photometric cluster member candidates contains 266 objects. After sigma clipping, our sample contains 243 photometric cluster member candidates. We then remove photometric cluster member candidates with $g - r > 1.0$ to match the completeness of HectoMAP. Lastly, we remove objects that have been confirmed as spectroscopic members. As a result, our sample of photometric cluster member candidates contains 119 objects.

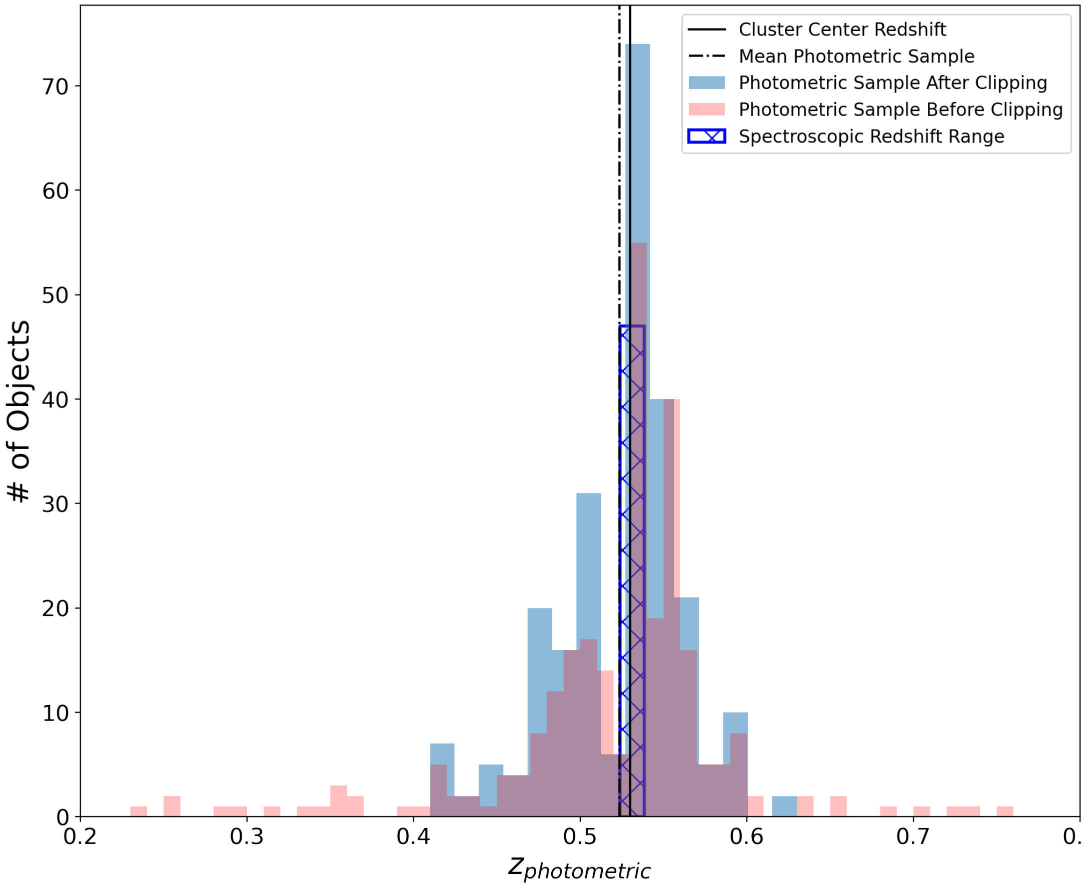

Figure 5.2: 1D histogram of photometric sample redshifts before (red) and after (blue) sigma clipping. The cluster redshift is shown as the black dashed line. We used a 3 σ upper and lower threshold in photometric redshift when clipping.

5.3 Stellar Interlopers

With our sigma clipped sample of photometric cluster member candidates (Section 5.2), we now remove stellar interlopers from our sample of photometric cluster member candidates. We obtain size measurements for our photometric cluster member candidates using `SExtractor` (Section 2.4). In addition to sizes, `SExtractor` also outputs a parameter called `Class Star`, which estimates the probability that an object is a galaxy or a star. `Class Star` values range from 0.0 for a galaxy to 1.0 for a star, a value of 0.5 indicates the object has an equal probability of being a galaxy or star. Several photometric cluster member candidates have `Class Star` greater than 0.5. In order to determine where to place our `Class Star` cut, we visually examine each object.

We create a *RGB* image of each photometric cluster member candidate using the *g*, *r*, and *i* band images obtained from the PDR 3 photometric catalog of HSC-SSP. The *RGB* images are shown in Figure 5.3, with spectroscopic members shown in the top row, photometric cluster member candidates in the middle row, and photometric objects determined to be stars in the bottom row. We inspect each photometric cluster member candidate *RGB* image along with the associated `Class Star` value. From this inspection, we decide to remove any photometric cluster member candidate with a `Class Star` value greater then 0.8. As a result, our sample of photometric cluster member candidates now contains 94 galaxies. The bottom row of Figure 5.3 shows an example of objects removed from the photometric cluster member candidate based on `Class Star` value. It is clear that the objects with `Class Star` greater than 0.8 are very compact objects, indicating they are likely stellar interlopers.

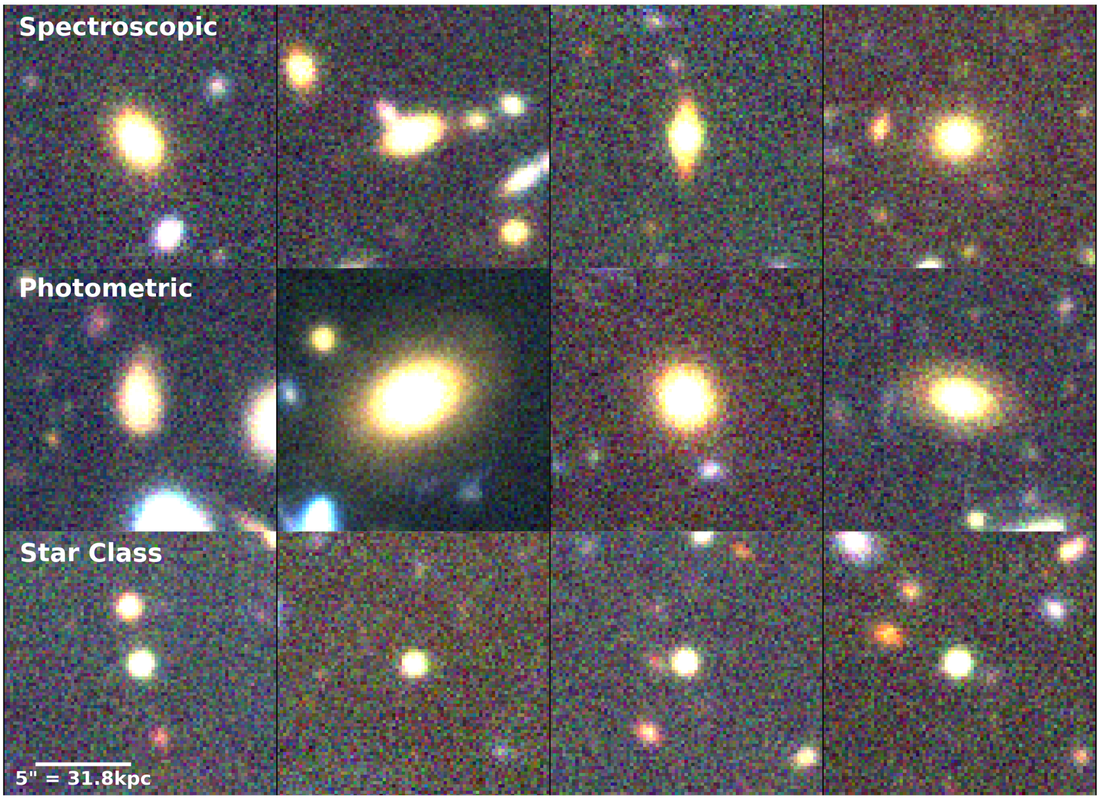

Figure 5.3: *RGB* image cutouts of spectroscopic (top row), photometric (middle row), and star class objects (bottom row). We create the image cutouts using g, r, and i band images from the PDR 3 photometric catalog of HSC-SSP. A scalebar in the bottom left of the figure shows the conversion from arcseconds to kpc, assuming the cluster redshift of $z = 0.53$.

5.4 r band $k-$correction for Cluster Member Candidates

All objects in our sample, both spectroscopic and photometric, have redshifts $z > 0.0$. As a result of nonzero redshifts, the light we observe in the $r-$band is intrinsically emitted at a shorter wavelength (e.g. Hogg et al. 2002). We correct for this by using the $k-$correction value. In order to calculate the R band absolute magnitude of our photometric cluster member candidates, each object needs to have a $k-$correction value (Oke & Sandage 1968; Hogg et al. 2002; Blanton & Roweis 2007; Chilingarian et al. 2010).

The $k-$correction is used to convert the observed apparent magnitude (m_R) in photometric bandpass (R) to the intrinsic absolute magnitude (M_Q) in the emitted-frame bandpass (Q) and is defined by the equation

$$m_R = M_Q + DM(z) + k_{QR}(z) - 5\log_{10} h \ , \tag{5.5}$$

where h is the dimensionless Hubble parameter and DM is the distance modulus. DM is given by

$$DM = 5log_{10}\frac{D_L}{10pc} \ , \tag{5.6}$$

where D_L is the luminosity distance, which is dependent on redshift. The $k-$correction k_{QR}(z) is given by

$$k_{QR} = -2.5log_{10}\left[[1+z] \frac{\int \frac{d\nu_0}{\nu_0} f_\nu(\nu_0) R(\nu_0) \int \frac{d\nu_e}{\nu_e} g^Q_{\nu_e}(\nu_e) Q(\nu_e)}{\int \frac{d\nu_0}{\nu_0} g^R_{\nu_0}(\nu_0) R(\nu_0) \int \frac{d\nu_e}{\nu_e} f_\nu(\frac{\nu_e}{1+z}) Q(\nu_e)} \right] \ , \tag{5.7}$$

where ν_o is the observed frequency, ν_e is the emitted frequency, $f_\nu(\nu_o)$ is the source flux density, $R(\nu_o)$ and $Q(\nu_e)$ are the bandpass functions at each frequency, $g^Q_{\nu_e}$, and $g^R_{\nu_o}$ are standard sources (standard stars) in each bandpass.

To calculate the $k-$correction, $k_{QR}(z)$, for a given object, we must know all the variables in Equation 5.7. For our spectroscopic members, we know the values of all variables in Equation 5.7. $k-$corrections for our spectroscopic objects are calculated by (Sohn et al. 2019). However, for the photometric cluster member candidates, we do not have a precise value for the redshift z of each object. The large photometric redshift uncertainty translates into large uncertainty on the $k-$correction for photometric cluster member candidates. This renders us unable to calculate $k-$correction values for our photometric cluster member candidates

To assign $k-$corrections to photometric cluster member candidates, we create a 4D KDE based on spectroscopic members. The dimensions of our KDE are $g-r$, $r-i$, r band apparent magnitude, and r band $k-$correction. To find the optimal bandwidth we do a grid search cross validation across the parameter space (see Section 5.1)

We take a single sample from the KDE and omit samples that are beyond the maximum and minimum spectroscopic value for each dimension. This is necessary because the KDE creates a continuous distribution which extends beyond the observed spectroscopic values of each dimension. With KDE sampled points we calculate the Euclidean distance (d)

$$d = \sqrt{(x_2 - x_1)^2 + (y_2 - y_1)^2 + (z_2 - z_1)^2}\ , \tag{5.8}$$

in the space of $g-r$, $r-i$, r band apparent magnitude for photometric cluster member candidate (x_2, y_2, z_2) and KDE sample points (x_1, y_1, z_1), respectively. We assign the r band $k-$correction of the nearest KDE sample point to the photometric cluster member candidate. Figure 5.4 shows spectroscopic (squares) and photometric cluster member candidates (circles) on the color-color diagram. The points are colored by the r band $k-$correction value. For spectroscopic members, the $k-$correction shown is the calculated $k-$correction. The $k-$corrections for spectroscopic members, and thus photometric cluster member candidates, ranges from -0.81 to 0.31.

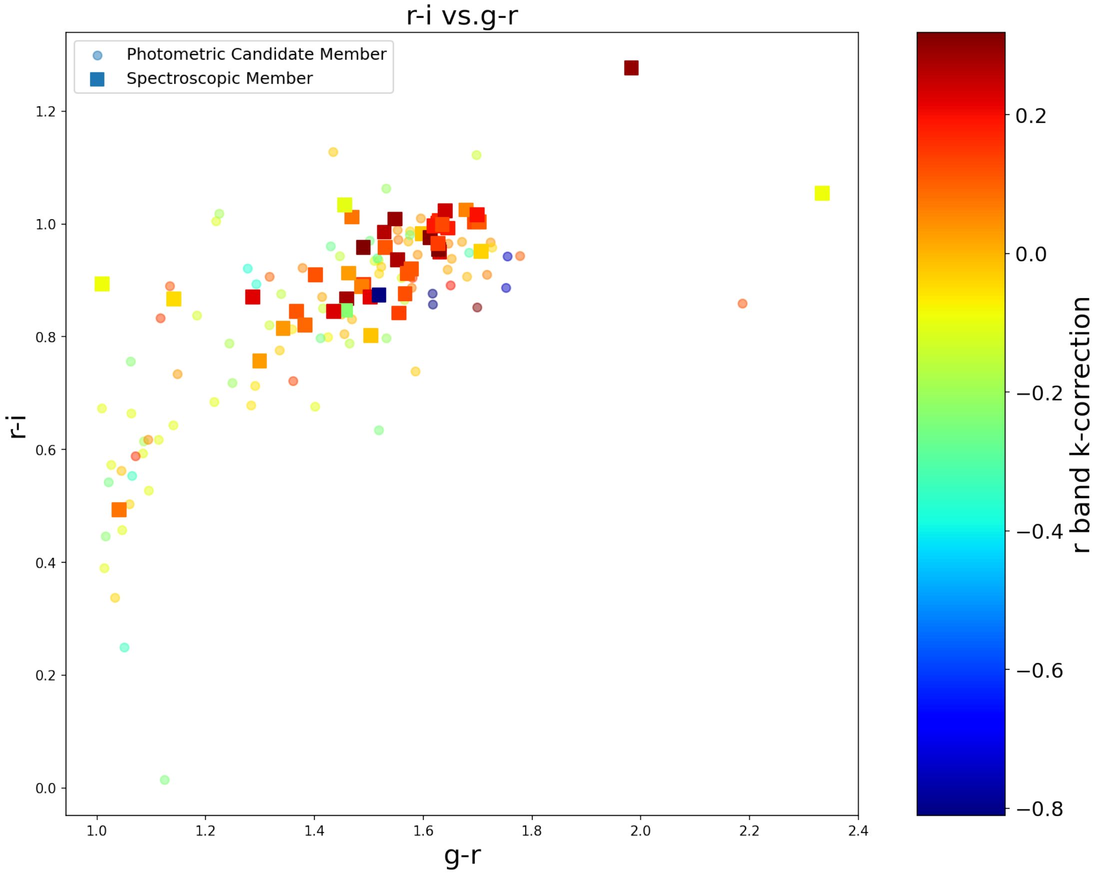

Figure 5.4: $r - i$ vs. $g - r$ color-color diagram showing both spectroscopic members (squares) and photometric cluster member candidates (circles). All points are colored by their r band $k-$correction value. Section 5.1 discusses KDE and Section 5.4 discusses how $k-$corrections are calculated for spectroscopic members and assigned to photometric cluster member candidates.

We perform bootstrap resampling to ensure that our small spectroscopic sample is not dominating the assignment of $k-$corrections to photometric cluster member candidates. We create 10 bootstrapped resamples of our spectroscopic data set. For each bootstrapped resample, we follow the aforementioned assignment of $k-$corrections to our photometric cluster member candidates. Each photometric cluster member candidate now has 10 r band $k-$correction values that have been assigned from bootstrapped spectroscopic samples. For each photometric cluster member candidate, we calculate the median r band $k-$correction. We compare the median $k-$correction value, obtained from bootstrapping, to the $k-$correction value obtained from the full spectroscopic sample. We find the difference to be $\approx$ 0.06. The variation in $k-$correction between the bootstrapped samples and the full spectroscopic sample is negligible and confirms that our small spectroscopic sample is not dominating the assignment of $k-$corrections to photometric cluster member candidates.

To illustrate how well the 4D KDE represents the distribution of individual dimensions of spectroscopic cluster members: *r - i*, *g - r*, r band apparent magnitude, and r band $k-$correction, we marginalize across each dimension of our 4D KDE from Figure 5.4 By marganilizing the 4D KDE, we can examine the 1D probability density function (PDF) of each dimension. In Figure 5.5, we show the histograms of spectroscopic members (left column) and samples from the 4D KDE (right column) for each dimension in the 4D KDE. In each row we also show the 1D PDF (blue curve) overplotted with both spectroscopic members and the 4D KDE sampled points. It is important to note that the 1D PDF shown in each row is the same for both spectroscopic and 4D KDE samples. Each row represents a different dimension used to create the 4D KDE, these dimensions are *r - i* (first row), *g - r* (second row), r band apparent mag (third row), and r band $k-$correction (fourth row).

To marginalize across one dimension of a KDE, we integrate the KDE over all dimensions except for the one being marginalized following the equation

$$P(x_k) = \int P(x_1, x_2, ..., x_{k-1}, x_{k+1}, ...x_n) dx_1 dx_2 dx_{k-1} dx_{k+1} dx_n. \tag{5.9}$$

In Equation 5.9, the marginalized dimension is x_k, and we integrate over all other dimensions in the KDE.

For each dimension in our 4D KDE, Equation 5.9 changes to:

$$P(x) = \left\{ \begin{array}{ll} \int P(x_{r-i}, x_r, x_{k_{QR}(z)}) dx_{r-i} dx_r dx_{k_{QR}(z)}, & \text{to find} P(x_{g-r}) \\ \int P(x_{g-r}, x_r, x_{k_{QR}(z)}) dx_{g-r} dx_r dx_{k_{QR}(z)} & \text{to find} P(x_{r-i}) \\ \int P(x_{g-r}, x_{r-i}, x_{k_{QR}(z)}) dx_{g-r} dx_{r-i} dx_{k_{QR}(z)}, & \text{to find} P(x_r) \\ \int P(x_{g-r}, x_{r-i}, x_r) dx_{g-r} dx_{r-i} dx_r, & \text{to find} P(x_{k_{QR}(z)}) \end{array} \right\} . \quad (5.10)$$

The result of Equations 5.10 is a 1D PDF representing each dimension of the KDE. We do this to check that each dimension of the 4D KDE we create to assign r band $k-$corrections follows the true distribution of spectroscopic members.

With the r band $k-$corrections, we calculate the R band absolute magnitude for both spectroscopic members and photometric cluster member candidates. We calculate R band absolute magnitudes using Equation 5.5. When calculating absolute magnitudes, we also account for extinction due to dust. Each spectroscopic cluster member has a dust extinction value. For photometric cluster member candidates, we use the mean spectroscopic dust extinction of 0.02. We subtract the extinction due to dust from the apparent magnitude. We use the R band absolute magnitude to assign $D_n 4000$ values to photometric cluster member candidates (Section 5.6).

5.5 Determining R_{cl}/R_{200} for Spectroscopic Members and Photometric Cluster Member Candidates

To determine how far spectroscopic members and photometric cluster member candidates are from the cluster center, we calculate the clustercentric distance R_{cl} (Section 1.2.3) in units of R_{200}. We use R_{cl}/R_{200} as it allows us to examine how the environment affects individual cluster members. For photometric cluster member candidates, we assume they are all at the redshift of cluster center ($z = 0.53$). This also implies that all photometric cluster member candidates have

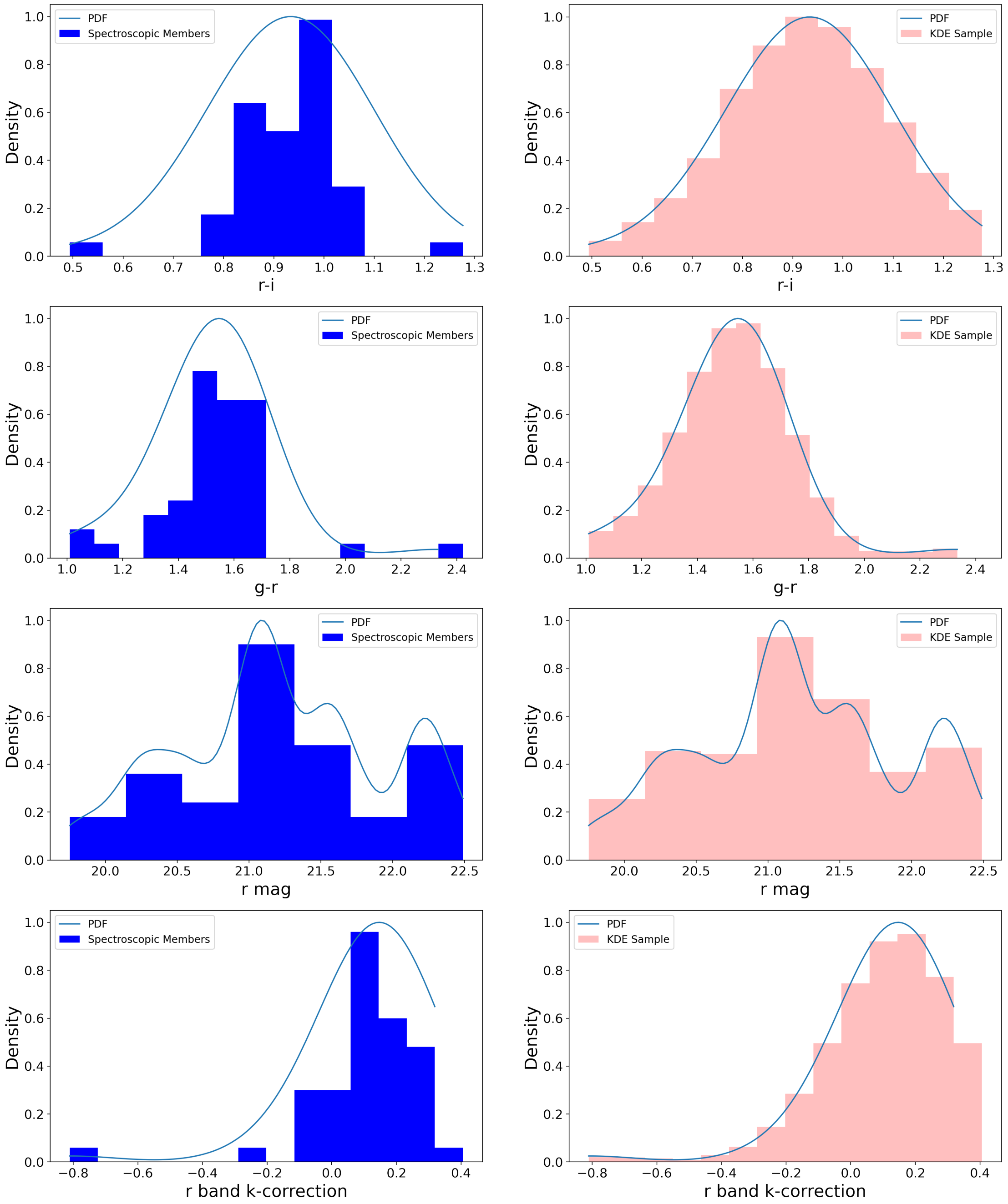

Figure 5.5: Histograms of spectroscopic members (left column) and 4D KDE samples (right column) over plotted with 1D probability density function (PDF). Each row corresponds to a dimension in the 4D KDE used to assign $k-$corrections from Figure 5.4. We can see that the 1D PDFs, we obtain through marginalization, accurately represent the spectroscopic data as well as the samples from the 4D KDE.

the same angular diameter distance. However, for spectroscopic members, we have accurate redshifts and use each individual member's redshift to find the angular diameter distance. If we use the cluster center redshift to calculate R_{cl} for all objects, there would be a negligible ($< 2\%$)

difference in our obtained values.

The angular diameter distance of an object is defined as

$$D_A = \frac{D_M}{1+z}, \tag{5.11}$$

where D_M is the transverse comoving distance and is equal to

$$D_M = D_C \ , \tag{5.12}$$

where D_C is the line-of-sight comoving distance (Hogg 1999).

We use `CosmoCalc` to calculate the angular diameter distance of spectroscopic and photometric cluster member candidates. We then calculate the median R.A. and Dec. of our spectroscopic samples and define that to be the cluster center. Using the median R.A and Dec., we find the distance from the cluster center of cluster members and member candidates using

$$D = \sqrt{((x_2 - x_1) * (cos(y_1))^2 + (y_2 - y_1)^2} \ , \tag{5.13}$$

where x_2 and y_2 are the R.A. and Dec. coordinates of our objects and x_1 and y_1 are the cluster center R.A. and Dec. To find the cluster centric radius (R_{cl}) for both spectroscopic members and photometric cluster member candidates, we multiply the angular diameter distance (Equation 5.11) by the angular distance from the cluster center (Equation 5.13). We then normalize R_{cl} by the R_{200} of the cluster (Chapter 2).

Figure 5.6 shows the distribution of R_{cl}/R_{200} for all spectroscopic members (blue) and photometric cluster member candidates (red). The clustercentric distances for spectroscopic members extend to approximately 5 R_{cl}/R_{200}, whereas the clustercentric distances for photometric cluster member candidates are much more extended. To be able to characterize the photometric cluster member candidates, we only include candidates that are within the same clustercentric radius as spectroscopic members. We do so to ensure that the D_n4000 values we assign are from similiar spectroscopic members. The maximum R_{cl}/R_{200} of spectroscopic members is shown as the black dashed line in Figure 5.6. All photometric cluster member candidates beyond this cut are removed from our analysis. We find 56 photometric cluster member candidates within 5 R_{cl}/R_{200} of our cluster.

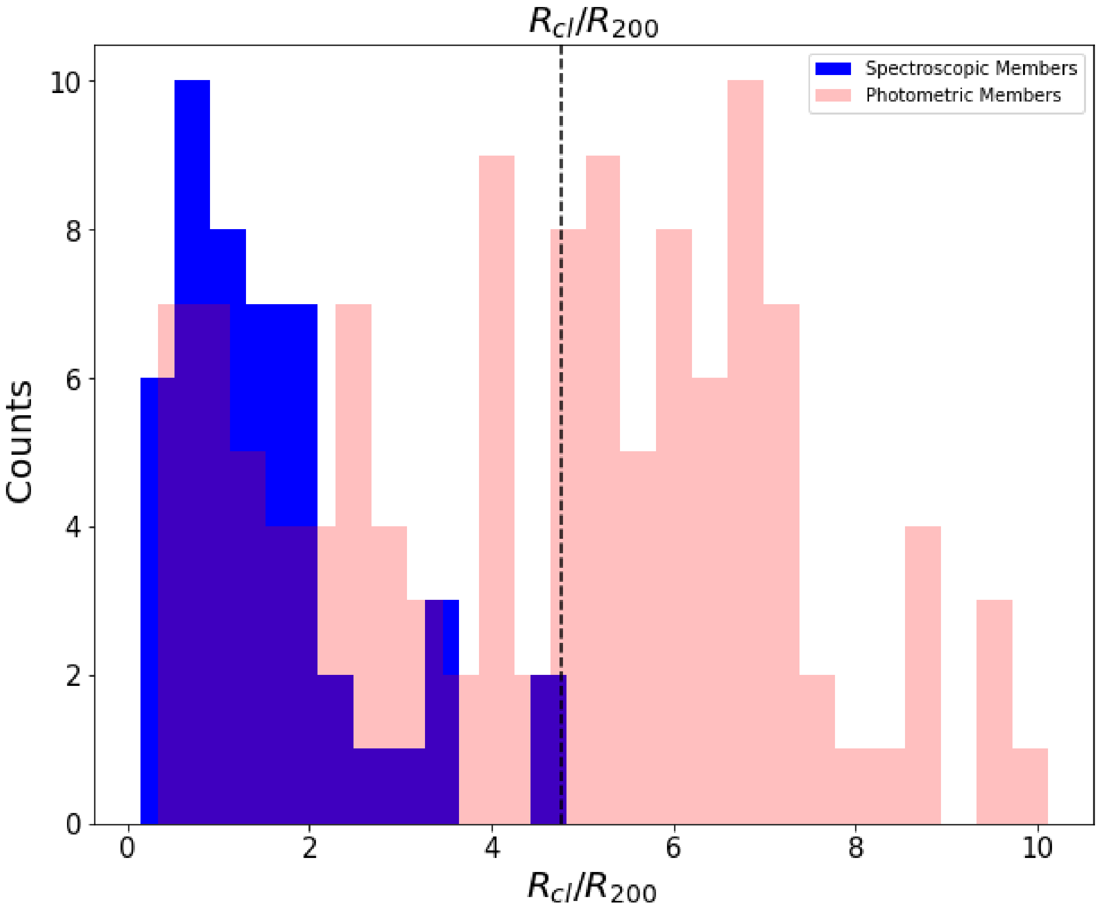

Figure 5.6: Histogram of clustercentric radii (R_{cl} Mpc) normalized by R_{200} (0.56 ± 0.03 Mpc) for spectroscopic (blue) and photometric cluster member candidates (red). The black dashed line indicates the maximum R_{cl}/R_{200} of spectroscopic members. We use the maximum R_{cl}/R_{200} of spectroscopic members as our selection limit for including photometric cluster member candidates.

5.6 Assigning D_n4000 Indices to Photometric Cluster Member Candidates

We include photometric cluster member candidates to make statistical corrections for the missing cluster members in calculating scaling relations for cluster galaxies (Section 6.2 and 6.4). To make these corrections we assign photometric cluster member candidates D_n4000 values based on their distance in R_{cl}/R_{200} to spectroscopic cluster members. To ensure that D_n4000 values are assigned to photometric cluster member candidates based on the properties of spectroscopic members with the most similar properties, we consider the distribution of spectroscopic members in R band absolute magnitudes.

The upper left panel of Figure 5.7 shows the distribution of R band absolute magnitudes for all spectroscopic members (blue) and photometric cluster member candidates (pink). We bin the spectroscopic members into three equal sized bins of R band absolute magnitude. Equal sized bins are used so that each KDE is created from a uniform number of points. The photometric cluster member candidates are then sorted into the three R band absolute magnitude bins. Some photometric cluster member candidates are outside the range of spectroscopic R band absolute magnitudes, shown as the shaded grey region in Figure 5.7. These photometric cluster member candidates are not included in our analysis as they do not have spectroscopic members with similar intrinsic luminosities. Our sample of photometric cluster member candidates now contains 51 galaxies.

We then create a 2D KDE based on the D_n4000 and R_{cl}/R_{200} of the spectroscopic members in each bin. The remaining three panels of Figure 5.7 are $-19.26 > M_R > -21.14$ (top right), $-21.24 > M_R > -21.61$ (bottom left), and $-21.61 > M_R - 22.8$ (bottom right). For each bin, we sample 1000 points from the KDE. Each sampled point has an associate R_{cl}/R_{200} and D_n4000 value. For the same bin, we then find the minimum difference between a sampled points R_{cl}/R_{200} and a photometric cluster member candidates R_{cl}/R_{200}. The photometric cluster member candidate that is closest to a sampled point, in terms of R_{cl}/R_{200}, is then assigned the sampled point's D_n4000. This process is repeated 1000 times in each bin so that each photometric cluster member candidate has 1000 D_n4000 values. The D_n4000 value for each spectroscopic member is the calculated D_n4000 (Section 4.2), which remains constant throughout the 1000 iterations. By doing this we have created a sample of 1000 partially independent mock galaxy clusters.

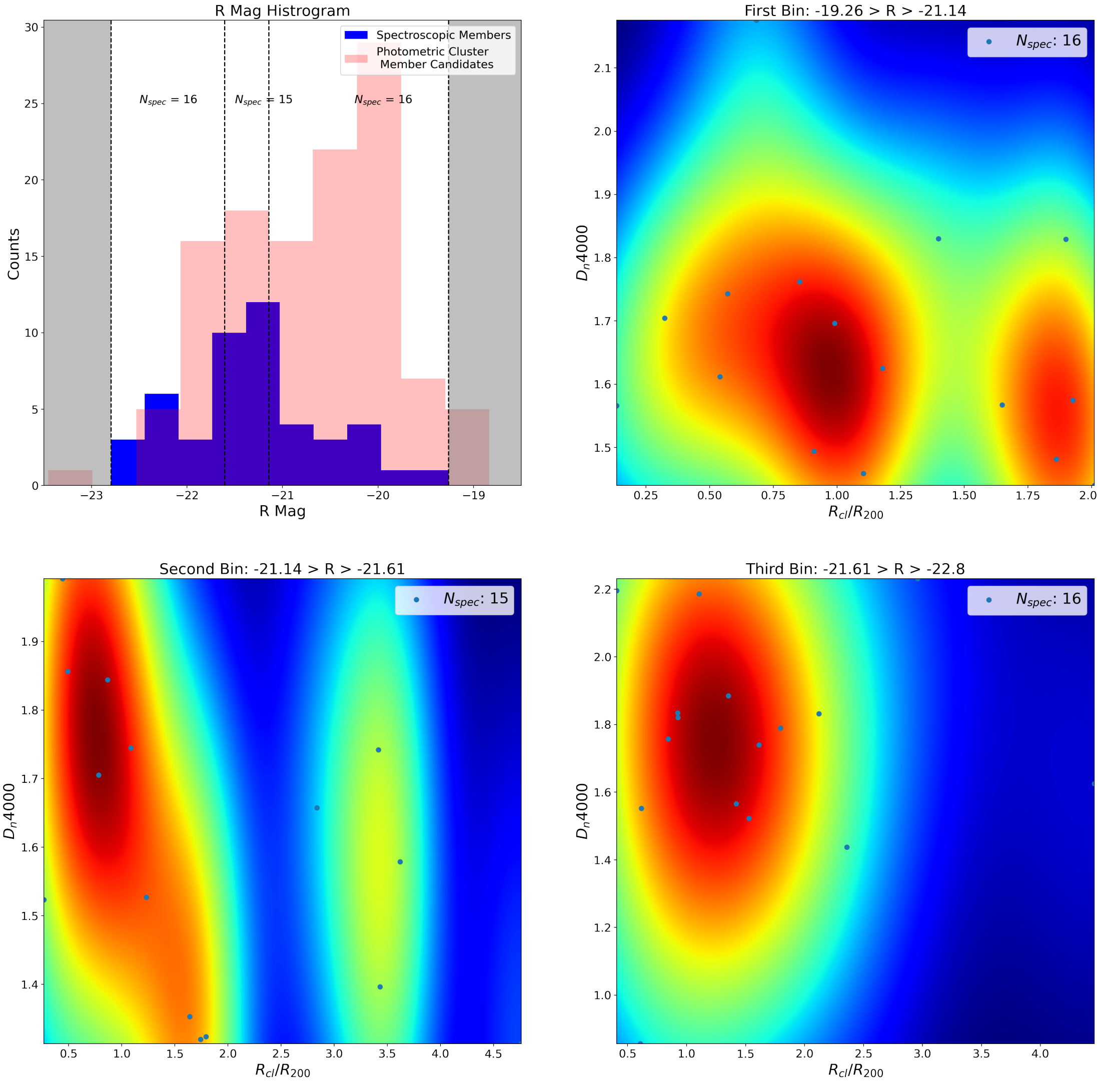

Figure 5.7: Histogram showing R band absolute magnitudes (upper left) of spectroscopic members (blue) and photometric cluster member candidates (pink). The grey shaded areas are regions where there are no spectroscopic members. Photometric cluster member candidates in the grey shaded regions are not included in our analysis. The bin boundaries are indicated as black dashed lines, and the number of spectroscopic members in each bin is shown as N_{spec}. The following three panels show the 2D surface based on the KDE for the distribution of spectroscopic cluster members in the parameter space of D_n4000 and R_{cl}/R_{200}. Our three bins are as follows: $-19.26 > M_R > -21.14$ (top right), $-21.24 > M_R > -21.61$ (bottom left), and $-21.61 > M_R - 22.8$ (bottom right) .

Chapter 6

Results and Discussion

As we discuss in Section 1.3, individual galaxy properties such as morphology, star formation, and gas content can be impacted based on the environment in which a galaxy resides. The cluster environment offers the most extreme example of environmental effects on individual galaxies. Galaxies nearby and within the cluster environment can experience harassment (Moore et al. 1996; Bialas et al. 2015), minor mergers (Naab et al. 2009; Planelles & Quilis 2009; Chen et al. 2019), ram-pressure stripping (Gunn & Gott 1972; Abadi et al. 1999; Sohn et al. 2019), strangulation (Larson et al. 1980; Balogh et al. 2000; Kawata & Mulchaey 2008), and tidal interactions (Eneev et al. 1973; Byrd & Valtonen 1990). These quenching mechanisms alter the relation between D_n4000 and R_{cl}/R_{200} (Section 6.1) and also Size and Stellar Mass (Section 6.2) for quiescent galaxies (Section 1.2.1) in the cluster environment.

6.1 Cluster Galaxy D_n4000-Clustercentric Distance Relation

All of the above processes can alter the star formation rate, and thus the average stellar population age of a galaxy. Changes to a galaxy's stellar population age are directly measurable through the D_n4000 index. We aim to investigate how the D_n4000 index (Section 4.2) of a galaxy changes as a function of R_{cl}/R_{200} (Section 5.5).

It has been well established that in local universe clusters ($z < 0.2$) there is a decrease in the star formation rate in galaxies as they approach the cluster center (Gómez et al. 2003; Smith et al. 2006; Mahajan et al. 2012; Wetzel et al. 2013; Smith et al. 2019). As the star formation rate of a galaxy decreases, we expect to see the D_n4000 index increase. This is a direct result of the evolution of the stellar population within a galaxy. It has been shown that galaxies that infall earlier into the cluster environment, are more likely to be virialized and are quenched earlier, leading to an increase in the galaxy's D_n4000 (Yoon et al. 2017; Einasto et al. 2018; Smith et al. 2019). Therefore, in the local universe, galaxies within the cluster environment have been found to have a trend of increasing D_n4000 with decreasing clustercentric radius.

Previous studies investigate the D_n4000-clustercentric radius relation at higher redshifts $z > 0.2$ (e.g. Muzzin et al. 2012; Kim et al. 2022; Paulino-Afonso et al. 2020; Mahajan & Raychaudhury 2009). These works show that the trend of the D_n4000-clustercentric radius relation is not as strong at higher redshifts $z > 0.2$. This indicates that galaxy clusters are still assembling and have not had sufficient time to fully quench galaxies near the cluster center.

We investigate $D_n4000 - R_{cl}/R_{200}$ to determine if the trend found by previous works holds true for our cluster at redshift $z = 0.53$. In Section 2, we discuss that our cluster is a potentially merging cluster. By analyzing $D_n4000 - R_{cl}/R_{200}$, we can add to previous studies to better understand the environmental effect of galaxy clusters on individual galaxy's stellar population age at higher redshifts. We use both spectroscopic members and photometric cluster member candidates to study $D_n4000 - R_{cl}/R_{200}$ for our cluster.

We assign each photometric cluster member candidate a D_n4000 value based on its proximity to points sampled from a KDE (Section 5.1). The KDE we use here is based on the positions of spectroscopic members in the parameter space of D_n4000 and R_{cl}/R_{200} (Figure 5.7). We iterate the process of assigning D_n4000 to photometric cluster member candidates 1000 times.

For spectroscopic cluster members we use the calculated D_n4000 (Section 4.2) for each iteration. By performing this iterative assignment, we are simulating 1000 mock galaxy clusters. Due to our selection of photometric cluster member candidates based on the faintest apparent r band magnitude of spectroscopic cluster members, each simulated sample represents a flux limited sample of cluster members.

Previous works have shown that linear fits can accurately capture the relation between D_n4000 and cluster radius (Mahajan & Raychaudhury 2009; Muzzin et al. 2012; Paulino-Afonso et al. 2020; Kim et al. 2022). For each simulated galaxy cluster, we perform a linear fit following the equation

$$D_n4000 = \alpha \left(\frac{R_{cl}}{R_{200}} \right) + A \, , \tag{6.1}$$

where α is the slope and A is the zero point corresponding to the D_n4000 at the cluster center. We use the `Scipy` (Virtanen et al. 2020) package `stats` for our fitting procedure. From our fitting procedure, we obtain the best fit slope and zeropoint parameters for all 1000 relations of $D_n4000 - R_{cl}/R_{200}$.

We show the 2D distribution of slopes and zero points in the central panel of Figure 6.1. We fit the distribution of slopes and zero points as a bivariate Gaussian distribution. The parameters of this fit are the principal axis (σ_1 and σ_2), the rotation of the ellipse (α), the standard deviation of the slope and zeropoint (σ_x and σ_y), and the correlation coefficient (σ_{xy}). We use the parameters of the bivariate Gaussian distribution to create 1D Gaussian distributions of the slope and zeropoint. The white ellipses in the center panel show the 1, 2, and 3 σ confidence regions. The top panel of Figure 6.1 shows the 1D histogram of slopes. We also show the 1D Gaussian (red) that we create using `Scipy stats` package with the parameters we obtain from the bivariate Gaussian fit. To show that the 1D Gaussian is an accurate representation of the distribution of

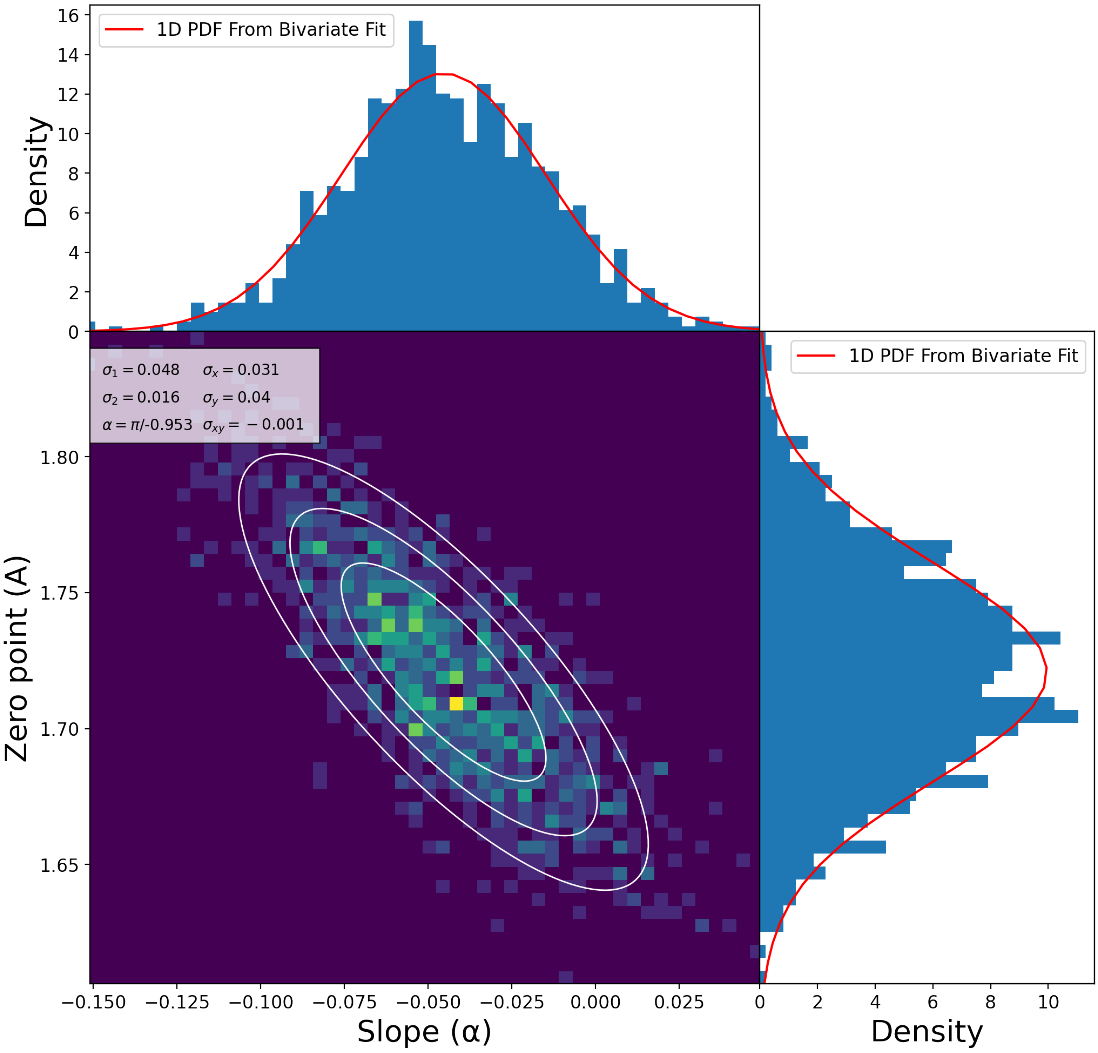

Figure 6.1: Center panel: 2D distribution of slopes (α) and zero points (A) of the D_n4000 vs. R_{cl}/R_{200} relation (Equation 6.2) based on 1000 simulated samples with spectroscopic and additional photometric members. The white ellipses trace the 1, 2, and 3 σ confidence intervals from the 2D Gaussian that best represents our observed distribution. Side panels: 1D distribution of slopes (top) and zero points (right). The blue histograms are the slopes/zero points from all 1000 relations and the red curve is the PDF created from the observed data. This shows we can model the distribution of both slopes and zero points as a Gaussain to find the median slope and zero point.

slopes, we show it against the histogram of slopes (blue). The right panel is the same as the top panel except it is for the distribution of zero points. Both side panels of Figure 6.1 show that we are able to represent the distributions of slopes and zeropoints as a 1D Gaussian.

From the 1D Gaussian fits, we find the median slope and zero point from all 1000 $D_n4000 - R_{cl}/R_{200}$ relations. The median relation of $D_n4000 - R_{cl}/R_{200}$ for our cluster is

$$D_n4000 = (-0.045 \pm 0.035)\left(\frac{R_{cl}}{R_{200}}\right) + (1.721 \pm 0.040)\ . \tag{6.2}$$

Uncertainties on the slope and zero point values are estimated from the standard deviation of the fitted 1D Gaussians.

Figure 6.2 shows the median relation between $D_n4000 - R_{cl}/R_{200}$ for spectroscopic members (red) and photometric cluster member candidates (blue) in our cluster over a random iteration of photometric cluster member candidates. The grey lines show all 1000 relations of $D_n4000 - R_{cl}/R_{200}$. We show these to demonstrate that the median relation is an accurate representation of the data. Within the uncertainties of our measurement, we find the trend of D_n4000 to be flat across all values of R_{cl}/R_{200}. We also examine the relation of $D_n4000 - R_{cl}/R_{200}$ with only spectroscopic members and find no change in our results.

To better understand this relation we would need to have a more complete spectroscopic member catalog. We discuss potential future work in Section 7.1. However, with our current results, we find a flat trend, within errors, of $D_n4000 - R_{cl}/R_{200}$ for our galaxy cluster. This indicates that galaxies at both small and large clustercentric distances have similarly aged stellar populations. A D_n4000 greater than 1.5 indicates that the stellar population is older than 1 Gyr (see Figure 4.3 for relation between stellar population age and D_n4000). As a result of the constant trend of $D_n4000 - R_{cl}/R_{200}$ with a zeropoint of 1.721 ± 0.040, we infer that the median galaxy stellar population age of our cluster is $\approx$ 5 Gyr, depending on assumed stellar metallicity (Figure 4.3).

Although the median trend is flat, we do observe a significant scatter in the D_n4000 of galaxies at all clustercentric distances. This indicates that there is a mixture of galaxies with old (> 1 Gyr) stellar populations and galaxies with young (< 1 Gyr) stellar populations at all clustercentric distances. However, this mixture of galaxy stellar population ages is slightly skewed

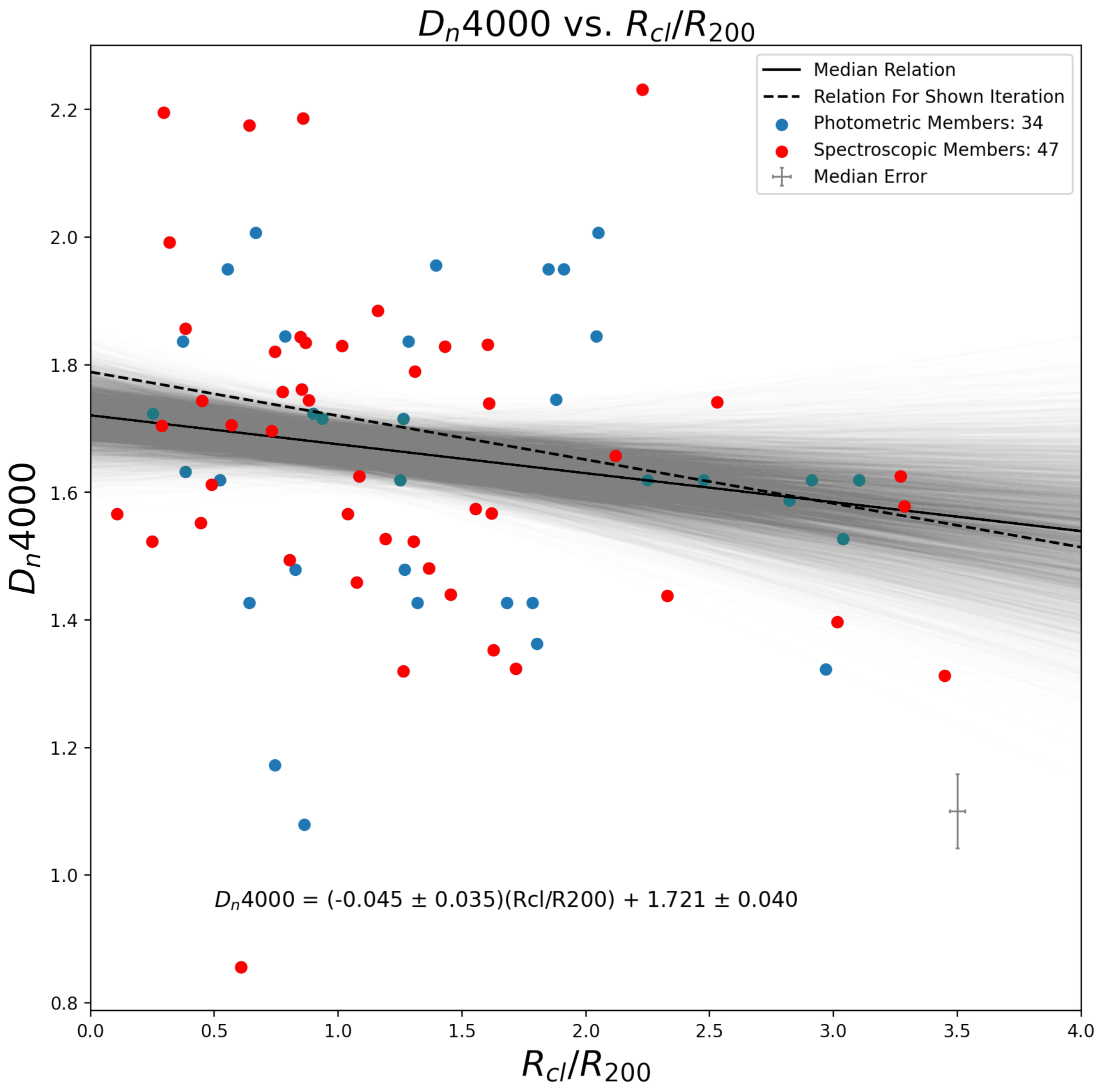

Figure 6.2: D_n4000 as a function of clustercentric radius (R_{cl}) normalized by R_{200}. The red points are spectroscopic members and the blue points are photometric cluster member candidates with D_n4000 values based on a single draw from the 1000 relations of D_n4000 vs. R_{cl}/R_{200}. The solid black line is the median relation from Equation 6.2. The 1000 grey lines represent the 1000 relations of D_n4000 vs. R_{cl}/R_{200} for spectroscopic and photometric cluster member candidates. The black dashed line is the relation for the shown colored points.

towards older populations as evident by our median zeropoint being 1.721 ± 0.040.

As we discuss in Chapter 2, this cluster has two BCGs with distinct groupings of galaxies surrounding each BCG. Our cluster was chosen for spectroscopic follow up observations as it is a potentially merging cluster (Sohn et al. 2021a). We now find similarly aged stellar populations at large and small clustercentric distances as well as a large scatter in the D_n4000 of cluster members at large and small clustercentric distances. Our results act as an independent suggestion that this cluster is currently undergoing a merger.

We directly compare our results to two studies that examine D_n4000 vs. clustercentric distance. We compare to Muzzin et al. (2012), who study the D_n4000 of quiescent galaxies as a function of environment. Their work uses a sample with multiple galaxy clusters over a redshift range of $0.85 < z < 1.20$. Muzzin et al. (2012) find a nearly flat trend of $D_n4000 - R_{cl}/R_{200}$ for quiescent galaxies with mass $\log_{10}(M_*/M_\odot) > 10.0$. The majority of our photometric cluster member candidates and spectroscopic members are at similar masses. Muzzin et al. (2012) reports an average zeropoint of 1.68 at a radius of 0.1 Mpc for objects with $\log_{10}(M_*/M_\odot) > 10.0$. This is further indication that clusters at higher redshifts $z > 0.2$ are still forming and have a mixture of both star forming and quenched galaxies across all clustercentric distances.

We also compare our results to Kim et al. (2022). However, these authors do not strictly look at D_n4000-Clustercentric distance. Instead, Kim et al. (2022) study D_n4000 vs. infall time, which is defined as the $\log(R_{cl}/R_{500}) \times$ the line of sight peculiar velocity. In our comparison we use the infall time as a proxy for cluster radius. The sample in Kim et al. (2022) includes 105 clusters spanning a redshift range of 0.26 < z < 1.13 which is then subdivided into low redshift 0.26 < z < 0.53, high redshift 0.53 < z < 1.13, and the total redshift range. The authors find a nearly flat trend in D_n4000 vs infall time across all redshift bins. The low z bin has a marginally steeper slope -0.093 $\pm$ 0.020 compared to the high z bin slope -0.078 $\pm$ 0.025 and the total z bin slope -0.096 $\pm$ 0.016. We find our slope to be within 3σ of all redshift bin slopes presented in Kim et al. (2022). However, while our slope is within 3σ of Kim et al. (2022), we do observe that our slope, within errors, is smaller than the high z bin. This may be further indication that our cluster is currently merging as the average stellar population age of our cluster members is flat compared to other clusters at similar redshifts.

Comparison of the zeropoint to Kim et al. (2022) is not as straightforward as the slope comparison. As a result of analyzing the infall time, the zeropoints reported by Kim et al. (2022) do not represent the cluster center. We extrapolated the reported zeropoints to obtain values that represent the cluster center. The low z bin has the largest zeropoint of 1.76 ± 0.02, followed by the total z bin 1.71 ± 0.01, and the high z bin 1.63 ± 0.02. Regardless of which bin we use to compare our results, we find our slope value to be within 3σ of those reported by Kim et al. (2022). However, we find that our zeropoint, within errors, falls between the low z bin and the high z bin. With better statistics, our results may act as further confirmation that the average stellar population age within the cluster core increases with redshift.

We find for our galaxy cluster that there is a flat trend of D_n4000 with decreasing clustercentric radius. Our results, in combination with other works, contribute to tracing the trend of galaxy cluster stellar population age with clustercentric distance with redshift. A flat trend of $D_n4000 - R_{cl}/R_{200}$ indicates that galaxies near the center of the cluster and galaxies at the outskirts of the cluster have similar stellar population ages. This is in disagreement with what has been found in the cluster environment in the local Universe. At low redshifts $z < 0.2$, it has been shown that the stellar population age of a galaxy increases as the galaxy approaches the cluster center (Gómez et al. 2003; Smith et al. 2006; Upadhyay et al. 2021). We hypothesize that the flat trend in $D_n4000 - R_{cl}/R_{200}$ that we observe is a direct result that shows our cluster is currently undergoing a merger. This result offers an independent suggestion that this cluster is a merging cluster.

6.2 Galaxy Cluster Size-Stellar Mass Relation

The same processes we discuss in the introduction of this chapter can affect the size of galaxies within a cluster. Observations have shown that there is an evolution in the size of quiescent galaxies from high redshfit $z > 1$ to the local Universe (e.g. Mowla et al. 2019a; Williams et al. 2010; van der Wel et al. 2014; Shen et al. 2003a; Huertas-Company et al. 2013; Rettura et al. 2010; Maltby et al. 2010). Under the hierarchical model of galaxy formation, galaxy clusters should be regions where we observe accelerated evolution of galaxies (Dressler 1980; Cooper et al. 2012; Jørgensen & Chiboucas 2013; Delaye et al. 2014; Morishita et al. 2017; Chan et al. 2018). This makes galaxy clusters excellent laboratories where we can explore how the environment affects individual galaxy's sizes.

However, there are mixed results as to the true dependence of galaxy size on their environment. Some results show that galaxies within clusters have smaller sizes than their counterparts in the field (e.g. Maltby et al. 2010; Rettura et al. 2010; Raichoor et al. 2012). Others find that galaxies in clusters are larger in size than those in the field (e.g. Papovich et al. 2012).

To study the size-stellar mass relation of our cluster, we use our sample of spectroscopic cluster members and continue using the same set of photometric cluster member candidates as in Section 6.1. We do not assign new D_n4000 values, all photometric cluster member candidates have the same 1000 D_n4000 values as in Section 6.1. However, for the size-stellar mass relation, we select only spectroscopic members and photometric cluster member candidates that have D_n4000 > 1.5. We do so to select the quiescent galaxies within our galaxy cluster (Damjanov et al. 2023). This means we have a constant number of spectroscopic members as their D_n4000 does not change over each iteration. However, the number of photometric cluster member candidates is not constant as the assigned D_n4000 value changes with each iteration.

We examine 1000 size-stellar mass relations containing both spectroscopic members and photometric cluster member candidates. For each iteration, we fit the size-stellar mass relation using a linear equation following the form

$$\log_{10}\left(\frac{R_{eff}}{1kpc}\right) = \beta \log_{10}\left(\frac{M_*}{10^{11}M_\odot}\right) + B \ , \tag{6.3}$$

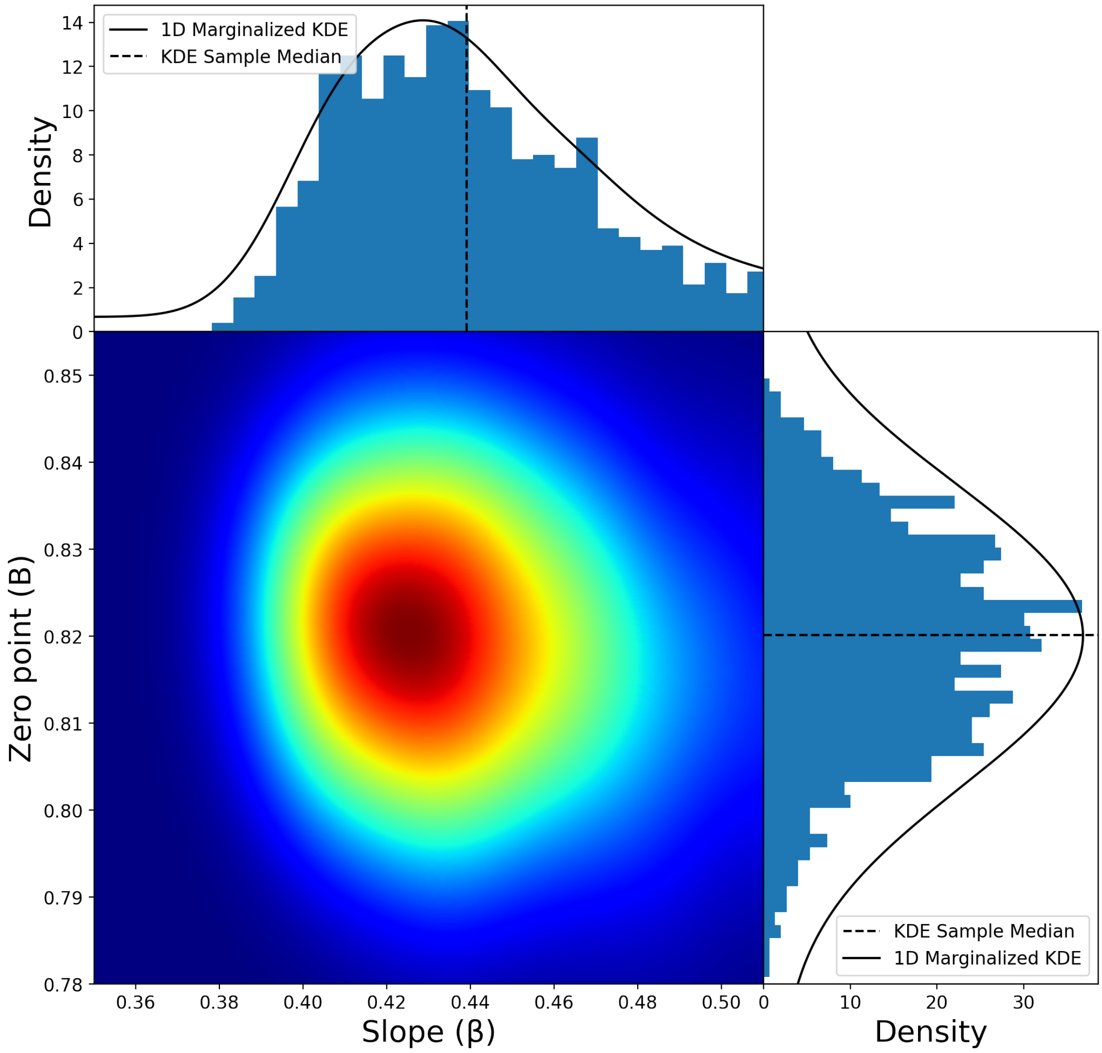

Figure 6.3: 2D surface (center panel) based on the KDE in the parameter space of zeropoint (B) and slope (β) obtained from 1000 size-stellar mass relations. We find the distribution of slopes and zeropoints to be non Gaussian and thus use a KDE to model it. We show the 1D histogram of slopes (top panel) and zeropoints (right panel) along with their respective 1D marginalized PDF and the KDE sample median. We use this KDE to find the median size- stellar mass relation parameters and find them to be β = 0.439 and B = 0.819.

where β is the slope and B is the zero point which corresponds to the size of a galaxy at a stellar mass of $\log_{10}(M_*/M_\odot) = 11.0$. From each fit we obtain a slope and zero point value. In total, we obtain 1000 best fit slope and zeropoint parameters that characterize 1000 size-stellar mass relations.

The distribution of size-stellar mass slopes and zeropoints for our full sample of spectroscopic members and photometric cluster member candidates is shown in Figure 6.3. We find that the distribution of slopes and zeropoints is non Gaussian. Therefore we cannot use a bivariate normal distribution to model the distribution of slopes and zeropoints as we do in Section 6.1. Instead, to model the slopes and zero points from our 1000 size-stellar mass relations, we use a 2D KDE.

The KDE is created in the parameter space of slopes and zeropoints following the methods discussed in Section 5.1. The 2D surface based on the KDE is shown in the center panel of Figure 6.3. We marginalize each dimension of the KDE and show the 1D PDF against the 1D histogram of slopes and zeropoints in the top and right panel, respectively. The distribution of slopes is a skewed Gaussian that extends further to larger slope values than what is shown. We truncate the skewed Gaussians to show the main body of the distribution. We then obtain 1000 samples from the 2D KDE and find the median slope and zeropoint which is shown as the black dashed line in Figure 6.3. We define the median of the KDE samples to be the parameters that best describe our 1000 size-stellar mass relations.

We find that for the spectroscopic members and photometric member candidates of our cluster with $(g-r) > 1.0$, $D_n4000 > 1.5$, over a mass range of $9.4 \leq \log_{10}(M_*/M_\odot) \leq 12.1$ exhibit a linear size-stellar mass relation

$$\log_{10}\left(\frac{R_{eff}}{1kpc}\right) = (0.426 \pm 0.036)\log_{10}\left(\frac{M_*}{10^{11}M_\odot}\right) + (0.827 \pm 0.015)\ . \tag{6.4}$$

The left panel of Figure 6.4 shows the size-stellar mass relation (black line) from Equation 6.4 alongside spectroscopic members (squares) and photometric cluster member candidates (circles). The grey lines in the left panel of Figure 6.4 are the 1000 samples from the 2D KDE of slopes and zero points. The size-stellar mass relation is shown plotted against a single randomly selected iteration of photometric cluster member candidates and spectroscopic members. All point are colored by their calculated D_n4000 (spectroscopic members) or their assigned

D_n4000 (photometric cluster member candidates). For our full sample of spectroscopic members and photometric cluster member candidates with $(g-r) > 1.0$ and $D_n4000 > 1.5$, we find that galaxies at a fixed stellar mass of $\log_{10}(M_*/M_\odot) = 11.0$ have an average size of 6.71 ± 1.04 kpc. We do not compare this result to other works as it covers a large mass range and does not accurately represent the known pivot in the size-stellar stellar mass relation.

In previous works it has been shown that there is a pivot stellar mass where the slope of the size-stellar mass relation changes for quiescent galaxies (Shen et al. 2003b; van der Wel et al. 2014; Kawinwanichakij et al. 2021; Mowla et al. 2019a; George 2020). The pivot mass for $z \approx 0.50$ is $\log_{10}(M_*/M_\odot) \approx 10.5$ (George 2020). We now select only photometric cluster member candidates and spectroscopic members with $(g-r) > 1.0$, $D_n4000 > 1.5$, and $\log_{10}(M_*/M_\odot) > 10.5$. We follow the same fitting procedure as discussed above and find the size-stellar mass relation to be

$$\log_{10}\left(\frac{R_{eff}}{1kpc}\right) = (0.550 \pm 0.022)\log_{10}\left(\frac{M_*}{10^{11}M_\odot}\right) + (0.818 \pm 0.016)\ . \tag{6.5}$$

The middle panel of Figure 6.4 shows the size-stellar mass relation for objects that have $\log_{10}(M_*/M_\odot) > 10.5$ (Equation 6.5). Additionally, we show a single randomly selected iteration of spectroscopic members and photometric cluster member candidates that have $\log_{10}(M_*/M_\odot) > 10.5$. We see the slope of our relation steepen when compared to the left panel. However, the zeropoint remains essentially unchanged. For our sample of spectroscopic members and photometric cluster member candidates with $(g-r) > 1.0$, $D_n4000 > 1.5$, and $\log_{10}(M_*/M_\odot) > 10.5$, we find that galaxies at a fixed stellar mass of $\log_{10}(M_*/M_\odot) = 11.0$ have an average size of 6.58 ± 1.04 kpc.

We are also interested in the size-stellar mass relation for spectroscopic cluster members only. The pivot mass $\log_{10}(M_*/M_\odot) \approx 10.5$ is smaller than the mass completeness limit

$\log_{10}(M_*/M_\odot) = 10.87$ of the HectoMAP survery (See Section 2.1.1). To examine the size-stellar mass relation in the context of the HectoMAP survey, we select only spectroscopic members with $(g - r) > 1.0$, D_n4000 > 1.5, and $\log_{10}(M_*/M_\odot) > 10.87$. We fit this size-stellar mass relation using the python package `linmix` (Kelly 2007). `linmix` is a Bayesian linear regression method that takes into account measurement errors. We only use `linmix` for this size-stellar mass relation because of the limited number of points. Using `linmix` for the other size-stellar mass relations would be too computationally intensive. Using the `linmix` fit method, we find the linear size-stellar mass relation above $\log_{10}(M_*/M_\odot) > 10.87$ to be

$$\log_{10}\left(\frac{R_{eff}}{1kpc}\right) = (0.782 \pm 0.211)\log_{10}\left(\frac{M_*}{10^{11}M_\odot}\right) + (0.665 \pm 0.217)\ . \qquad (6.6)$$

The right panel of Figure 6.4 shows the size-stellar mass relation for only spectroscopic members (squares) above $\log_{10}(M_*/M_\odot) > 10.87$ (Equation 6.6). The grey lines in the right panel of Figure 6.4 show the `linmix` fit. The size-stellar mass relation for our sample with $\log_{10}(M_*/M_\odot) > 10.87$, is shown plotted against the spectroscopic members which are colored by their D_n4000 value. We find the slope to be much steeper in the highest mass bin than in the other two lower mass bins. We also find the zero point to be the smallest in this bin. However, due to the small number of points, both the slope and zeropoint have large errors. At a fixed stellar mass of $\log_{10}(M_*/M_\odot) = 11.0$, we find that galaxies in our cluster have an average size of 4.62 ± 1.65 kpc.

From our analysis, we find that the slope of the size-stellar mass relation increases as we increase the lower mass limit. This is in agreement with previous results and provides evidence that there is a pivot mass in the size-stellar mass relation of our cluster. We also find that the average size of galaxies in our cluster at a stellar mass of $\log_{10}(M_*/M_\odot) = 11.0$ decreases as we increase the stellar mass lower limit. This is an interesting result as it may imply that there

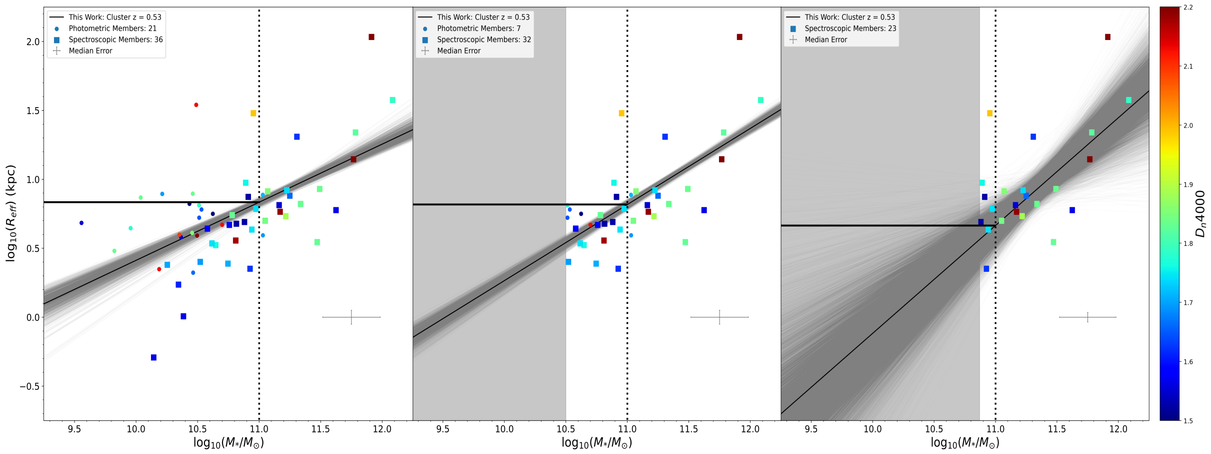

Figure 6.4: Three size-stellar mass relations from our sample of photometric cluster member candidates (circles) and spectroscopic members (squares) with varying stellar mass cuts. The solid black line represents the median relation in each panel and the grey lines are the confidence interval for each relation. Our full sample is shown in the left panel. The middle panel shows all objects with $\log_{10}(M_*/M_\odot) > 10.5$. The right panel shows only spectroscopic objects with $\log_{10}(M_*/M_\odot) > 10.87$. In each panel, we only fit objects that are within the stellar mass range. All points are colored by their calculated D_n4000 for spectroscopic members or their assigned D_n4000 for photometric cluster member candidates.

are large in size, lower mass galaxies within the cluster environment.

We compare our size-stellar mass relations to several other works shown in Figure 6.5. The panels are arranged in the same order as in Figure 6.4 except here we omit the size-stellar mass relation over our full mass range. We do this because of the known pivot mass in the size-stellar mass relation of quiescent galaxies. In Figure 6.5, the red region shows results from Damjanov et al. (2023), who study the size-stellar mass relation of galaxies in the field at redshifts $0.5 < z < 0.6$. The green and blue regions show the results from van der Wel et al. (2014) and represent the average size-stellar mass relation across all environments of quiescent galaxies at $z = 0.25$ and $z = 0.75$, respectively. Lastly, the purple region shows a result from George et al. (in prep.), who study the size-stellar mass relation of quiescent field galaxies over a large redshift range. Here we show a result from George et al. (in prep.) over the redshift range of $0.4 < z < 0.6$. We indicate the zeropoint of each work with a horizontal line colored to match the respective relation. The dashed black vertical line shows our fiducial mass of $\log_{10}(M_*/M_\odot) = 11.0$.

The linear size-stellar mass relation parameters for our work and the works we compare to are presented in Table 6.1.

Table 6.1: Size-stellar mass relations and comparison to previous works

Author	z	$\log_{10}(M_*/M_\odot)$	Slope	$R_{eff}(10^{11})^1$
Ridgeway 2023	0.53	9.4 - 12.1	0.426 ± 0.036	0.827 ± 0.015
Ridgeway 2023	0.53	10.5 - 12.1	0.550 ± 0.022	0.818 ± 0.016
Ridgeway 2023	0.53	10.87 - 12.1	0.782 ± 0.211	0.665 ± 0.217
van der Wel et al. 2014	0.25	> 10.3	0.75 ± 0.06	0.83 ± 0.03
George et al. in prep.	$0.4 < z < 0.6$	> 10.47	0.69 ± 0.04	0.70 ± 0.02
Damjanov et al. 2023	$0.5 < z < 0.6$	> 10.87	0.879 ± 0.029	0.615 ± 0.030
van der Wel et al. 2014	0.75	> 10.3	0.71 ± 0.03	0.63 ± 0.01

[1] (van der Wel et al. 2014) and (George et al. in prep.) defined zeropoints at 5×10^{10}, the value we report and compare to is extrapolated from the fit. We obtain errors through propagation of errors.

It has been shown that the slope of the size-stellar mass relation is more susceptible to changes in the samples mass range and therefore may not be the best parameter to use for comparison. The zeropoint has been found to be more robust to changes in the mass range samples. Therefore, for the remainder of our discussion, we will compare both slopes and zeropoints to other works. However, our main emphasis will be on analyzing the difference between our zeropoints and those in the literature.

To accurately compare our work to both van der Wel et al. (2014) and George et al. (in prep.), we must propagate the uncertainty measured on their zeropoints. This is necessary as we define our fiducial mass at $\log_{10}(M_*/M_\odot) = 11.0$, whereas van der Wel et al. (2014) and George et al. (in prep.) define theirs at $\log_{10}(M_*/M_\odot) = 10.7$. To account for this, we use the errors presented by both authors and propagate them in quadrature. In Table 6.1, column $R_{eff}(10^{11})$, we show the zeropoint at $\log_{10}(M_*/M_\odot) = 11.0$ along with the propagated uncertainty. We use these values throughout the remainder of our comparison to quantify statistical significance of the difference between our result to those we compare to.

It is important to note that both van der Wel et al. (2014) and George et al. (in prep.) utilize

`Galfit` (Peng et al. 2002) for their size measurements. In contrast, this work and (Damjanov et al. 2023), obtain size measurements using `SExtractor`. Both `Galfit` and `SExtractor` follow a similar formula for calculating galaxy sizes based on 2D fitting of photometry. Where `Galfit` outperforms `SExtractor` is in the fitting of irregularly shaped objects (Peng et al. 2010). However, it is well established that the morphology of cluster galaxies is dominated by elliptical galaxies (e.g. Postman & Geller 1984; Dressler 1980; Bamford et al. 2009). Therefore, we expect that the difference in size measurement between `Galfit` and `SExtractor` will not have a significant impact on our results.

The left panel of Figure 6.5 shows our size-stellar mass relation for spectroscopic members and photometric cluster member candidates with $\log_{10}(M_*/M_\odot) \geq 10.5$ against our four comparison works. We find that the slope of our size-stellar mass relation is shallower than all other works we compare to. However, our zeropoint is larger than all other comparison works except for van der Wel et al. (2014) at $z = 0.25$. The zeropoints at $\log_{10}(M_*/M_\odot) = 11.0$ for all other works are shown as solid lines. We find our zeropoint to be more than 4σ greater than George et al. (in prep.) and more than 5σ greater than Damjanov et al. (2023). Both George et al. (in prep.) and Damjanov et al. (2023) cover a similar redshift and mass range as the work presented here. We can therefore state that cluster member galaxies at a stellar mass of $\log_{10}(M_*/M_\odot) = 11.0$ and a redshift of $z = 0.53$, are on average, larger in size than their counterparts in the field.

Our zeropoint is within the measurement uncertainties and is not statistically significant for the (van der Wel et al. 2014) $z = 0.25$ size-stellar mass relation. However, we do find our zeropoint to be more than 9σ greater than (van der Wel et al. 2014) $z = 0.75$. If the size-stellar mass relation of the field is the same as that of the cluster environment, we would expect our size-stellar mass relation to fall almost exactly in the middle of (van der Wel et al. 2014), due to the evolution of the size-stellar mass relation over redshift. However, we find that our size-stellar mass relation is significantly closer to (van der Wel et al. 2014) $z = 0.25$. This indicates that galaxies within our cluster are experiencing a faster size evolution than those galaxies at similar masses in the field.

The right panel of Figure 6.5 shows our size-stellar mass relation for spectroscopic members with $\log_{10}(M_*/M_\odot) \geq 10.87$ along with our comparison works. We select objects with $\log_{10}(M_*/M_\odot) \geq 10.87$ as that is the completeness mass limit of the HectoMAP survey at $z = 0.53$. Only spectroscopic cluster members are included as our sample is complete above this mass limit.

It is important to note that the errors on the slope and zeropoint of our relation are quite large. This is a result of fitting only 23 spectroscopic members. We find the slopes of all comparison works to be within the measurement uncertainties of our slope. The zeropoints of all comparison works are also within the measurement uncertainties of our zeropoint. If we only select galaxies above the spectroscopic mass limit of $\log_{10}(M_*/M_\odot) \geq 10.87$, we find no statistically significant difference at any stellar mass between cluster and field galaxies.

We compare the size-stellar mass relation of our galaxy cluster, with two mass cuts, to the size-stellar mass relations of galaxies in the field. For the size-stellar mass relation of cluster galaxies with stellar mass $\log_{10}(M_*/M_\odot) \geq 10.5$, we find, at a fixed stellar mass of $\log_{10}(M_*/M_\odot) = 11.0$, galaxies in the cluster environment to be statistically larger in size than those in the field. However, for the size-stellar mass relation of cluster galaxies with stellar mass $\log_{10}(M_*/M_\odot) \geq 10.87$, we find, at a fixed stellar mass of $\log_{10}(M_*/M_\odot) = 11.0$, galaxies in the cluster environment and in the field to be indistinguishable in size. This leads us to conclude that there is a mechanism, or mechanisms, that influences galaxies with stellar mass $\log_{10}(M_*/M_\odot) \leq 10.87$ within the cluster environment and results in increased galaxy size.

With our current data, we cannot determine which mechanism is responsible for the accelerated size growth of cluster galaxies. However, based on processes discussed in the literature, we

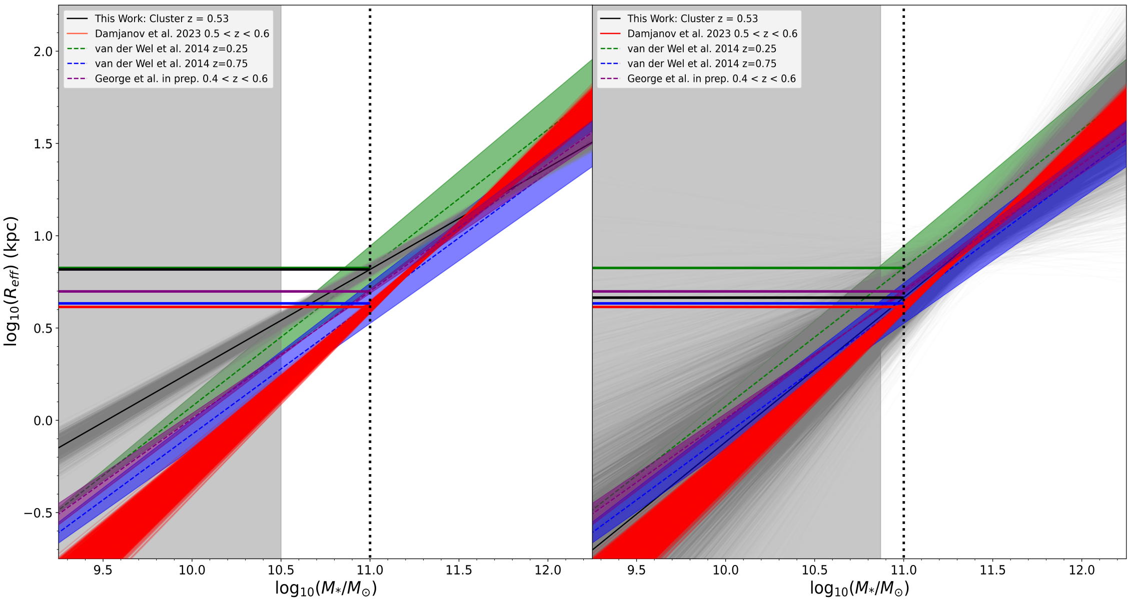

Figure 6.5: Size-stellar mass relation for cluster galaxies $\log_{10}(M_*/M_\odot) \geq 10.5$ (left panel) and cluster galaxies $\log_{10}(M_*/M_\odot) \geq 10.87$ (right panel) compared to four other works. The relations we compare to are (Damjanov et al. 2023) $0.5 < z < 0.6$ shown in red, (van der Wel et al. 2014) $z = 0.25$ in green and $z = 0.75$ in blue, and (George et al. in prep.) $0.4 < z < 0.6$ shown in purple. The grey section in each panel represents the lowest mass we fit. We discuss how our slope and zeropoint compares to these works in the text.

can discuss which is most probable. We hypothesize that the most probable cause of the increase in size of cluster member galaxies with stellar mass $\log_{10}(M_*/M_\odot) \geq 10.5$ is minor mergers. Previous theoretical and observational works show that minor mergers occur both frequently throughout a galaxies history and result in a large change in galactic size for a small change in stellar mass (White et al. 2007; Bezanson et al. 2009; Khochfar & Silk 2009; Naab et al. 2009; Genel et al. 2009; Lotz et al. 2011; Newman et al. 2012; Cappellari 2013). In addition, it has been found in the literature that adiabatic expansion via stellar mass loss or AGN feedback may contribute to quiescent cluster galaxy size growth (Damjanov et al. 2009; Sweet et al. 2017; Andreon et al. 2016; Fan et al. 2001; Laporte et al. 2013; Choi et al. 2018). We discuss ways to disentangle to true cause of the size growth of galaxies in cluster in Section 7.1.

Chapter 7

Conclusions and Future Work

Galaxy clusters act as excellent laboratories where we can observe the accelerated evolution of individual galaxies (Dressler 1980; Cooper et al. 2012; Jørgensen & Chiboucas 2013; Delaye et al. 2014; Morishita et al. 2017; Chan et al. 2018). Our cluster was selected for follow up observations because it is a unique example of a massive merging cluster. We obtain follow up observational data using Keck LRIS (section 2.1.2). After processing raw spectra from LRIS (Chapter 3), we calculate redshifts of LRIS objects to determine cluster membership (Section 4.1). For LRIS and HectoMAP cluster members, we calculate D_n4000 (Section 4.2), which we use throughout our analysis as a proxy for the average age of the galaxy stellar population. We select a sample of photometric cluster member candidates (Section 2.2) and create a statistical correction to account for missing spectroscopic cluster members that are below the completeness magnitude limit of HectoMAP (Chapter 5). Using this statistical correction, in unison with our available spectroscopic measurements, we analyze the relation of $D_n4000 - R_{cl}/R_{200}$ (Section 6.1) and the size-stellar mass relation (Section 6.2) of our galaxy cluster. Our results are as follows:

- Through the follow up observations using Keck LRIS, we identify and confirm 25 new spectroscopic galaxy cluster members. This represents a 78% increase in the known spectroscopic cluster membership (Section 4.1).

- Using photometric data, we create a catalog of photometric cluster member candidates that are near the cluster on the sky and have photometric redshifts within the velocity dispersion of the cluster. We assign these photometric cluster member candidates D_n4000 values. By using this catalog of photometric cluster member candidates with the spectroscopic cluster members, we now have a sample of 1000 mock galaxy clusters. With this statistical correction, we examine the estimated range of properties for cluster members and how those properties change as a function of clustercentric distance.

- Using both the spectroscopic members and the photometric cluster member candidates, we analyze the trend of $D_n4000 - R_{cl}/R_{200}$ (Figure 6.2). We find that the trend $D_n4000 - R_{cl}/R_{200}$ is flat, within errors, for our cluster. We infer that galaxies at small and large clustercentric distances have stellar populations of similar ages. Based on the zeropoint of our relation, we infer that the median galaxy stellar population age of our cluster is ≈ 5 Gyr. We also observe a mixture of star forming and quenched galaxies at all cluster radii. These results act as an independent confirmation that this cluster is in fact merging.

- We analyze the size-stellar mass relation (Section 6.2) of our spectroscopic members and photometric cluster member candidates using three different mass cuts. We examine the size-stellar mass relation of our entire sample over the stellar mass range $9.4 \leq \log_{10}(M_*/M_\odot) \leq 12.1$. However, it has been well established by previous works that the size-stellar mass relation for quiescent galaxies has a strong positive correlation above stellar mass of $\log_{10}(M_*/M_\odot) > 10.5$ (e.g. Shen et al. 2003a; Williams et al. 2010; van der Wel et al. 2014; Mowla et al. 2019a; George et al. in prep.). To account for this pivot in the size-stellar mass relation, we fit spectroscopic members and photometric cluster members candidates above stellar mass of $\log_{10}(M_*/M_\odot) > 10.5$. Lastly, we examine the size-stellar mass relation for spectroscopic members only above the mass completeness limit $\log_{10}(M_*/M_\odot) > 10.87$ of the HectoMAP survey. Our results for each mass cut are as follows:

- For our full sample of spectroscopic members and photometric cluster member candidates with $(g - r) > 1.0$ and $D_n4000 > 1.5$, we find that galaxies at a fixed stellar mass of $\log_{10}(M_*/M_\odot) = 11.0$ have an average size of 6.71 ± 1.04 kpc. We do not compare this result to other works as it covers a broad mass range and does not accurately represent the nature of the size-stellar mass relation for quiescent galaxies.
- For spectroscopic cluster members and photometric cluster member candidates with $(g - r) > 1.0$, $D_n4000 > 1.5$, and $\log_{10}(M_*/M_\odot) > 10.5$, we find that galaxies at a fixed stellar mass of $\log_{10}(M_*/M_\odot) = 11.0$ have an average size of 6.58 ± 1.04 kpc. Comparing our results to (George et al. in prep.), we find that quiescent cluster member galaxies, at a stellar mass of $\log_{10}(M_*/M_\odot) = 11.0$ and a redshift of $z = 0.53$, are on average 30% larger in size than quiescent galaxies in the field at similar redshifts.
- For spectroscopic cluster members only with $(g - r) > 1.0$, $D_n4000 > 1.5$, and $\log_{10}(M_*/M_\odot) > 10.87$, we find that galaxies at a fixed stellar mass of $\log_{10}(M_*/M_\odot) = 11.0$ have an average size of 4.62 ± 1.65 kpc. Comparing our results to (Damjanov et al. 2023), we find that quiescent cluster member galaxies at a stellar mass of $\log_{10}(M_*/M_\odot) = 11.0$ and a redshift of $z = 0.53$, have similar sizes, within errors, to queiscent galaxies in the field.

7.1 Future Work

Future work from this thesis can go in several directions. The most obvious next step would be to obtain spectroscopic observations for our catalog of photometric cluster member candidates. Currently, the cluster relations we examine of $D_n4000 - R_{cl}/R_{200}$ and size-stellar mass represent the range of possible relations for our cluster. By spectroscopically confirming our photometric cluster member candidates, we will be able to better constrain these cluster relations. Confirming additional members will also allow us to characterize these relations to lower stellar mass cluster galaxies and across larger clustercentric distances

Alternatively, we could examine the cause of the size growth of cluster galaxies. It has been theorized that the size growth of quiescent galaxies in the cluster environment is primarily a result of minor mergers (Bezanson et al. 2009; White et al. 2007; Naab et al. 2009; Nipoti et al. 2009; Newman et al. 2012; McLure et al. 2013; van Dokkum et al. 2015; Faisst et al. 2017; Damjanov et al. 2023). To understand if minor mergers are driving the growth of quiescent galaxies in our cluster, we could measure the surface brightness profiles of cluster members. Surface brightness profiles of galaxies have been shown to trace the merger history of galaxies as well as allowing us to distinguish between minor and major merger events (e.g Hopkins et al. 2010; Hilz et al. 2013).

We could also analyze cosmological hydrodynamical simulations of galaxy clusters to better understand how quenching mechanism affect cluster members (e.g. Borgani & Kravtsov 2011). For our cluster, we observe a flat trend of $D_n4000 - R_{cl}/R_{200}$, utilizing simulation data could help us form a more complete understanding as to which quenching mechanisms are the cause of this trend. Additionally, we can analyze at what clustercentric distances quiescent galaxies experience the most size growth. A likely hydrodynamical simulation code we could use to probe these relations is `GADGET-4` (Springel et al. 2021).

Lastly, we can collect spectra of the lensed arcs. We can do this by using LRIS and increasing the exposure time of our science frames. Our cluster offers us the unique opportunity of having multiple massive galaxies that are associated with strong lensing arcs. Obtaining spectra of lensed arcs would allow us to map the total mass distribution of these massive galaxies. With the total mass distribution, we can map the dark matter distribution of individual massive galaxies. This would allow us to measure how the profile of dark matter changes as a function of galaxy size. This is a relatively understudied field as there is a limited number of massive galaxies with strong lensing arcs.

Appendix

A.1 Keck LRIS Spectra

Here we present a summary of our reduced spectrum for all LRIS cluster members. In the following figures the top panel is the 1D coadded spectrum and the second panel shows the 2D coadded object model spectrum. The following three pairs of panels are the individual science frames 2D object model spectrum above the modeled sky emission, respectively. We show examples of strong absorption galaxies in Figures A.1, A.2, A.3, A.4, A.5, A.7, A.8, A.12, A.13, A.14, A.15, A.16, A.17, A.18, A.19, A.20, A.21, A.22, A.24. We show examples of objects with OII emission in Figures A.6, A.9, A.10, A.11, A.23, A.25.

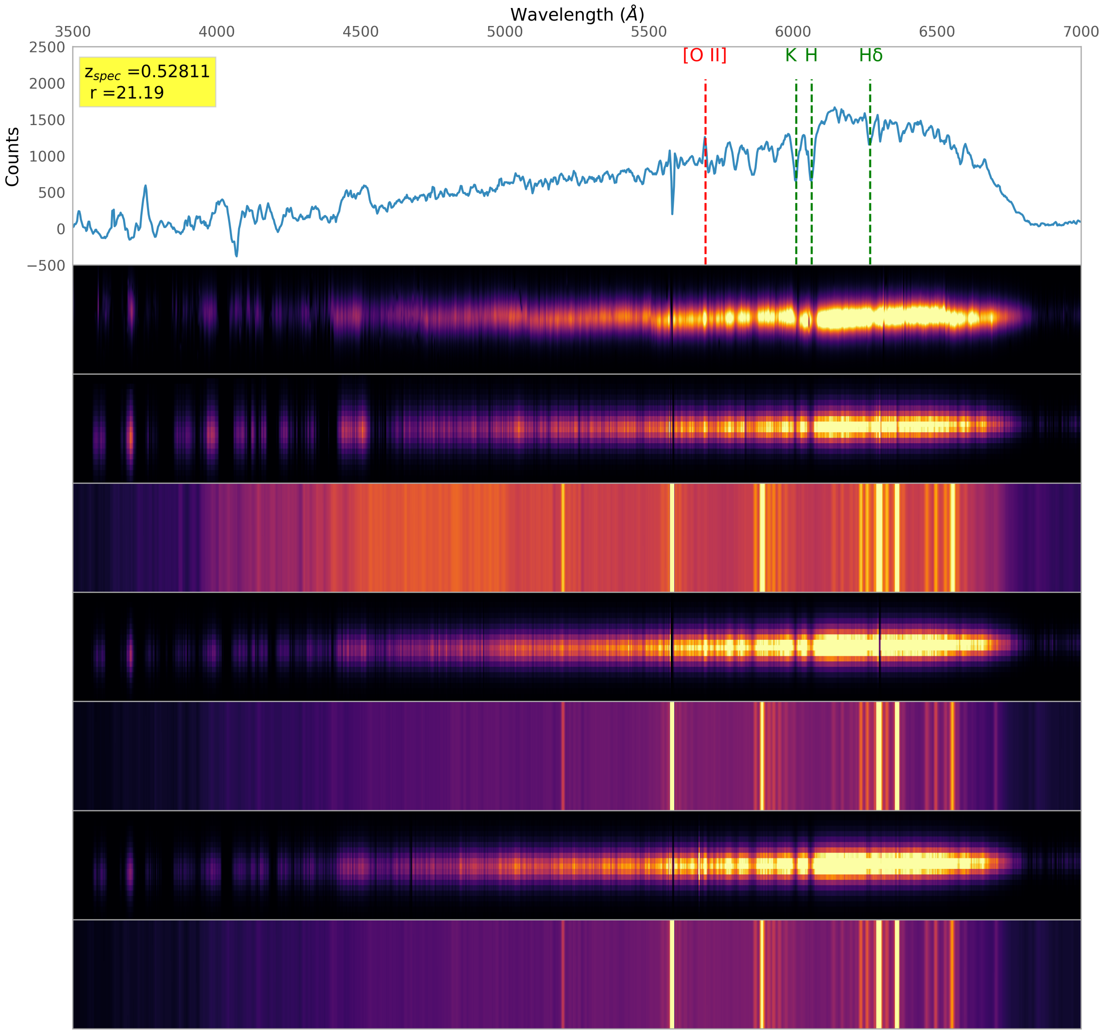

Figure A.1: Object HM_g006. (R.A., Dec. = 247.439764, 43.822285) deg.

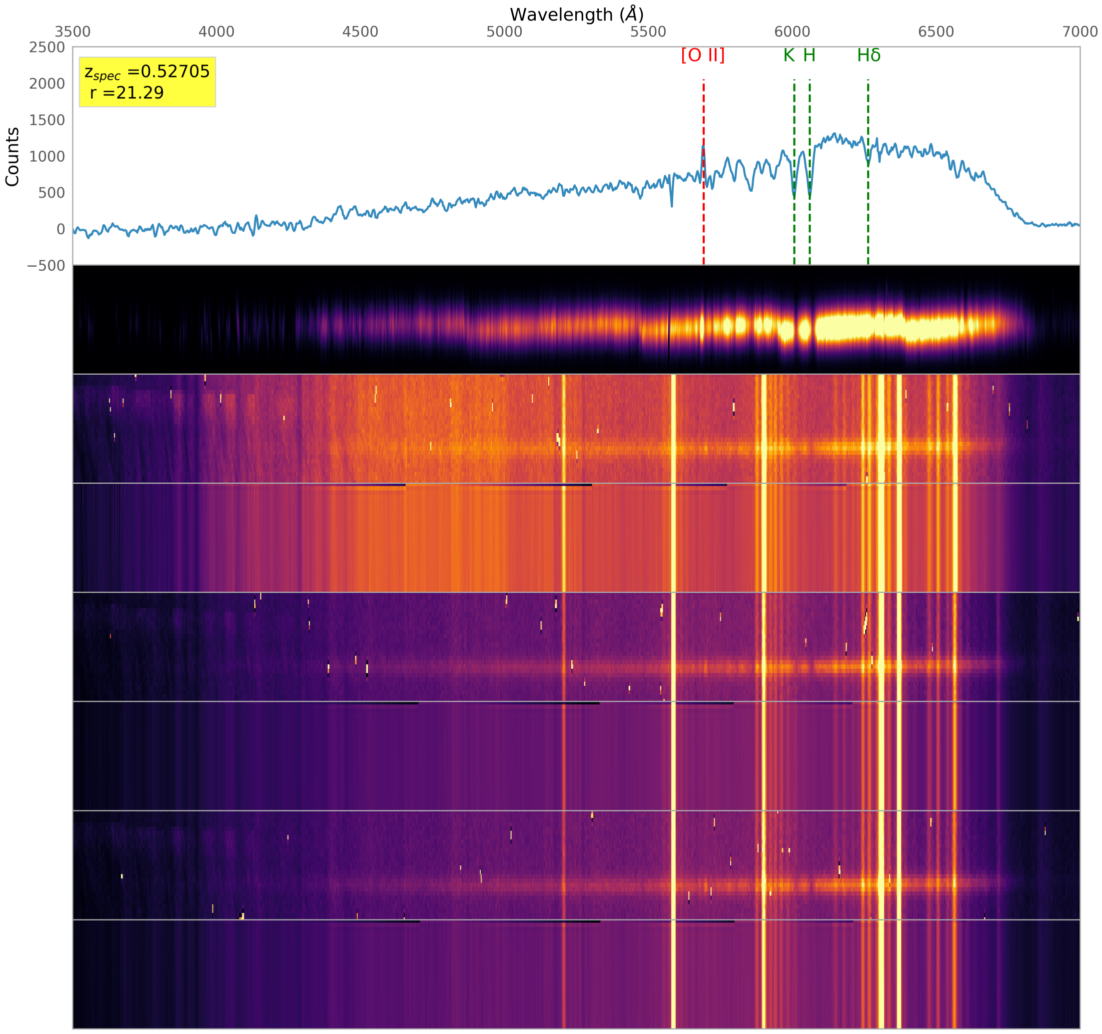

Figure A.2: Object HM_g008. (R.A., Dec. = 247.447263, 43.856375) deg.

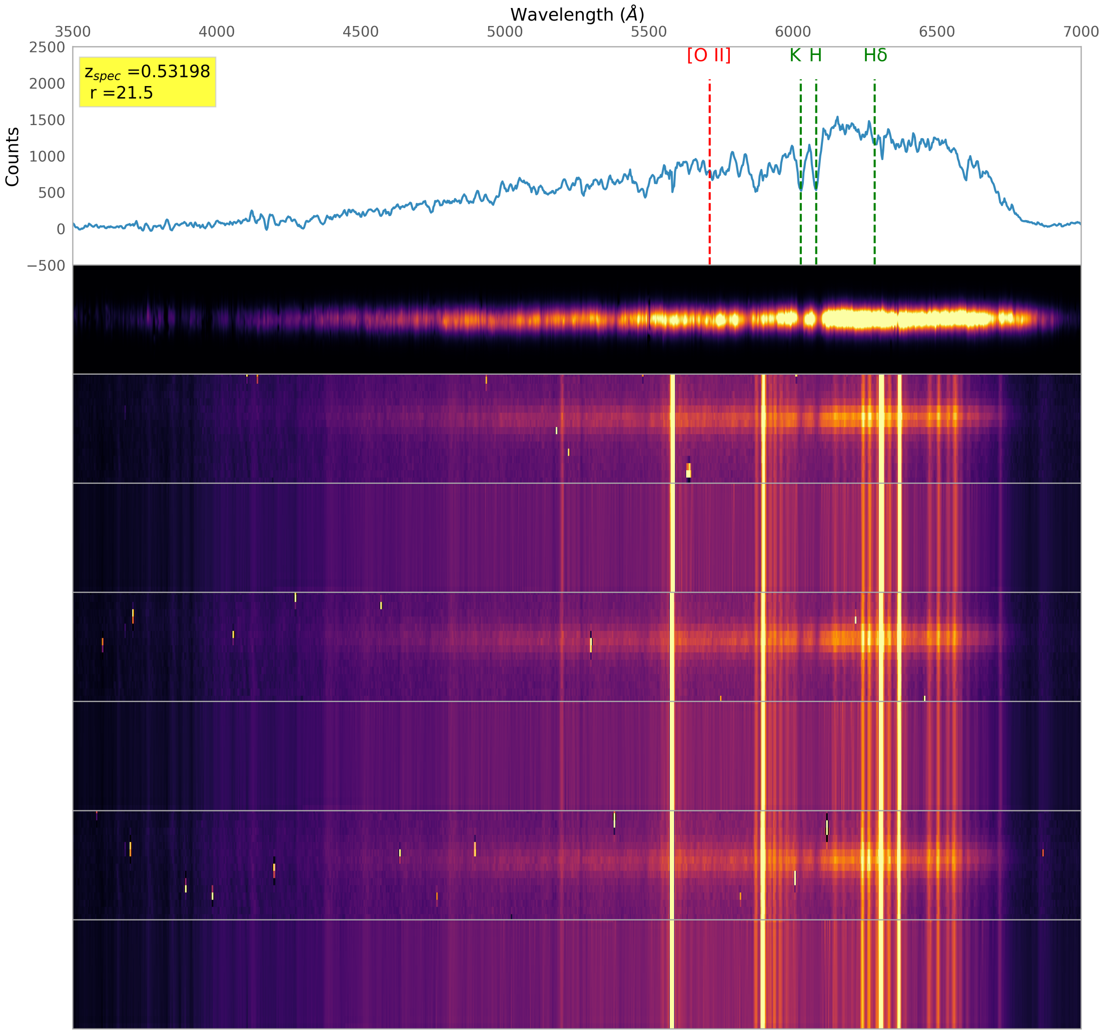

Figure A.3: Object HM_g013. (R.A., Dec. = 247.460209, 43.833598) deg.

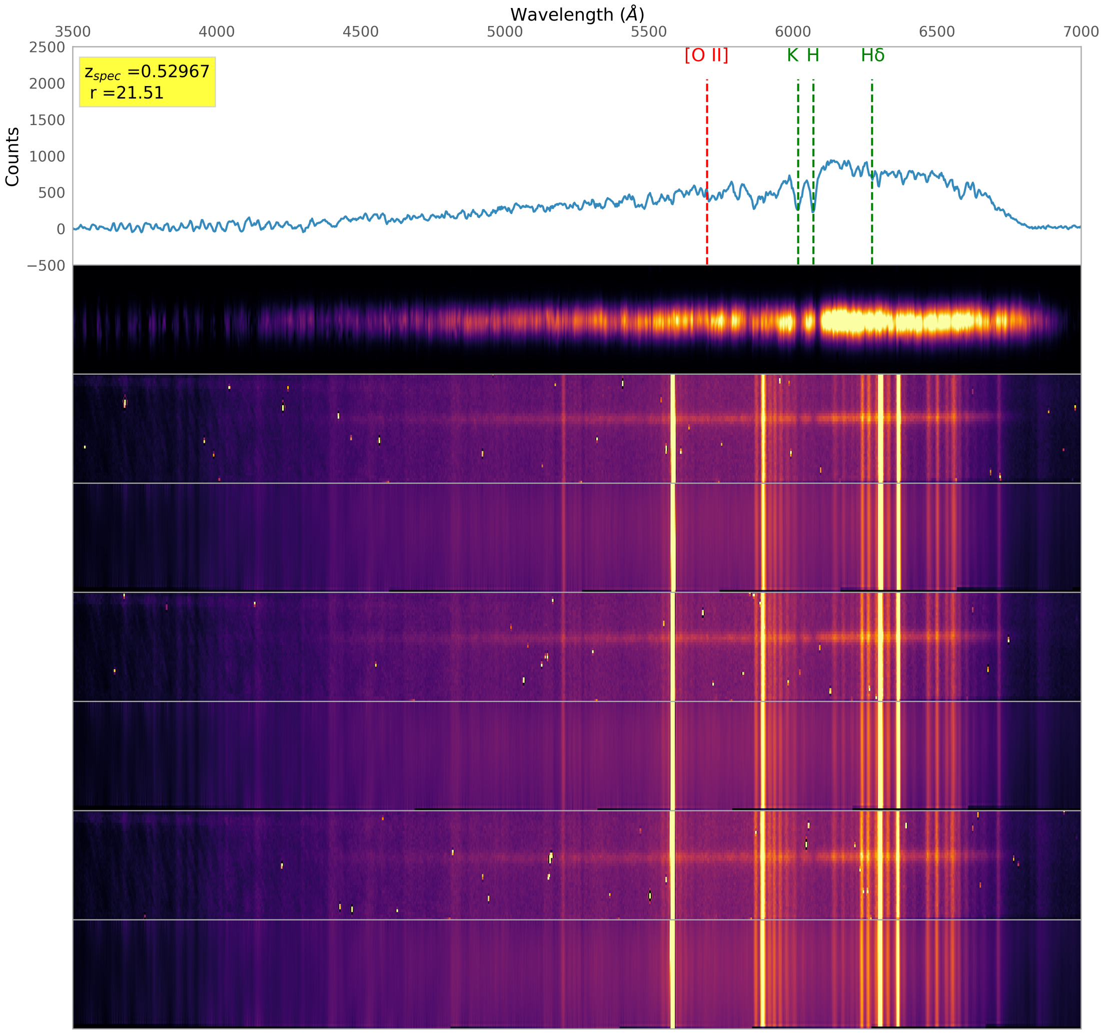

Figure A.4: Object HM_g014. (R.A., Dec. = 247.442601, 43.848417) deg.

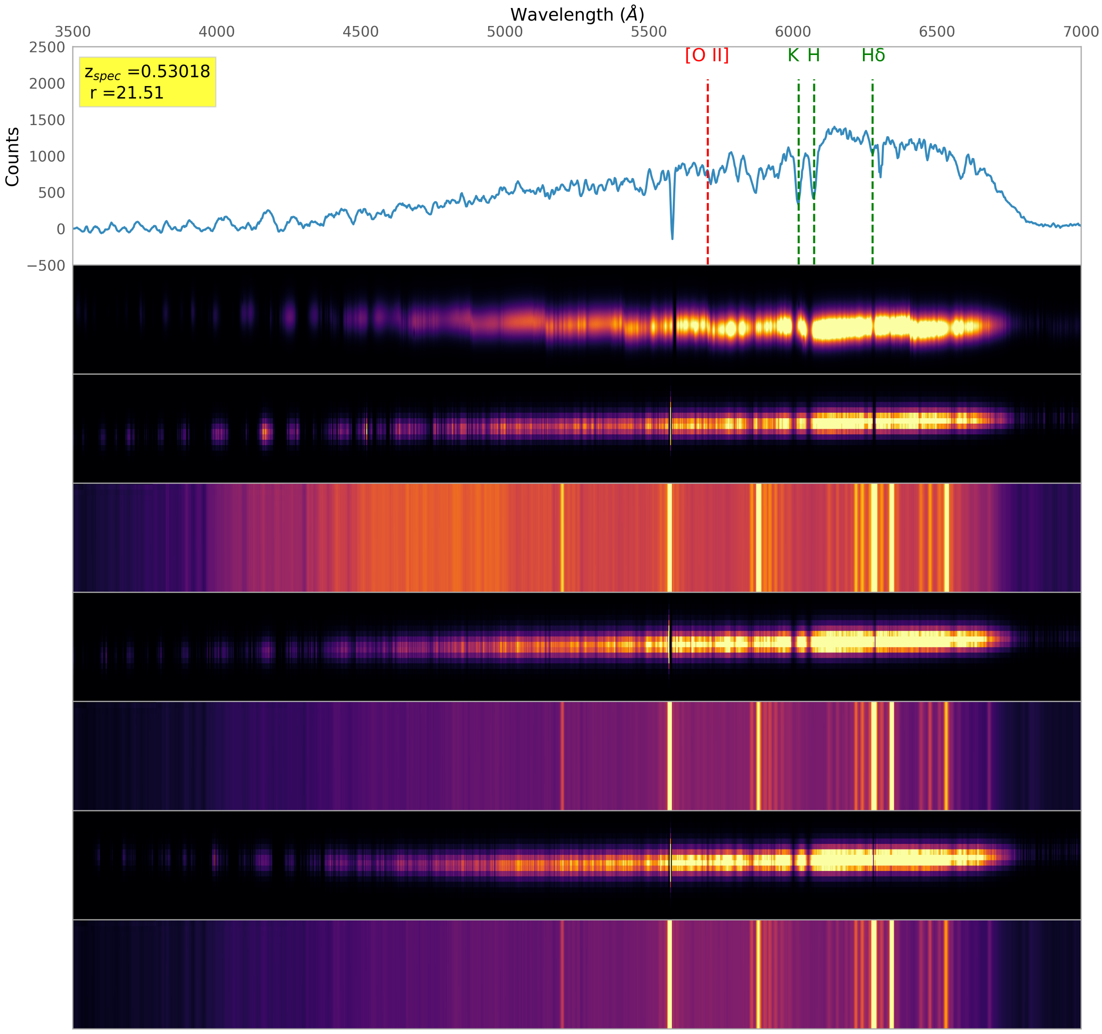

Figure A.5: Object HM_g015. (R.A., Dec. = 247.417143, 43.824986) deg.

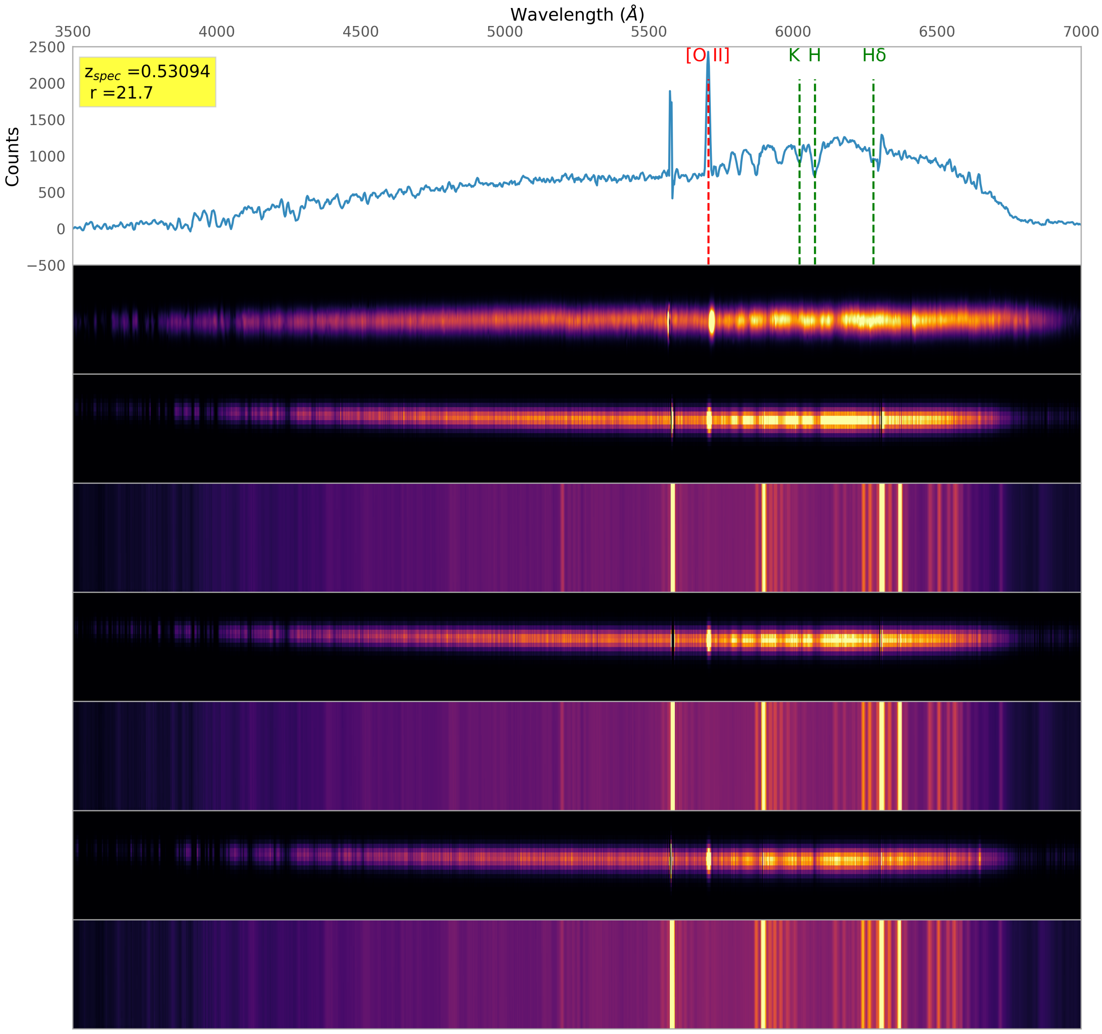

Figure A.6: Object HM_g022. (R.A., Dec. = 247.461386, 43.856980) deg.

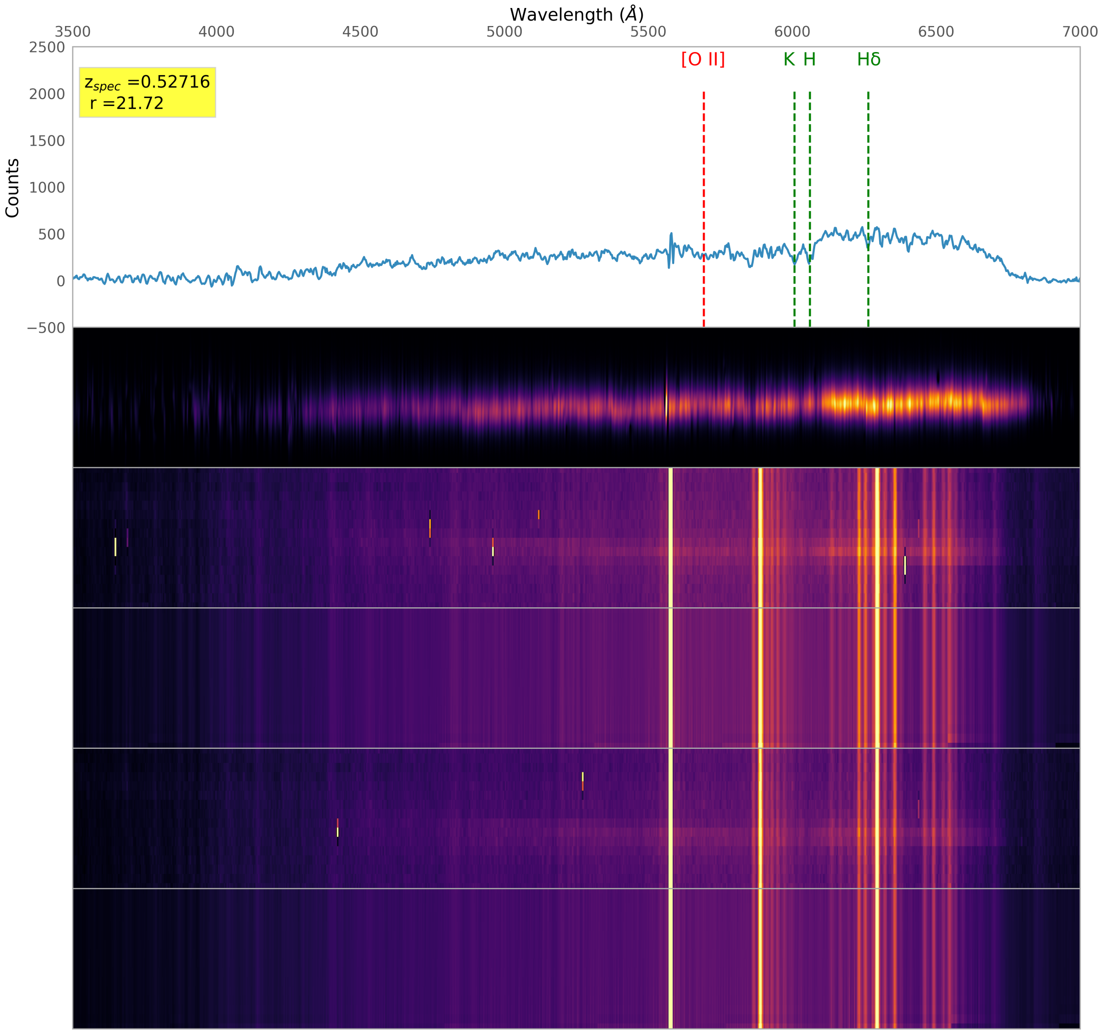

Figure A.7: Object HM_g023. (R.A., Dec. = 247.436304, 43.849075) deg.

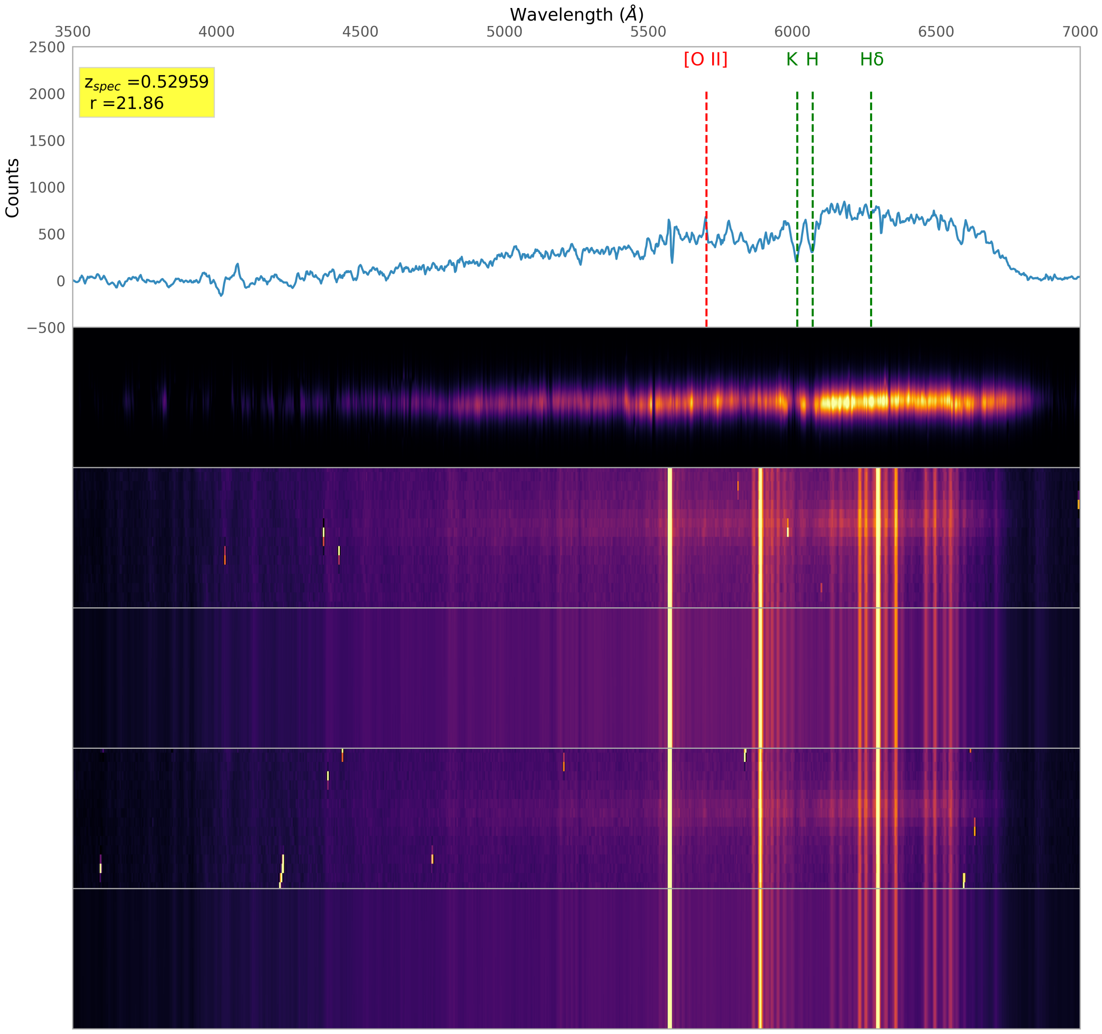

Figure A.8: Object HM_g027. (R.A., Dec. = 247.448858, 43.834449) deg.

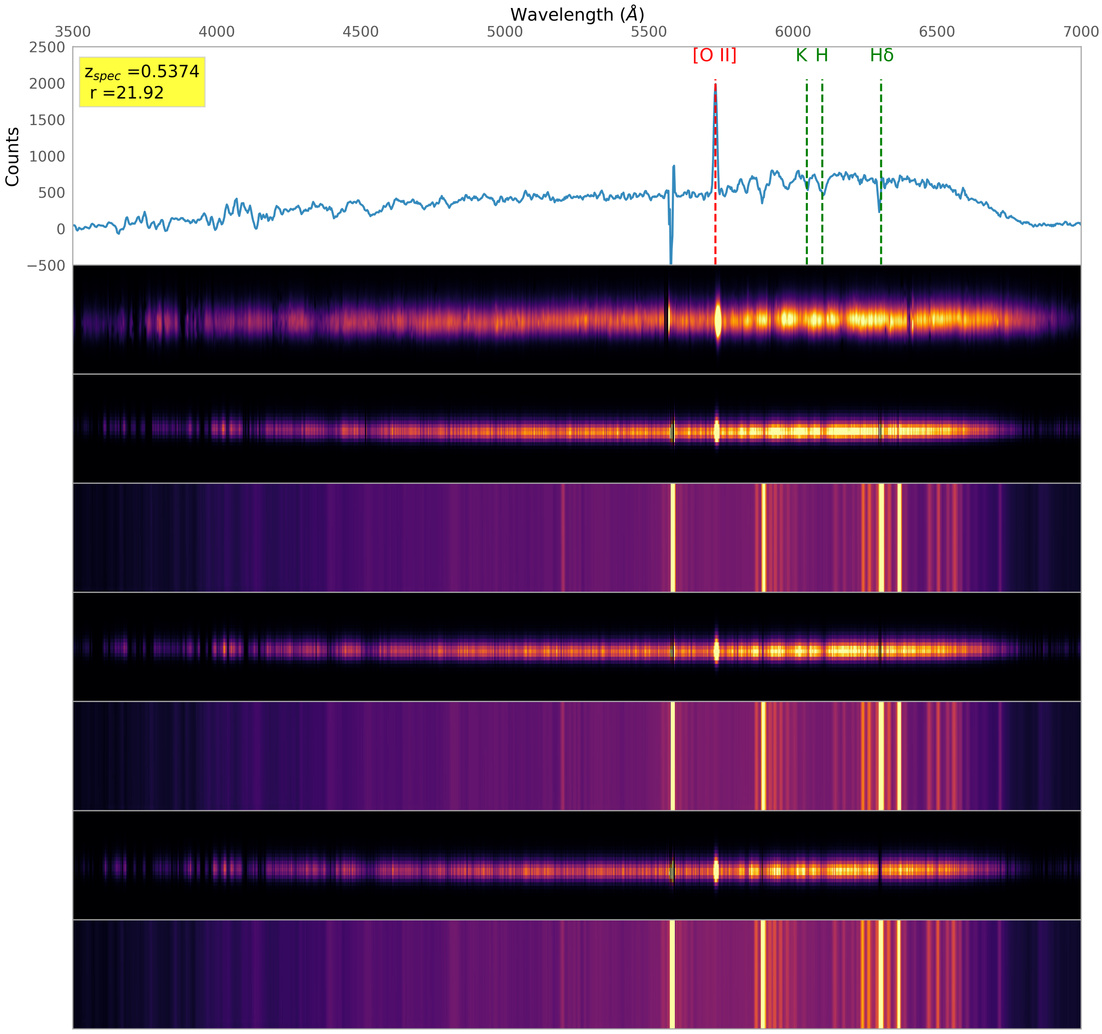

Figure A.9: Object HM_g029. (R.A., Dec. = 247.453838, 43.843891) deg.

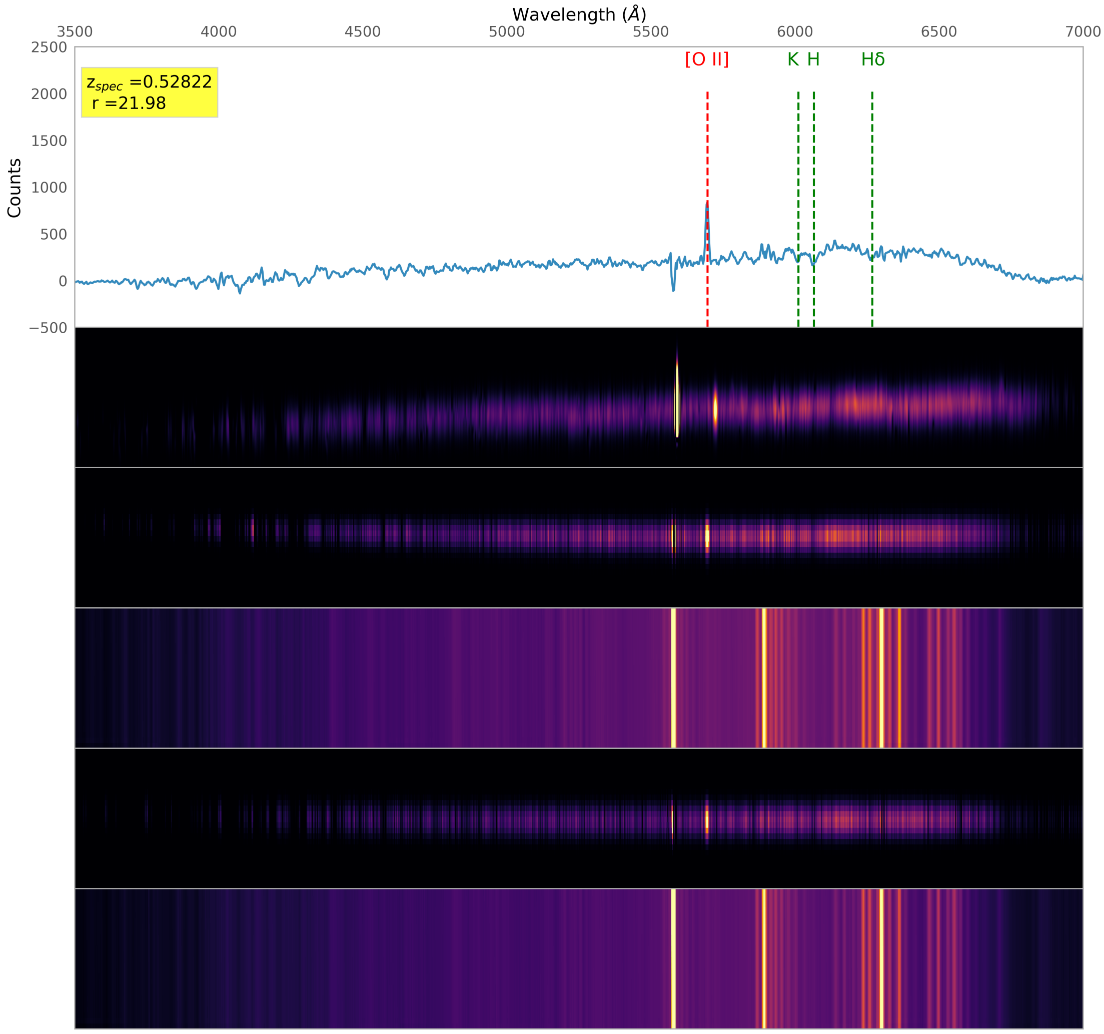

Figure A.10: Object HM_g030. (R.A., Dec. = 247.449075, 43.854239) deg.

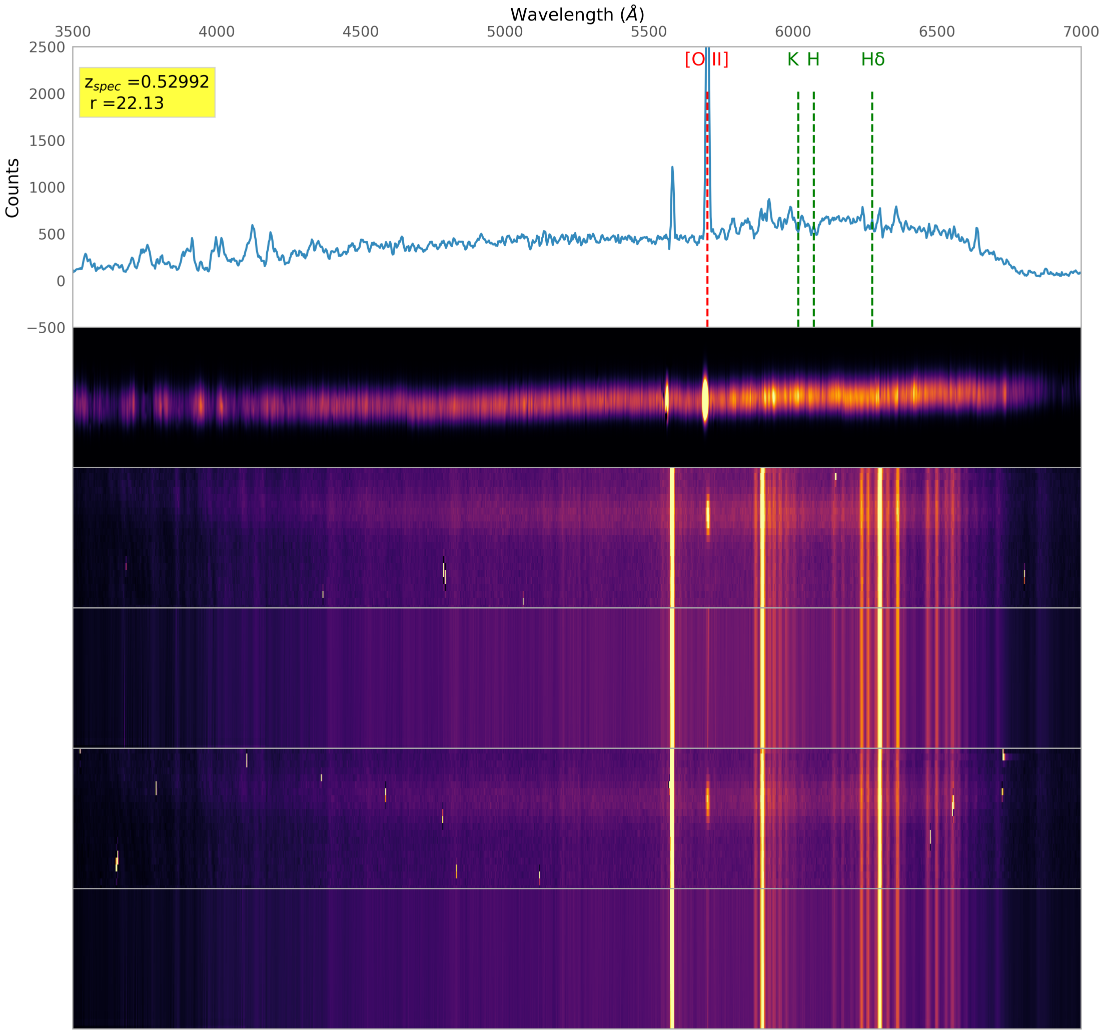

Figure A.11: Object HM_g034. (R.A., Dec. = 247.452979, 43.857650) deg.

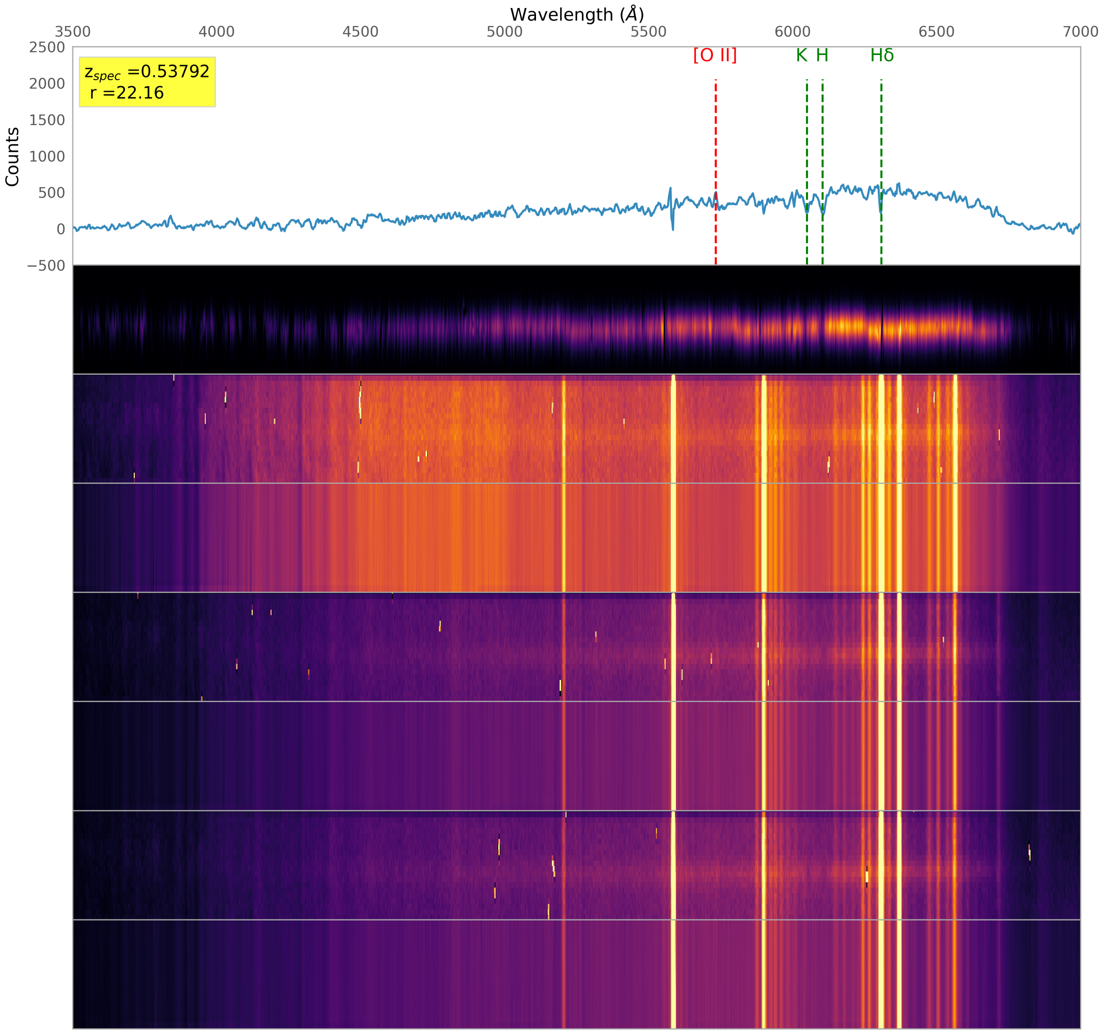

Figure A.12: Object HM_g035. (R.A., Dec. = 247.445343, 43.853748) deg.

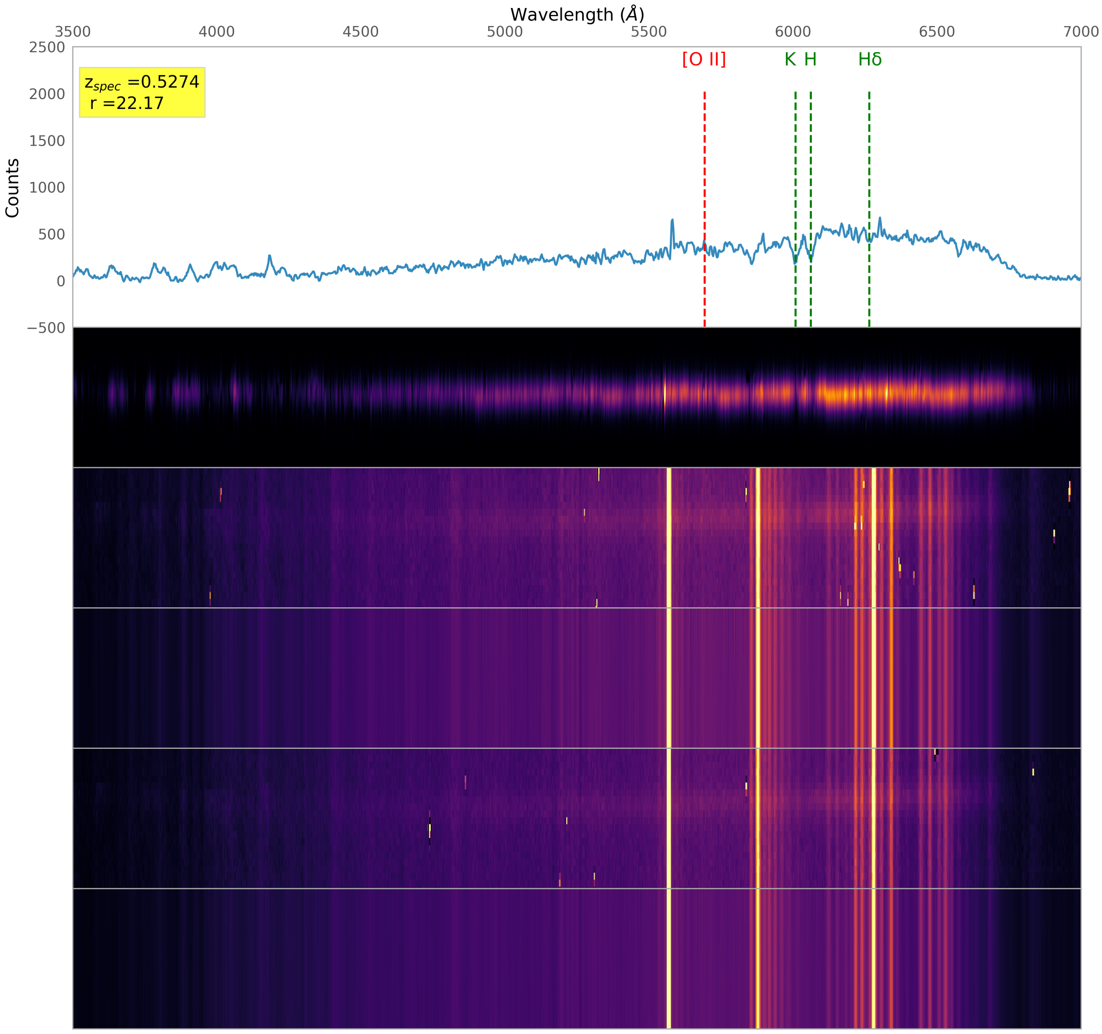

Figure A.13: Object HM_g036. (R.A., Dec. = 247.421041, 43.844545) deg.

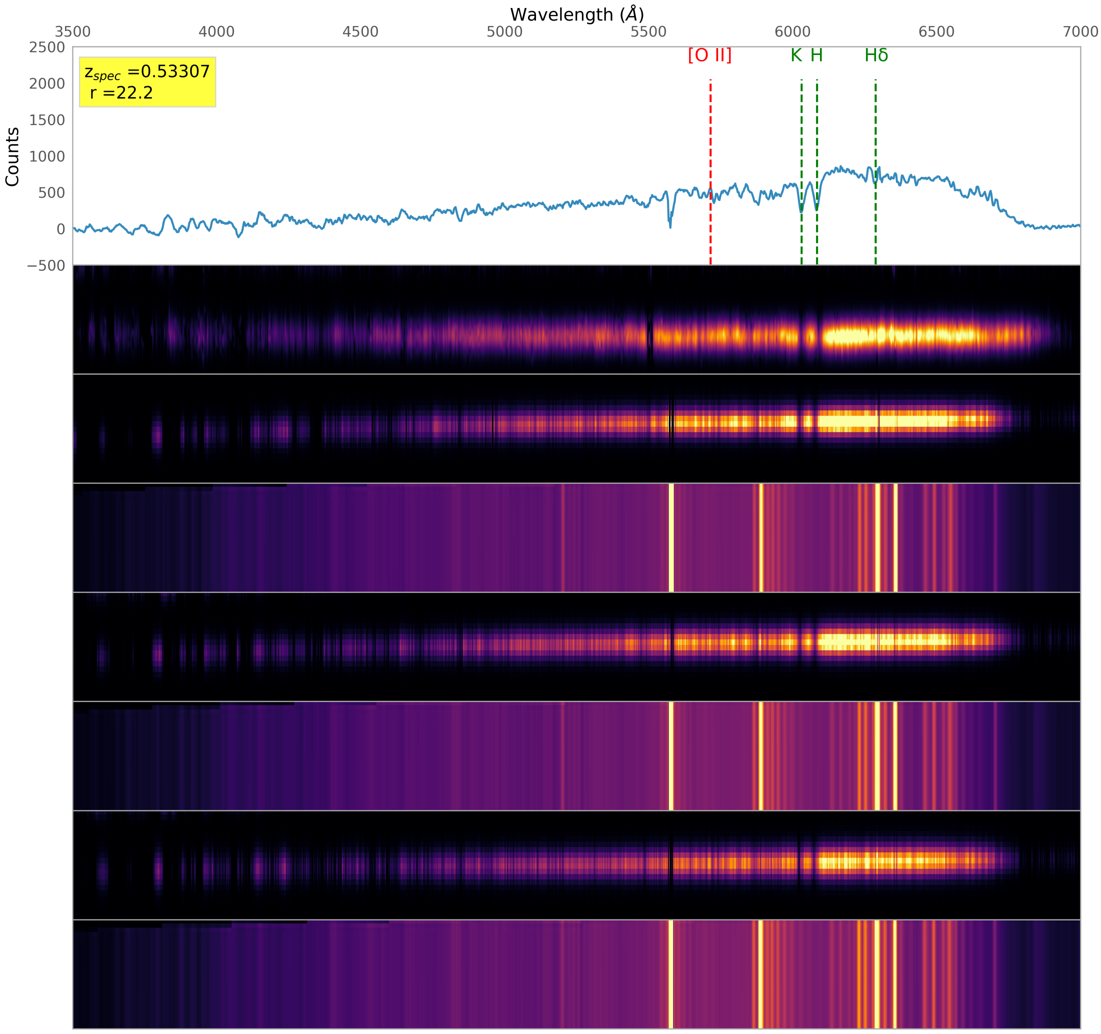

Figure A.14: Object HM_g038. (R.A., Dec. = 247.430965, 43.821909) deg.

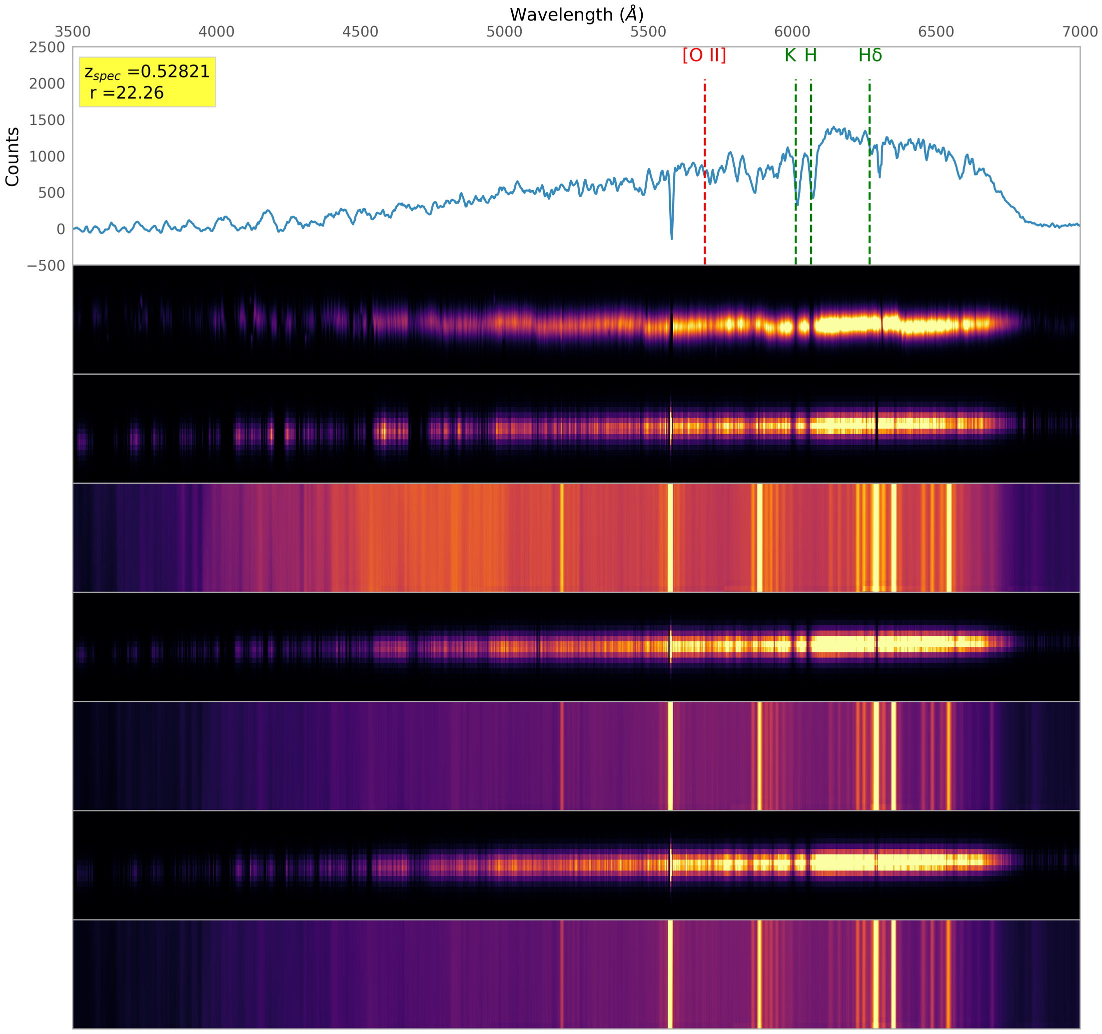

Figure A.15: Object HM_g041. (R.A., Dec. = 247.428056, 43.817335) deg.

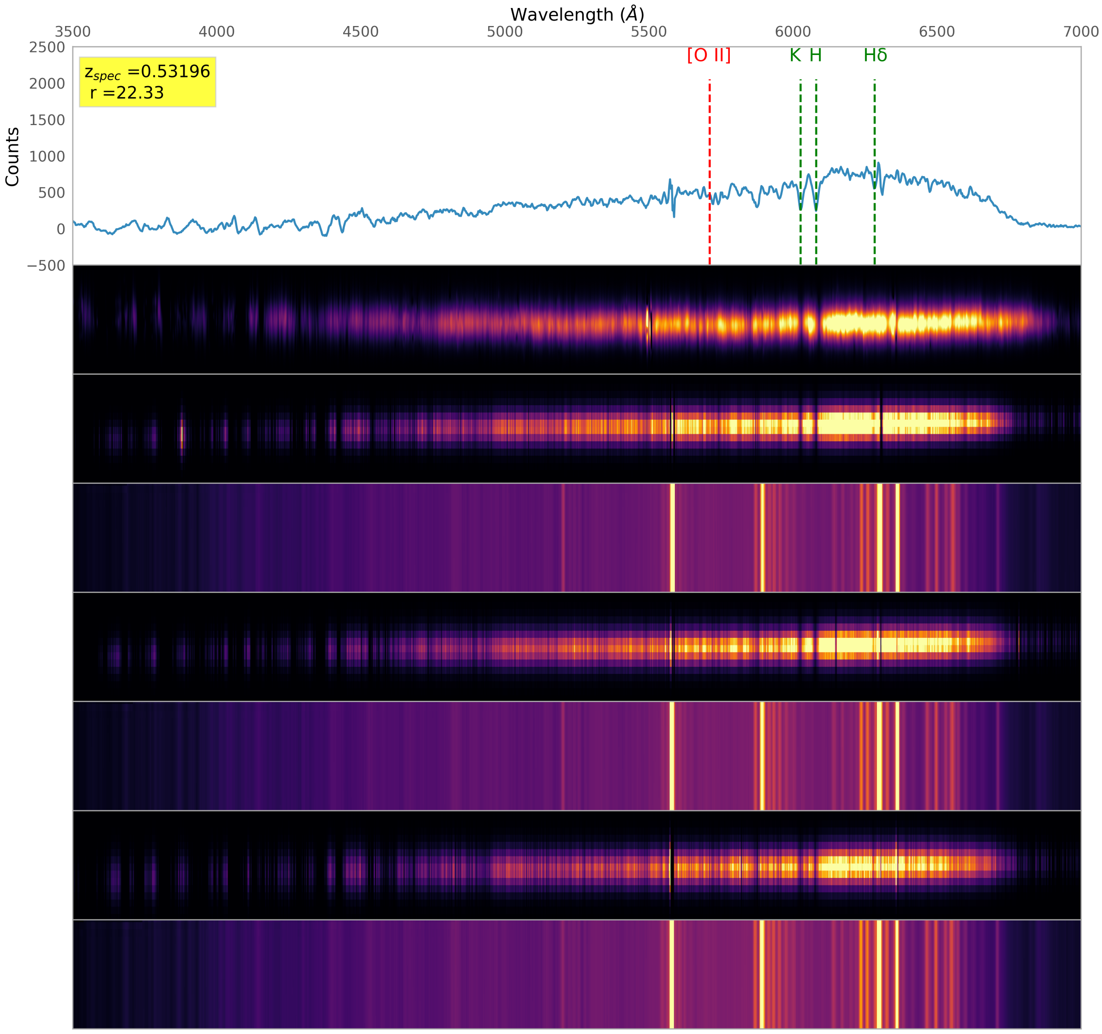

Figure A.16: Object HM_g046. (R.A., Dec. = 247.439267, 43.826324) deg.

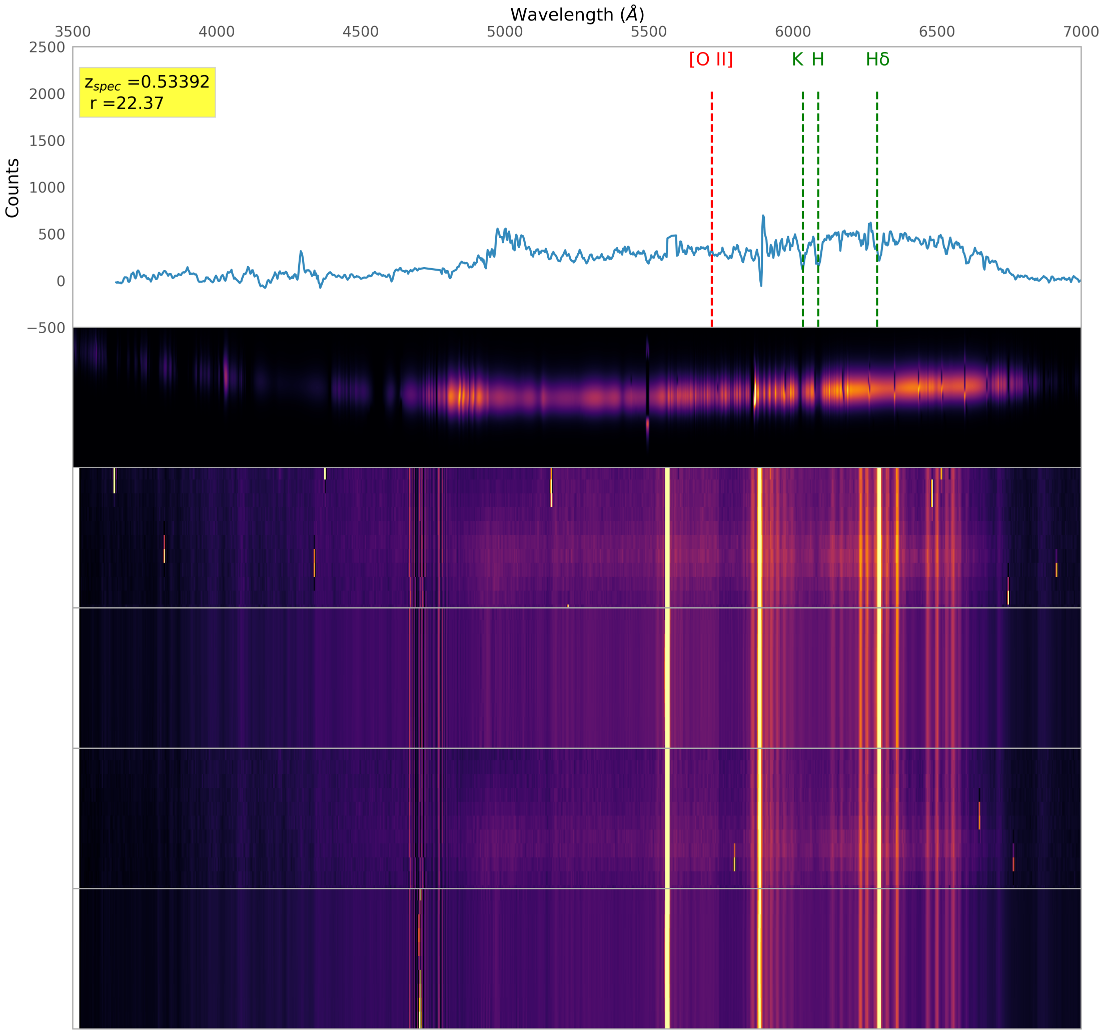

Figure A.17: Object HM_g051. (R.A., Dec. = 247.481543, 43.837080) deg.

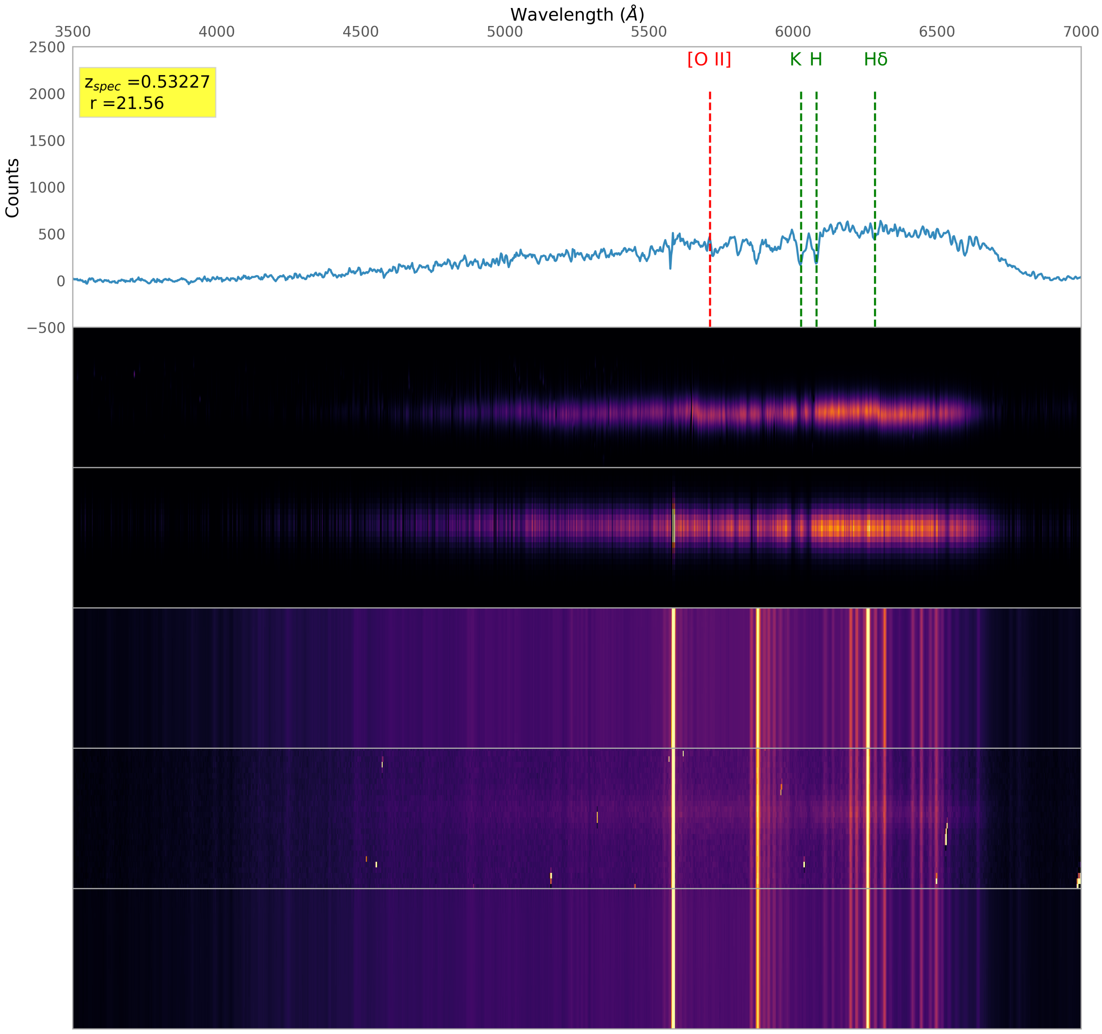

Figure A.18: Object HM_g096. (R.A., Dec. = 247.395519, 43.803017) deg.

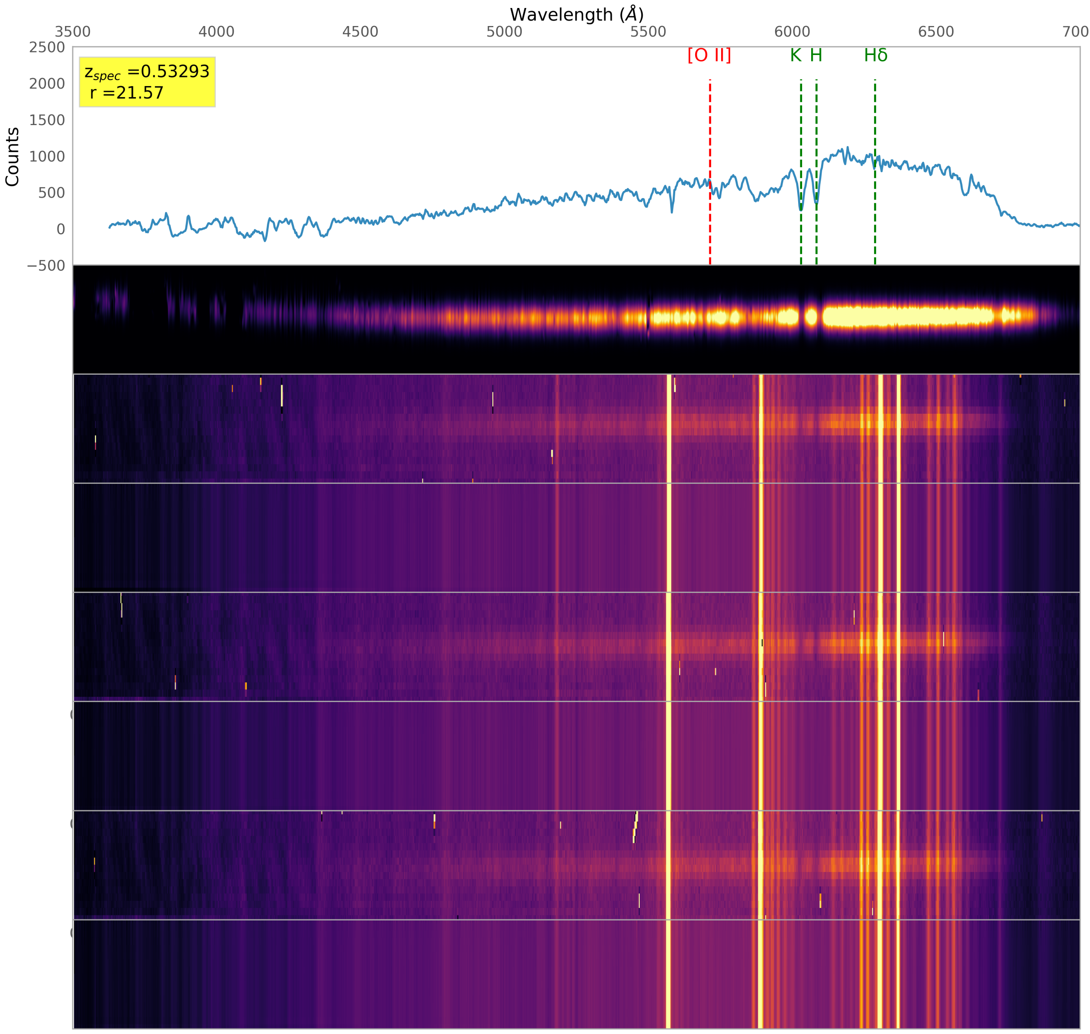

Figure A.19: Object HM_g097. (R.A., Dec. = 247.481079, 43.813323) deg.

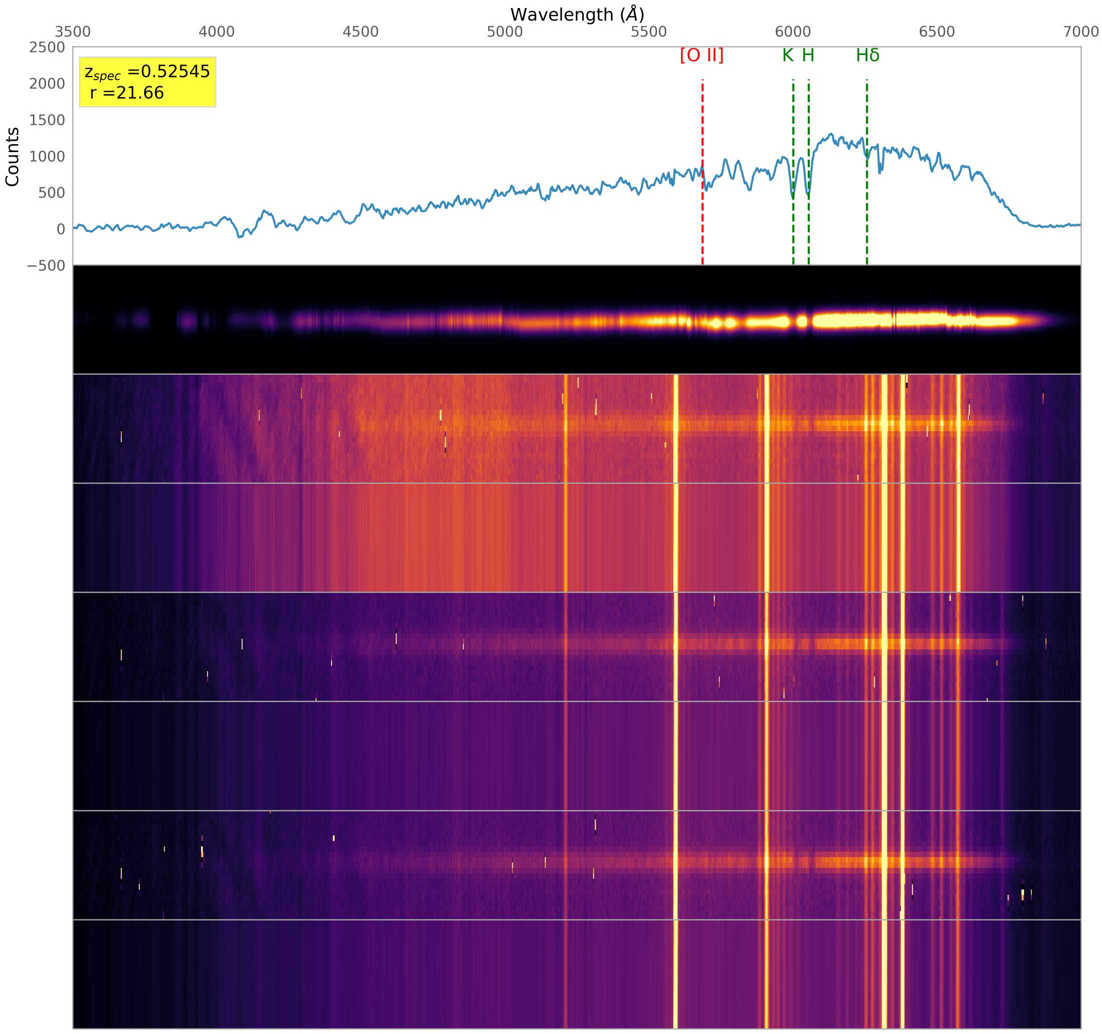

Figure A.20: Object HM_g101. (R.A., Dec. = 247.453005, 43.803898) deg.

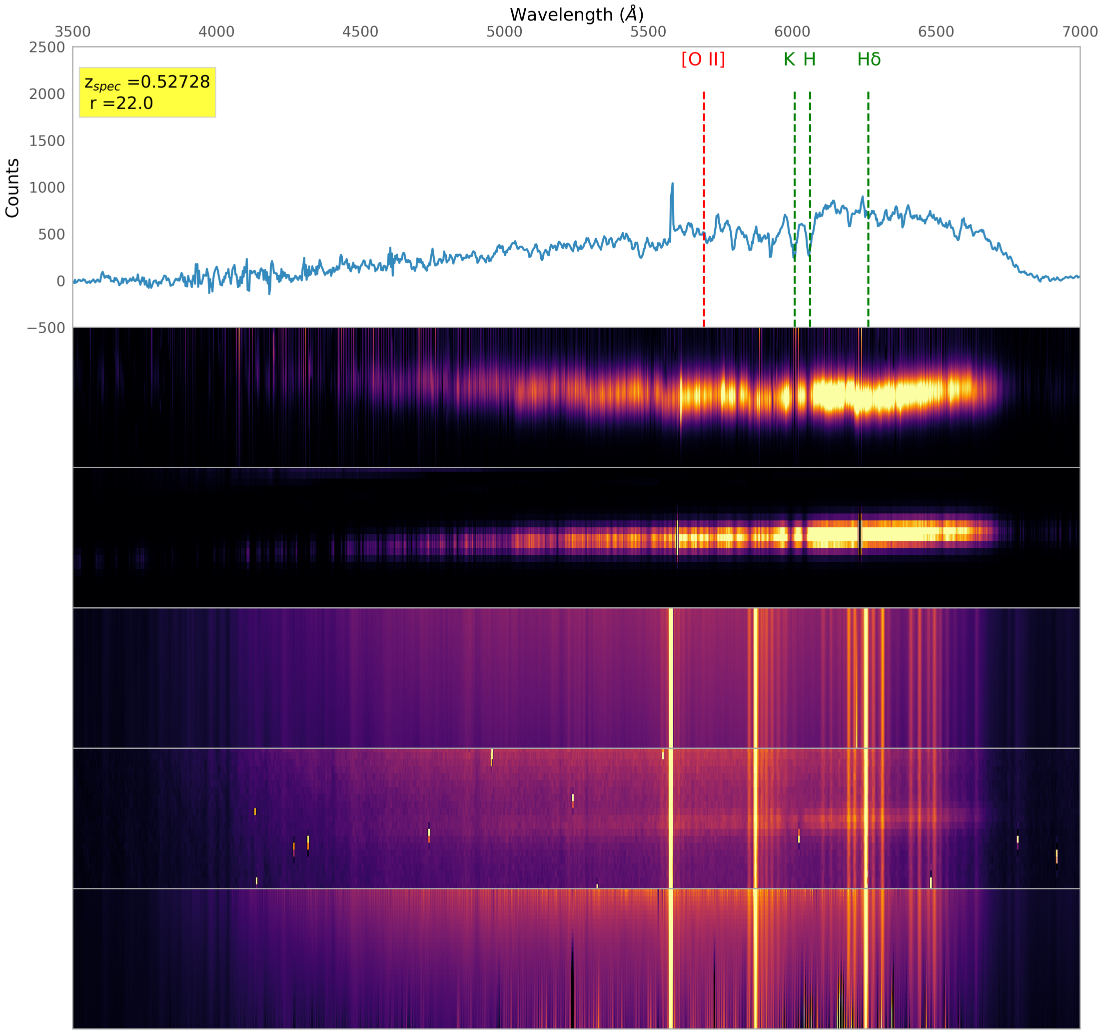

Figure A.21: Object HM_g118. (R.A., Dec. = 247.398146, 43.820813) deg.

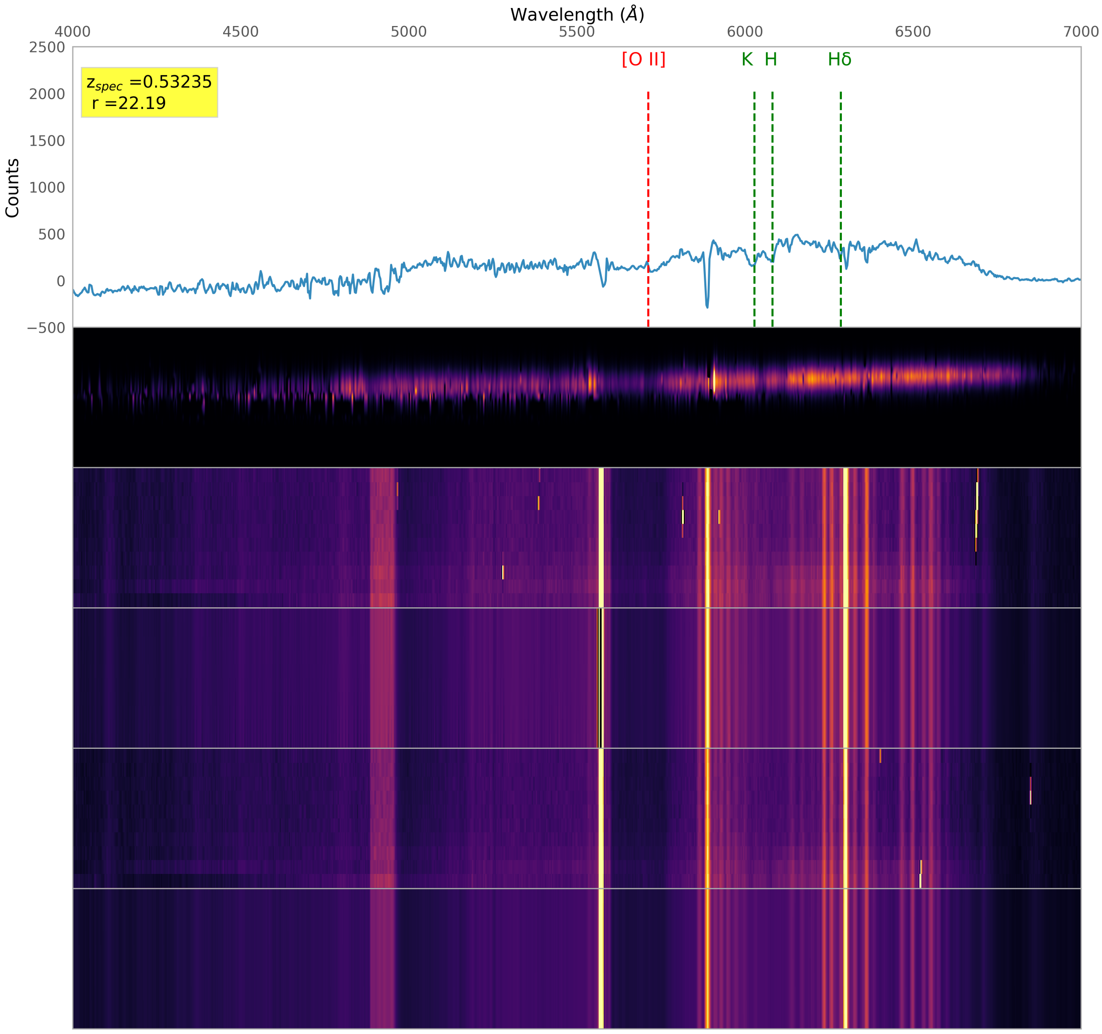

Figure A.22: Object HM_g130. (R.A., Dec. = 247.486052, 43.831115) deg.

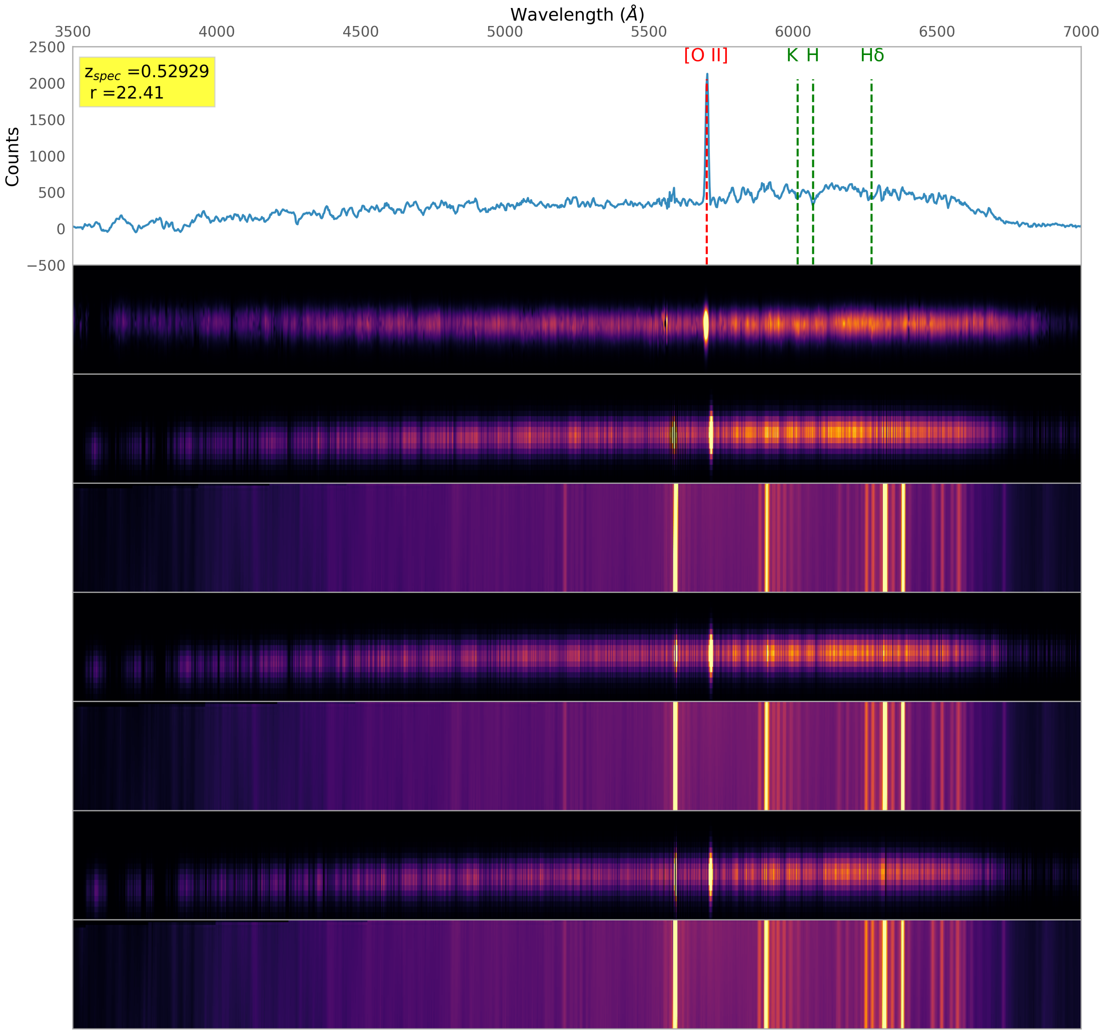

Figure A.23: Object HM_g139. (R.A., Dec. = 247.469968, 43.776610) deg.

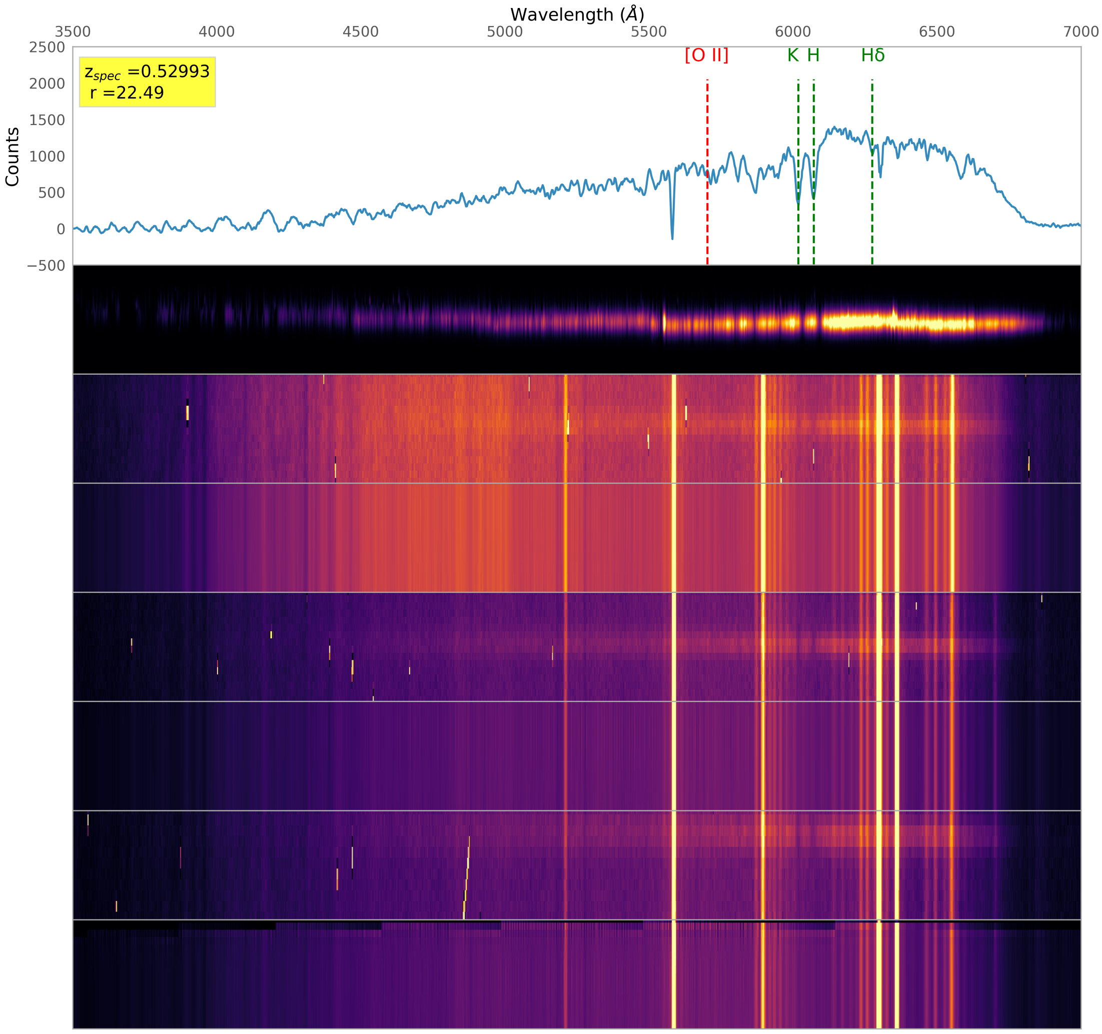

Figure A.24: Object HM_g145. (R.A., Dec. = 247.425366, 43.788531) deg.

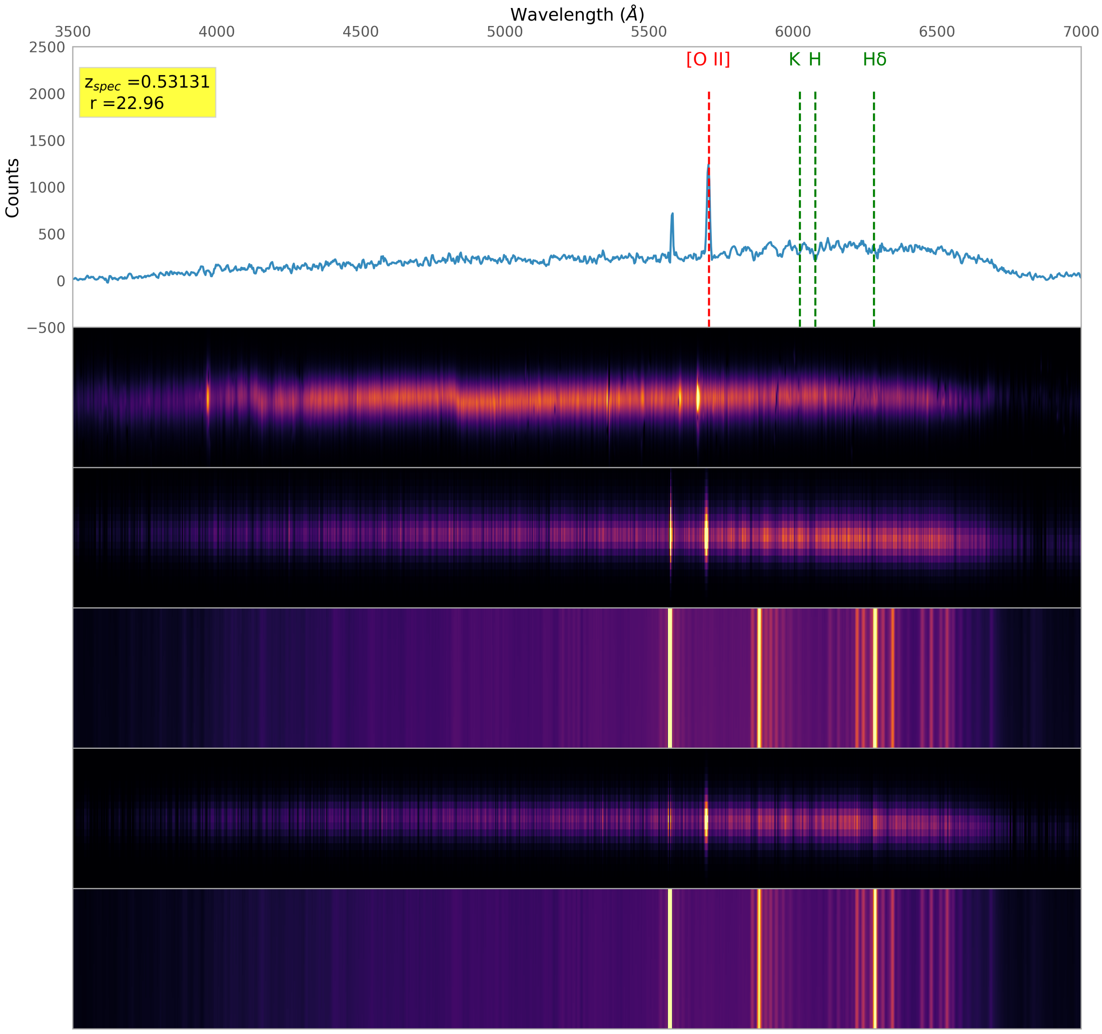

Figure A.25: Object HM_g186. (R.A., Dec. = 247.422468, 43.769037) deg.

Bibliography

Abadi, M. G., Moore, B., & Bower, R. G. 1999, MNRAS, 308, 947, doi: `10.1046/j.1365-8711.1999.02715.x`

Abell, G. O. 1965, ARA&A, 3, 1, doi: `10.1146/annurev.aa.03.090165.000245`

Agnese, R., Anderson, A. J., Asai, M., et al. 2014, Phys. Rev, 112, 241302, doi: `10.1103/PhysRevLett.112.241302`

Aguilar, L. A., & White, S. D. M. 1985, ApJ, 295, 374, doi: `10.1086/163382`

Ahumada, R., Allende Prieto, C., Almeida, A., et al. 2020, ApJS, 249, 3, doi: `10.3847/1538-4365/ab929e`

Aihara, H., Armstrong, R., Bickerton, S., et al. 2018a, PASJ, 70, S8, doi: `10.1093/pasj/psx081`

Aihara, H., Arimoto, N., Armstrong, R., et al. 2018b, PASJ, 70, S4, doi: `10.1093/pasj/psx066`

Aihara, H., AlSayyad, Y., Ando, M., et al. 2022, PASJ, 74, 247, doi: `10.1093/pasj/psab122`

Alberts, S., & Noble, A. 2022, Universe, 8, 554, doi: `10.3390/universe8110554`

Alberts, S., Pope, A., Brodwin, M., et al. 2014, MNRAS, 437, 437, doi: `10.1093/mnras/stt1897`

Andreon, S., Dong, H., & Raichoor, A. 2016, A&A, 593, A2, doi: `10.1051/0004-6361/201628442`

Archambault, S., Behnke, E., Bhattacharjee, P., et al. 2012, Physics Letters B, 711, 153, doi: `10.1016/j.physletb.2012.03.078`

Arkani-Hamed, N., Finkbeiner, D. P., Slatyer, T. R., & Weiner, N. 2009, Phys. Rev. D, 79, 015014, doi: `10.1103/PhysRevD.79.015014`

Arnaud, M. 2009, A&A, 500, 103, doi: `10.1051/0004-6361/200912150`

Arnouts, S., Cristiani, S., Moscardini, L., et al. 1999, MNRAS, 310, 540, doi: `10.1046/j.1365-8711.1999.02978.x`

Astropy Collaboration, Price-Whelan, A. M., Lim, P. L., et al. 2022, ApJ, 935, 167, doi: `10.3847/1538-4357/ac7c74`

Baldry, I. K., Balogh, M. L., Bower, R. G., et al. 2006, MNRAS, 373, 469, doi: `10.1111/j.1365-2966.2006.11081.x`

Baldry, I. K., Glazebrook, K., Brinkmann, J., et al. 2004, ApJ, 600, 681, doi: `10.1086/380092`

Baldry, I. K., Alpaslan, M., Bauer, A. E., et al. 2014, MNRAS, 441, 2440, doi: `10.1093/mnras/stu727`

Balogh, M., Eke, V., Miller, C., et al. 2004a, MNRAS, 348, 1355, doi: `10.1111/j.1365-2966.2004.07453.x`

Balogh, M. L., Baldry, I. K., Nichol, R., et al. 2004b, ApJL, 615, L101, doi: `10.1086/426079`

Balogh, M. L., Morris, S. L., Yee, H. K. C., Carlberg, R. G., & Ellingson, E. 1999, ApJ, 527, 54, doi: `10.1086/308056`

Balogh, M. L., Navarro, J. F., & Morris, S. L. 2000, ApJ, 540, 113, doi: `10.1086/309323`

Bamford, S. P., Nichol, R. C., Baldry, I. K., et al. 2009, MNRAS, 393, 1324, doi: `10.1111/j.1365-2966.2008.14252.x`

Barden, M., Rix, H.-W., Somerville, R. S., et al. 2005, ApJ, 635, 959, doi: `10.1086/497679`

Barkana, R. 2018, Nature, 555, 71, doi: `10.1038/nature25791`

Barkana, R., Haiman, Z., & Ostriker, J. P. 2001, ApJ, 558, 482, doi: `10.1086/322393`

Barnes, D. J., Kay, S. T., Henson, M. A., et al. 2017, MNRAS, 465, 213, doi: `10.1093/mnras/stw2722`

Bartelmann, M. 2010, Class Quantum Gravity, 27, 233001, doi: `10.1088/0264-9381/27/23/233001`

Bartelmann, M., & Schneider, P. 2001, Phys. Rep., 340, 291, doi: `10.1016/S0370-1573(00)00082-X`

Beers, T. C., Flynn, K., & Gebhardt, K. 1990, AJ, 100, 32, doi: `10.1086/115487`

Bellstedt, S., Lidman, C., Muzzin, A., et al. 2016, MNRAS, 460, 2862, doi: `10.1093/mnras/stw1184`

Bennett, C. L., Halpern, M., Hinshaw, G., et al. 2003, ApJS, 148, 1, doi: `10.1086/377253`

Benson, A. J. 2010, Phys. Rep., 495, 33, doi: `10.1016/j.physrep.2010.06.001`

Benson, A. J., & Bower, R. 2011, MNRAS, 410, 2653, doi: `10.1111/j.1365-2966.2010.17641.x`

Berrier, J. C., Stewart, K. R., Bullock, J. S., et al. 2009, ApJ, 690, 1292, doi: `10.1088/0004-637X/690/2/1292`

Bertin, E., & Arnouts, S. 1996, A&AS, 117, 393, doi: `10.1051/aas:1996164`

Bezanson, R., van Dokkum, P. G., Tal, T., et al. 2009, ApJ, 697, 1290, doi: `10.1088/0004-637X/697/2/1290`

Bialas, D., Lisker, T., Olczak, C., Spurzem, R., & Kotulla, R. 2015, A&A, 576, A103, doi: `10.1051/0004-6361/201425235`

Blanton, M. R., & Roweis, S. 2007, AJ, 133, 734, doi: `10.1086/510127`

Blanton, M. R., Hogg, D. W., Bahcall, N. A., et al. 2003, ApJ, 594, 186, doi: `10.1086/375528`

Blumenthal, G. R., Faber, S. M., Primack, J. R., & Rees, M. J. 1984, Nature, 311, 517, doi: `10.1038/311517a0`

Böhringer, H., Schuecker, P., Guzzo, L., et al. 2004, A&A, 425, 367, doi: `10.1051/0004-6361:20034484`

Bois, M., Emsellem, E., Bournaud, F., et al. 2011, MNRAS, 416, 1654, doi: `10.1111/j.1365-2966.2011.19113.x`

Bolzonella, M., Miralles, J. M., & Pelló, R. 2000, A&A, 363, 476, doi: `10.48550/arXiv.astro-ph/0003380`

Borgani, S., & Kravtsov, A. 2011, Advanced Science Letters, 4, 204, doi: `10.1166/asl.2011.1209`

Boselli, A., & Gavazzi, G. 2006, PASP, 118, 517, doi: `10.1086/500691`

Bower, R. G., Benson, A. J., Malbon, R., et al. 2006, MNRAS, 370, 645, doi: `10.1111/j.1365-2966.2006.10519.x`

Brinchmann, J., Charlot, S., White, S. D. M., et al. 2004, MNRAS, 351, 1151, doi: `10.1111/j.1365-2966.2004.07881.x`

Brodwin, M., Stanford, S. A., Gonzalez, A. H., et al. 2013, ApJ, 779, 138, doi: `10.1088/0004-637X/779/2/138`

Bruzual, G., & Charlot, S. 2003, MNRAS, 344, 1000, doi: `10.1046/j.1365-8711.2003.06897.x`

Byrd, G., & Valtonen, M. 1990, ApJ, 350, 89, doi: `10.1086/168362`

Cappellari, M. 2013, ApJL, 778, L2, doi: `10.1088/2041-8205/778/1/L2`

Cassata, P., Cimatti, A., Kurk, J., et al. 2008, A&A, 483, L39, doi: `10.1051/0004-6361:200809881`

Cava, A., Bettoni, D., Poggianti, B. M., et al. 2009, A&A, 495, 707, doi: `10.1051/0004-6361:200810997`

Cavaliere, A., & Fusco-Femiano, R. 1976, A&A, 49, 137

Chabrier, G. 2003, PASP, 115, 763, doi: `10.1086/376392`

Chan, J. C. C., Beifiori, A., Saglia, R. P., et al. 2018, ApJ, 856, 8, doi: `10.3847/1538-4357/aaadb4`

Chen, H., Avestruz, C., Kravtsov, A. V., Lau, E. T., & Nagai, D. 2019, MNRAS, 490, 2380, doi: `10.1093/mnras/stz2776`

Cheung, E., Bundy, K., Cappellari, M., et al. 2016, Nature, 533, 504, doi: `10.1038/nature18006`

Chilingarian, I. V., Melchior, A.-L., & Zolotukhin, I. Y. 2010, MNRAS, 405, 1409, doi: `10.1111/j.1365-2966.2010.16506.x`

Chiu, I., Mohr, J., McDonald, M., et al. 2016, MNRAS, 455, 258, doi: `10.1093/mnras/stv2303`

Choi, E., Somerville, R. S., Ostriker, J. P., Naab, T., & Hirschmann, M. 2018, ApJ, 866, 91, doi: `10.3847/1538-4357/aae076`

Chromey, F. R. 2016, To measure the sky: an introduction to observational astronomy (Cambridge University Press, Cambridge)

Chung, A., van Gorkom, J. H., Kenney, J. D. P., Crowl, H., & Vollmer, B. 2009, AJ, 138, 1741, doi: `10.1088/0004-6256/138/6/1741`

Ciotti, L., Ostriker, J. P., & Proga, D. 2010, ApJ, 717, 708, doi: `10.1088/0004-637X/717/2/708`

Cohn, J. D., & White, M. 2005, Astroparticle Physics, 24, 316, doi: `10.1016/j.astropartphys.2005.07.006`

Cole, S., Lacey, C. G., Baugh, C. M., & Frenk, C. S. 2000, MNRAS, 319, 168, doi: `10.1046/j.1365-8711.2000.03879.x`

Conroy, C., & Gunn, J. E. 2010, ApJ, 712, 833, doi: `10.1088/0004-637X/712/2/833`

Conroy, C., Gunn, J. E., & White, M. 2009, ApJ, 699, 486, doi: `10.1088/0004-637X/699/1/486`

Conroy, C., van Dokkum, P. G., & Kravtsov, A. 2015, ApJ, 803, 77, doi: `10.1088/0004-637X/803/2/77`

Conselice, C. J. 1997, PASP, 109, 1251, doi: `10.1086/134004`

Conselice, C. J. 2014, ARA&A, 52, 291, doi: `10.1146/annurev-astro-081913-040037`

Cooper, M. C., Gallazzi, A., Newman, J. A., & Yan, R. 2010, MNRAS, 402, 1942, doi: `10.1111/j.1365-2966.2009.16020.x`

Cooper, M. C., Griffith, R. L., Newman, J. A., et al. 2012, MNRAS, 419, 3018, doi: `10.1111/j.1365-2966.2011.19938.x`

Copeland, E. J., Sami, M., & Tsujikawa, S. 2006, International Journal of Modern Physics D, 15, 1753, doi: `10.1142/S021827180600942X`

Croton, D. J., Springel, V., White, S. D. M., et al. 2006, MNRAS, 365, 11, doi: `10.1111/j.1365-2966.2005.09675.x`

Daddi, E., Renzini, A., Pirzkal, N., et al. 2005, ApJ, 626, 680, doi: `10.1086/430104`

Damjanov, I., Sohn, J., Geller, M. J., Utsumi, Y., & Dell'Antonio, I. 2023, ApJ, 943, 149, doi: `10.3847/1538-4357/aca88f`

Damjanov, I., Zahid, H. J., Geller, M. J., et al. 2019, ApJ, 872, 91, doi: `10.3847/1538-4357/aaf97d`

Damjanov, I., McCarthy, P. J., Abraham, R. G., et al. 2009, ApJ, 695, 101, doi: `10.1088/0004-637X/695/1/101`

Damjanov, I., Abraham, R. G., Glazebrook, K., et al. 2011, ApJL, 739, L44, doi: `10.1088/2041-8205/739/2/L44`

Dark Energy Survey Collaboration, Abbott, T., Abdalla, F. B., et al. 2016, MNRAS, 460, 1270, doi: `10.1093/mnras/stw641`

Davis, M., Efstathiou, G., Frenk, C. S., & White, S. D. M. 1985, ApJ, 292, 371, doi: `10.1086/163168`

De Lucia, G., & Blaizot, J. 2007, MNRAS, 375, 2, doi: `10.1111/j.1365-2966.2006.11287.x`

de Vaucouleurs, G. 1959, Handbuch der Physik, 53, 275, doi: `10.1007/978-3-642-45932-0_7`

Del Popolo, A., & Le Delliou, M. 2017, Galaxies, 5, 17, doi: `10.3390/galaxies5010017`

Delaye, L., Huertas-Company, M., Mei, S., et al. 2014, MNRAS, 441, 203, doi: `10.1093/mnras/stu496`

DESI Collaboration, Aghamousa, A., Aguilar, J., et al. 2016, arXiv e-prints, arXiv:1611.00036, doi: `10.48550/arXiv.1611.00036`

Dressler, A. 1980, ApJ, 236, 351, doi: `10.1086/157753`

Dubinski, J. 1998, ApJ, 502, 141, doi: `10.1086/305901`

Earl, N., Tollerud, E., O'Steen, R., et al. 2023, astropy/specutils: v1.10.0, v1.10.0, Zenodo, Zenodo, doi: `10.5281/zenodo.7803739`

Ebeling, H., Edge, A. C., & Henry, J. P. 2001, ApJ, 553, 668, doi: `10.1086/320958`

Einasto, M., Deshev, B., Lietzen, H., et al. 2018, A&A, 610, A82, doi: `10.1051/0004-6361/201731600`

Einstein, A. 1917, Sitzungsberichte der Königlich Preußischen Akademie der Wissenschaften (Berlin), 142

Eneev, T. M., Kozlov, N. N., & Sunyaev, R. A. 1973, A&A, 22, 41

Ettori, S., Donnarumma, A., Pointecouteau, E., et al. 2013, Space Sci. Rev., 177, 119, doi: `10.1007/s11214-013-9976-7`

Evrard, A. E., Metzler, C. A., & Navarro, J. F. 1996, ApJ, 469, 494, doi: `10.1086/177798`

Evrard, A. E., Summers, F. J., & Davis, M. 1994, ApJ, 422, 11, doi: `10.1086/173700`

Faber, S. M. 1972, A&A, 20, 361

Faber, S. M., & Gallagher, J. S. 1979, ARA&A, 17, 135, doi: `10.1146/annurev.aa.17.090179.001031`

Fabian, A. C. 1994, ARA&A, 32, 277, doi: `10.1146/annurev.aa.32.090194.001425`

Fabian, A. C. 2003, in Revista Mexicana de Astronomia y Astrofisica Conference Series, Vol. 17, Revista Mexicana de Astronomia y Astrofisica Conference Series, ed. V. Avila-Reese, C. Firmani, C. S. Frenk, & C. Allen, 303–313. `https://arxiv.org/abs/astro-ph/0210150`

Fabricant, D., Fata, R., Roll, J., et al. 2005, PASP, 117, 1411, doi: `10.1086/497385`

Faisst, A. L., Carollo, C. M., Capak, P. L., et al. 2017, ApJ, 839, 71, doi: `10.3847/1538-4357/aa697a`

Fan, X., Narayanan, V. K., Lupton, R. H., et al. 2001, AJ, 122, 2833, doi: `10.1086/324111`

Fan, X., Strauss, M. A., Schneider, D. P., et al. 2003, AJ, 125, 1649, doi: `10.1086/368246`

Feldmann, R., Quataert, E., Hopkins, P. F., Faucher-Giguère, C.-A., & Kereš, D. 2017, MNRAS, 470, 1050, doi: `10.1093/mnras/stx1120`

Ferguson, H. C., Dickinson, M., Giavalisco, M., et al. 2004, ApJL, 600, L107, doi: `10.1086/378578`

Fields, B., Molaro, P., & Sarkar, S. 2014

Fisher, D., Fabricant, D., Franx, M., & van Dokkum, P. 1998, ApJ, 498, 195, doi: `10.1086/305553`

Fouqué, P., Solanes, J. M., Sanchis, T., & Balkowski, C. 2001, A&A, 375, 770, doi: `10.1051/0004-6361:20010833`

Furnell, K. E., Collins, C. A., Kelvin, L. S., et al. 2021, MNRAS, 502, 2419, doi: `10.1093/mnras/stab065`

Gallazzi, A., & Bell, E. F. 2009, ApJS, 185, 253, doi: `10.1088/0067-0049/185/2/253`

Geller, M. J., & Postman, M. 1983, ApJ, 274, 31, doi: `10.1086/161423`

Genel, S., Genzel, R., Bouché, N., Naab, T., & Sternberg, A. 2009, ApJ, 701, 2002, doi: `10.1088/0004-637X/701/2/2002`

Genel, S., Nelson, D., Pillepich, A., et al. 2018, MNRAS, 474, 3976, doi: `10.1093/mnras/stx3078`

George, A. 2020, Master's thesis, Saint Mary's University. `https://library2.smu.ca/handle/01/29427`

George, A., Sawicki, M., & Damjanov, I. in prep.

Giavalisco, M., Steidel, C. C., & Macchetto, F. D. 1996, ApJ, 470, 189, doi: `10.1086/177859`

Gitti, M., Brighenti, F., & McNamara, B. R. 2012, Advances in Astronomy, 2012, 950641, doi: `10.1155/2012/950641`

Gnedin, O. Y. 2003, ApJ, 582, 141, doi: `10.1086/344636`

Gomez, P. 2022, Keck LRIS. `https://www2.keck.hawaii.edu/`

Gómez, P. L., Nichol, R. C., Miller, C. J., et al. 2003, ApJ, 584, 210, doi: `10.1086/345593`

Gonzalez, A. H., Sivanandam, S., Zabludoff, A. I., & Zaritsky, D. 2013, ApJ, 778, 14, doi: `10.1088/0004-637X/778/1/14`

Goto, T., Yagi, M., Tanaka, M., & Okamura, S. 2004, MNRAS, 348, 515, doi: `10.1111/j.1365-2966.2004.07324.x`

Gunn, J. E., & Gott, J. Richard, I. 1972, ApJ, 176, 1, doi: `10.1086/151605`

Guzzo, L. 1997, NewA, 2, 517, doi: `10.1016/S1384-1076(97)00037-7`

Haines, C. P., Gargiulo, A., La Barbera, F., et al. 2007, MNRAS, 381, 7, doi: `10.1111/j.1365-2966.2007.12189.x`

Hamadouche, M. L., Carnall, A. C., McLure, R. J., et al. 2022, MNRAS, 512, 1262, doi: `10.1093/mnras/stac535`

Hatch, N. A., De Breuck, C., Galametz, A., et al. 2011, MNRAS, 410, 1537, doi: `10.1111/j.1365-2966.2010.17538.x`

Hausman, M. A., & Ostriker, J. P. 1978, ApJ, 224, 320, doi: `10.1086/156380`

Hilz, M., Naab, T., & Ostriker, J. P. 2013, MNRAS, 429, 2924, doi: `10.1093/mnras/sts501`

Hinshaw, G., Weiland, J. L., Hill, R. S., et al. 2009, ApJS, 180, 225, doi: `10.1088/0067-0049/180/2/225`

Hinton, S. R., Davis, T. M., Lidman, C., Glazebrook, K., & Lewis, G. F. 2016, Astronomy and Computing, 15, 61, doi: `10.1016/j.ascom.2016.03.001`

Hoekstra, H., Bartelmann, M., Dahle, H., et al. 2013, SSR, 177, 75, doi: `10.1007/s11214-013-9978-5`

Hoffer, A. S., Donahue, M., Hicks, A., & Barthelemy, R. S. 2012, ApJS, 199, 23, doi: `10.1088/0067-0049/199/1/23`

Hogg, D. W. 1999, arXiv e-prints, astro, doi: `10.48550/arXiv.astro-ph/9905116`

Hogg, D. W., Baldry, I. K., Blanton, M. R., & Eisenstein, D. J. 2002, arXiv e-prints, astro, doi: `10.48550/arXiv.astro-ph/0210394`

Hogg, D. W., Eisenstein, D. J., Blanton, M. R., et al. 2005, ApJ, 624, 54, doi: `10.1086/429084`

Hopkins, P. F., Bundy, K., Hernquist, L., Wuyts, S., & Cox, T. J. 2010, MNRAS, 401, 1099, doi: `10.1111/j.1365-2966.2009.15699.x`

Hopkins, P. F., Hernquist, L., Cox, T. J., Keres, D., & Wuyts, S. 2009, ApJ, 691, 1424, doi: `10.1088/0004-637X/691/2/1424`

Horne, K. 1986, PASP, 98, 609, doi: `10.1086/131801`

Howell, S. B. 2000, Handbook of CCD Astronomy (Cambridge University Press, Cambridge)

Hsieh, B. C., & Yee, H. K. C. 2014, ApJ, 792, 102, doi: `10.1088/0004-637X/792/2/102`

Hsieh, B. C., Yee, H. K. C., Lin, H., & Gladders, M. D. 2005, ApJS, 158, 161, doi: `10.1086/429293`

Huchra, J. P., & Geller, M. J. 1982, ApJ, 257, 423, doi: `10.1086/160000`

Huertas-Company, M., Mei, S., Shankar, F., et al. 2013, MNRAS, 428, 1715, doi: `10.1093/mnras/sts150`

Hung, C.-L., & Ebeling, H. 2012, MNRAS, 421, 3229, doi: `10.1111/j.1365-2966.2012.20546.x`

Hwang, H. S., Geller, M. J., Park, C., et al. 2016, ApJ, 818, 173, doi: `10.3847/0004-637X/818/2/173`

Ilbert, O., Arnouts, S., McCracken, H. J., et al. 2006, A&A, 457, 841, doi: `10.1051/0004-6361:20065138`

Ivezić, Ž., Connolly, A. J., VanderPlas, J. T., & Gray, A. 2014, Statistics, Data Mining, and Machine Learning in Astronomy: A Practical Python Guide for the Analysis of Survey Data (Princeton University Press, Princeton), doi: `10.1515/9781400848911`

Jones, A. R. 2018, Probability, statistics and other frightening stuff (Routledge, London)

Jones, C., & Forman, W. 1984, ApJ, 276, 38, doi: `10.1086/161591`

Jørgensen, I., & Chiboucas, K. 2013, AJ, 145, 77, doi: `10.1088/0004-6256/145/3/77`

Jungman, G., Kamionkowski, M., & Griest, K. 1996, Phys. Rep., 267, 195, doi: `10.1016/0370-1573(95)00058-5`

Kamionkowski, M. 1998, in High Energy Physics and Cosmology, 1997 Summer School, ed. E. Gava, A. Masiero, K. S. Narain, S. Randjbar-Daemi, G. Senjanovic, A. Smirnov, & Q. Shafi, Vol. 14, 394, doi: `10.48550/arXiv.hep-ph/9710467`

Kauffmann, G., White, S. D. M., Heckman, T. M., et al. 2004, MNRAS, 353, 713, doi: `10.1111/j.1365-2966.2004.08117.x`

Kauffmann, G., Heckman, T. M., White, S. D. M., et al. 2003, MNRAS, 341, 33, doi: 10.1046/j.1365-8711.2003.06291.x

Kawata, D., & Mulchaey, J. S. 2008, ApJL, 672, L103, doi: 10.1086/526544

Kawinwanichakij, L., Silverman, J. D., Ding, X., et al. 2021, ApJ, 921, 38, doi: 10.3847/1538-4357/ac1f21

Kelly, B. C. 2007, ApJ, 665, 1489, doi: 10.1086/519947

Kenney, J. D. P., van Gorkom, J. H., & Vollmer, B. 2004, AJ, 127, 3361, doi: 10.1086/420805

Khochfar, S., & Silk, J. 2009, MNRAS, 397, 506, doi: 10.1111/j.1365-2966.2009.14958.x

Kim, J. E., & Carosi, G. 2010, Reviews of Modern Physics, 82, 557, doi: 10.1103/RevModPhys.82.557

Kim, K. J., Bayliss, M. B., Noble, A. G., et al. 2022, arXiv e-prints, arXiv:2207.12491. https://arxiv.org/abs/2207.12491

Knowles, K., Cotton, W. D., Rudnick, L., et al. 2022, A&A, 657, A56, doi: 10.1051/0004-6361/202141488

Kormendy, J. 1977, ApJ, 218, 333, doi: 10.1086/155687

Kravtsov, A. V., & Borgani, S. 2012, ARA&A, 50, 353, doi: 10.1146/annurev-astro-081811-125502

Kroupa, P. 2001, MNRAS, 322, 231, doi: 10.1046/j.1365-8711.2001.04022.x

Kuchner, U., Ziegler, B., Verdugo, M., Bamford, S., & Häußler, B. 2017, A&A, 604, A54, doi: 10.1051/0004-6361/201630252

Kurtz, M. J., & Mink, D. J. 1998, PASP, 110, 934, doi: `10.1086/316207`

Lacey, C., & Cole, S. 1993, MNRAS, 262, 627, doi: `10.1093/mnras/262.3.627`

Laporte, C. F. P., White, S. D. M., Naab, T., & Gao, L. 2013, MNRAS, 435, 901, doi: `10.1093/mnras/stt912`

Larson, R. B., Tinsley, B. M., & Caldwell, C. N. 1980, ApJ, 237, 692, doi: `10.1086/157917`

Lauer, T. R., Postman, M., Strauss, M. A., Graves, G. J., & Chisari, N. E. 2014, ApJ, 797, 82, doi: `10.1088/0004-637X/797/2/82`

Lewis, A., & Challinor, A. 2006, Phys. Rep., 429, 1, doi: `10.1016/j.physrep.2006.03.002`

Li, M., Li, X.-D., Wang, S., & Wang, Y. 2011, Communications in Theoretical Physics, 56, 525, doi: `10.1088/0253-6102/56/3/24`

Li, M., Li, Y., Bryan, G. L., Ostriker, E. C., & Quataert, E. 2020a, ApJ, 894, 44, doi: `10.3847/1538-4357/ab86b4`

—. 2020b, ApJ, 898, 23, doi: `10.3847/1538-4357/ab9c22`

Lilly, S., Schade, D., Ellis, R., et al. 1998, ApJ, 500, 75, doi: `10.1086/305713`

Lin, Y.-T., & Mohr, J. J. 2004, ApJ, 617, 879, doi: `10.1086/425412`

Littlefair, S. 2020, Observational Techniques for Astronomers, University of Sheffield. `http://slittlefair.staff.shef.ac.uk/teaching/phy217/lectures/instruments/L12/index.html#darks`

Loh, Y.-S., & Strauss, M. A. 2006, MNRAS, 366, 373, doi: `10.1111/j.1365-2966.2005.09714.x`

Lotz, J. M., Jonsson, P., Cox, T. J., et al. 2011, ApJ, 742, 103, doi: `10.1088/0004-637X/742/2/103`

Lower, S., Narayanan, D., Leja, J., et al. 2020, ApJ, 904, 33, doi: `10.3847/1538-4357/abbfa7`

Mahajan, S., & Raychaudhury, S. 2009, MNRAS, 400, 687, doi: `10.1111/j.1365-2966.2009.15512.x`

Mahajan, S., Raychaudhury, S., & Pimbblet, K. A. 2012, MNRAS, 427, 1252, doi: `10.1111/j.1365-2966.2012.22059.x`

Maltby, D. T., Aragón-Salamanca, A., Gray, M. E., et al. 2010, MNRAS, 402, 282, doi: `10.1111/j.1365-2966.2009.15953.x`

Marchesini, D., van Dokkum, P. G., Förster Schreiber, N. M., et al. 2009, ApJ, 701, 1765, doi: `10.1088/0004-637X/701/2/1765`

Masters, D., & Capak, P. 2011, PASP, 123, 638, doi: `10.1086/660023`

Mateus, A., Sodré, L., Cid Fernandes, R., et al. 2006, MNRAS, 370, 721, doi: `10.1111/j.1365-2966.2006.10565.x`

Mathews, W. G., & Brighenti, F. 2003, ARA&A, 41, 191, doi: `10.1146/annurev.astro.41.090401.094542`

McDonald, M., Veilleux, S., Rupke, D. S. N., Mushotzky, R., & Reynolds, C. 2011, ApJ, 734, 95, doi: `10.1088/0004-637X/734/2/95`

McLure, R. J., Pearce, H. J., Dunlop, J. S., et al. 2013, MNRAS, 428, 1088, doi: `10.1093/mnras/sts092`

McNamara, B. R., & O'Connell, R. W. 1989, AJ, 98, 2018, doi: `10.1086/115275`

Mei, S., Blakeslee, J. P., Côté, P., et al. 2007, ApJ, 655, 144, doi: `10.1086/509598`

Menci, N., Fontana, A., Giallongo, E., & Salimbeni, S. 2005, ApJ, 632, 49, doi: `10.1086/432788`

Mendel, J. T., Simard, L., Ellison, S. L., & Patton, D. R. 2013, MNRAS, 429, 2212, doi: `10.1093/mnras/sts489`

Mitchell, P. D., Lacey, C. G., Baugh, C. M., & Cole, S. 2013, MNRAS, 435, 87, doi: `10.1093/mnras/stt1280`

Mittal, R., Hudson, D. S., Reiprich, T. H., & Clarke, T. 2009, A&A, 501, 835, doi: `10.1051/0004-6361/200810836`

Miyazaki, S., Komiyama, Y., Kawanomoto, S., et al. 2018, PASJ, 70, S1, doi: `10.1093/pasj/psx063`

Mo, H., van den Bosch, F. C., & White, S. 2010, Galaxy Formation and Evolution (Cambridge University Press, Cambridge)

Mobasher, B., Dahlen, T., Ferguson, H. C., et al. 2015, ApJ, 808, 101, doi: `10.1088/0004-637X/808/1/101`

Mohr, J. J., Mathiesen, B., & Evrard, A. E. 1999, ApJ, 517, 627, doi: `10.1086/307227`

Moore, B., Katz, N., Lake, G., Dressler, A., & Oemler, A. 1996, Nature, 379, 613, doi: `10.1038/379613a0`

Morishita, T., Abramson, L. E., Treu, T., et al. 2017, ApJ, 835, 254, doi: `10.3847/1538-4357/835/2/254`

Mosleh, M., Williams, R. J., Franx, M., et al. 2012, ApJL, 756, L12, doi: `10.1088/2041-8205/756/1/L12`

Mowla, L., van der Wel, A., van Dokkum, P., & Miller, T. B. 2019a, ApJL, 872, L13, doi: `10.3847/2041-8213/ab0379`

Mowla, L. A., van Dokkum, P., Brammer, G. B., et al. 2019b, ApJ, 880, 57, doi: `10.3847/1538-4357/ab290a`

Muzzin, A., Wilson, G., Yee, H. K. C., et al. 2012, ApJ, 746, 188, doi: `10.1088/0004-637X/746/2/188`

Naab, T., Johansson, P. H., & Ostriker, J. P. 2009, ApJL, 699, L178, doi: `10.1088/0004-637X/699/2/L178`

Naab, T., Johansson, P. H., Ostriker, J. P., & Efstathiou, G. 2007, ApJ, 658, 710, doi: `10.1086/510841`

Navarro, J. F., Frenk, C. S., & White, S. D. M. 1996, ApJ, 462, 563, doi: `10.1086/177173`

—. 1997, ApJ, 490, 493, doi: `10.1086/304888`

Newman, A. B., Ellis, R. S., Bundy, K., & Treu, T. 2012, ApJ, 746, 162, doi: `10.1088/0004-637X/746/2/162`

Nipoti, C., Treu, T., Auger, M. W., & Bolton, A. S. 2009, ApJL, 706, L86, doi: `10.1088/0004-637X/706/1/L86`

Noble, A. G., Webb, T. M. A., Muzzin, A., et al. 2013, ApJ, 768, 118, doi: `10.1088/0004-637X/768/2/118`

Nulsen, P. E. J. 1982, MNRAS, 198, 1007, doi: `10.1093/mnras/198.4.1007`

O'Dea, C. P., Baum, S. A., Privon, G., et al. 2008, ApJ, 681, 1035, doi: `10.1086/588212`

Oesch, P. A., Bouwens, R. J., Carollo, C. M., et al. 2010, ApJL, 709, L21, doi: `10.1088/2041-8205/709/1/L21`

Oke, J. B., & Sandage, A. 1968, ApJ, 154, 21, doi: `10.1086/149737`

Oke, J. B., Cohen, J. G., Carr, M., et al. 1995, PASP, 107, 375, doi: `10.1086/133562`

Papovich, C., Bassett, R., Lotz, J. M., et al. 2012, ApJ, 750, 93, doi: `10.1088/0004-637X/750/2/93`

Patel, S. G., Holden, B. P., Kelson, D. D., et al. 2012, ApJL, 748, L27, doi: `10.1088/2041-8205/748/2/L27`

Paulino-Afonso, A., Sobral, D., Darvish, B., et al. 2020, A&A, 633, A70, doi: `10.1051/0004-6361/201834244`

Pecaut, M. J., & Mamajek, E. E. 2013, ApJS, 208, 9, doi: `10.1088/0067-0049/208/1/9`

Peccei, R. D., & Quinn, H. R. 1977, Phys. Rev. D, 16, 1791, doi: `10.1103/PhysRevD.16.1791`

Pedregosa, F., Varoquaux, G., Gramfort, A., et al. 2011, Journal of Machine Learning Research, 12, 2825

Peebles, P. J., & Ratra, B. 2003, Reviews of Modern Physics, 75, 559, doi: `10.1103/RevModPhys.75.559`

Peebles, P. J. E. 1993, Principles of Physical Cosmology (Princeton University Press, Princeton), doi: `10.1515/9780691206721`

Peng, C. Y., Ho, L. C., Impey, C. D., & Rix, H.-W. 2002, AJ, 124, 266, doi: `10.1086/340952`

Peng, Y.-j., Lilly, S. J., Kovač, K., et al. 2010, ApJ, 721, 193, doi: `10.1088/0004-637X/721/1/193`

Penzias, A. A., & Wilson, R. W. 1965, ApJ, 142, 419, doi: `10.1086/148307`

Perivolaropoulos, L., & Skara, F. 2022, New Astron. Rev., 95, 101659, doi: `10.1016/j.newar.2022.101659`

Perley, D. A. 2019, PASP, 131, 084503, doi: `10.1088/1538-3873/ab215d`

Piffaretti, R., & Valdarnini, R. 2008, A&A, 491, 71, doi: `10.1051/0004-6361:200809739`

Pillepich, A., Nelson, D., Hernquist, L., et al. 2018, MNRAS, 475, 648, doi: `10.1093/mnras/stx3112`

Planck Collaboration, Ade, P. A. R., Aghanim, N., et al. 2016, A&A, 594, A13, doi: `10.1051/0004-6361/201525830`

Planck Collaboration, Aghanim, N., Akrami, Y., et al. 2020, A&A, 641, A6, doi: `10.1051/0004-6361/201833910`

Planelles, S., & Quilis, V. 2009, MNRAS, 399, 410, doi: `10.1111/j.1365-2966.2009.15290.x`

Poggianti, B. M., Calvi, R., Bindoni, D., et al. 2013, ApJ, 762, 77, doi: `10.1088/0004-637X/762/2/77`

Pojmanski, G. 2002, AcA, 52, 397, doi: `10.48550/arXiv.astro-ph/0210283`

Pospelov, M., Ritz, A., & Voloshin, M. 2008, Physics Letters B, 662, 53, doi: `10.1016/j.physletb.2008.02.052`

Postman, M., & Geller, M. J. 1984, ApJ, 281, 95, doi: `10.1086/162078`

Primack, J. R., & Gross, M. A. K. 2001, in Current aspects of neutrino physics, ed. D. O. Caldwell, 287–308, doi: `10.48550/arXiv.astro-ph/0007165`

Prochaska, J., Hennawi, J., Westfall, K., et al. 2020, The Journal of Open Source Software, 5, 2308, doi: `10.21105/joss.02308`

Profumo, S., Sigurdson, K., & Kamionkowski, M. 2006, Phys. Rev., 97, 031301, doi: `10.1103/PhysRevLett.97.031301`

Raichoor, A., Mei, S., Stanford, S. A., et al. 2012, ApJ, 745, 130, doi: `10.1088/0004-637X/745/2/130`

Ravindranath, S., Ferguson, H. C., Conselice, C., et al. 2004, ApJL, 604, L9, doi: `10.1086/382952`

Rettura, A., Rosati, P., Nonino, M., et al. 2010, ApJ, 709, 512, doi: `10.1088/0004-637X/709/1/512`

Richmond, M. 2002, Dark Subtraction and Flatfielding. `http://spiff.rit.edu/classes/phys445/lectures/darkflat/darkflat.html#dark`

Riess, A. G., Filippenko, A. V., Challis, P., et al. 1998, AJ, 116, 1009, doi: `10.1086/300499`

Rines, K., Geller, M. J., Diaferio, A., & Kurtz, M. J. 2013, ApJ, 767, 15, doi: `10.1088/0004-637X/767/1/15`

Rockosi, C., Stover, R., Kibrick, R., et al. 2010, in Society of Photo-Optical Instrumentation Engineers (SPIE) Conference Series, Vol. 7735, Ground-based and Airborne Instrumentation for Astronomy III, ed. I. S. McLean, S. K. Ramsay, & H. Takami, 77350R, doi: `10.1117/12.856818`

Romer, A. K., Viana, P. T. P., Liddle, A. R., & Mann, R. G. 1999, arXiv e-prints, astro, doi: `10.48550/arXiv.astro-ph/9911499`

Rosati, P., Borgani, S., & Norman, C. 2002a, ARA&A, 40, 539, doi: `10.1146/annurev.astro.40.120401.150547`

—. 2002b, ARA&A, 40, 539, doi: `10.1146/annurev.astro.40.120401.150547`

Rosenblatt, M. 1956, The Annals of Mathematical Statistics, 27, 832 , doi: `10.1214/aoms/1177728190`

Rubin, V. C. 1983, Scientific American, 248, 96, doi: `10.1038/scientificamerican0683-96`

Ryden, B. 2003, Introduction to cosmology (Cambridge University Press, Cambridge,)

Sarazin, C. L. 2002, in Astrophysics and Space Science Library, Vol. 272, Merging Processes in Galaxy Clusters, ed. L. Feretti, I. M. Gioia, & G. Giovannini, 1–38, doi: `10.1007/0-306-48096-4_1`

Schaye, J., Crain, R. A., Bower, R. G., et al. 2015, MNRAS, 446, 521, doi: `10.1093/mnras/stu2058`

Schneider, A., Smith, R. E., & Reed, D. 2013, MNRAS, 433, 1573, doi: `10.1093/mnras/stt829`

Schneider, P. 2006, Extragalactic Astronomy and Cosmology (Springer, New York City)

Schneider, P., & Bartelmann, M. 1995, MNRAS, 273, 475, doi: `10.1093/mnras/273.2.475`

Schweizer, F., & Seitzer, P. 1992, AJ, 104, 1039, doi: `10.1086/116296`

Scott, E. L. 1957, AJ, 62, 248, doi: `10.1086/107529`

Sellwood, J. A. 2014, Reviews of Modern Physics, 86, 1, doi: `10.1103/RevModPhys.86.1`

Sersic, J. L. 1968, Atlas de Galaxias Australes (Cordoba)

Sharp, R., Saunders, W., Smith, G., et al. 2006, in Society of Photo-Optical Instrumentation Engineers (SPIE) Conference Series, Vol. 6269, Ground-based and Airborne Instrumentation for Astronomy, ed. I. S. McLean & M. Iye, 62690G, doi: `10.1117/12.671022`

Shen, S., Mo, H. J., White, S. D. M., et al. 2003a, MNRAS, 343, 978, doi: `10.1046/j.1365-8711.2003.06740.x`

—. 2003b, MNRAS, 343, 978, doi: `10.1046/j.1365-8711.2003.06740.x`

Sijacki, D., & Springel, V. 2006, MNRAS, 366, 397, doi: `10.1111/j.1365-2966.2005.09860.x`

Smith, R., Pacifici, C., Pasquali, A., & Calderón-Castillo, P. 2019, ApJ, 876, 145, doi: `10.3847/1538-4357/ab1917`

Smith, R. J., Hudson, M. J., Lucey, J. R., Nelan, J. E., & Wegner, G. A. 2006, MNRAS, 369, 1419, doi: `10.1111/j.1365-2966.2006.10393.x`

Smoot, G. F., Bennett, C. L., Kogut, A., et al. 1992, ApJL, 396, L1, doi: `10.1086/186504`

Sohn, J., Geller, M. J., Hwang, H. S., et al. 2021a, ApJ, 923, 143, doi: `10.3847/1538-4357/ac29c3`

—. 2021b, ApJ, 909, 129, doi: `10.3847/1538-4357/abd9be`

—. 2023, ApJ, 945, 94, doi: `10.3847/1538-4357/acb925`

Sohn, J., Geller, M. J., Rines, K. J., et al. 2018, ApJ, 856, 172, doi: `10.3847/1538-4357/aab20b`

Sohn, J., Geller, M. J., Zahid, H. J., & Fabricant, D. G. 2019, ApJ, 872, 192, doi: `10.3847/1538-4357/ab0213`

Sparke, L. S., & Gallagher, John S., I. 2007, Galaxies in the Universe: An Introduction (Cambridge University Press, Cambridge)

Spergel, D. N., Verde, L., Peiris, H. V., et al. 2003, ApJS, 148, 175, doi: `10.1086/377226`

Spinrad, H., & Taylor, B. J. 1971, ApJS, 22, 445, doi: `10.1086/190232`

Sprayberry, D. 2002, Keck telescope and facility Instrument Guide, Keck Observatory. `https://www2.keck.hawaii.edu/observing/kecktelgde/ktelinstupdate.pdf`

Springel, V., Pakmor, R., Zier, O., & Reinecke, M. 2021, MNRAS, 506, 2871, doi: `10.1093/mnras/stab1855`

Springel, V., White, S. D. M., Jenkins, A., et al. 2005, Nature, 435, 629, doi: `10.1038/nature03597`

Springel, V., Pakmor, R., Pillepich, A., et al. 2018, MNRAS, 475, 676, doi: `10.1093/mnras/stx3304`

Stanford, S. A., Eisenhardt, P. R., Brodwin, M., et al. 2005, ApJL, 634, L129, doi: `10.1086/499045`

Strateva, I., Ivezić, Ž., Knapp, G. R., et al. 2001, AJ, 122, 1861, doi: `10.1086/323301`

Svrcek, P., & Witten, E. 2006, Journal of High Energy Physics, 2006, 051, doi: `10.1088/1126-6708/2006/06/051`

Sweet, S. M., Sharp, R., Glazebrook, K., et al. 2017, MNRAS, 464, 2910, doi: `10.1093/mnras/stw2411`

Thomas, D., Maraston, C., Schawinski, K., Sarzi, M., & Silk, J. 2010, MNRAS, 404, 1775, doi: `10.1111/j.1365-2966.2010.16427.x`

Tinsley, B. M. 1968, ApJ, 151, 547, doi: `10.1086/149455`

Tonry, J., & Davis, M. 1979, AJ, 84, 1511, doi: `10.1086/112569`

Trujillo, I., Förster Schreiber, N. M., Rudnick, G., et al. 2006, ApJ, 650, 18, doi: `10.1086/506464`

Turner, M. S. 1986, Phys. Rev. D, 33, 889, doi: `10.1103/PhysRevD.33.889`

—. 1988, Phys. Rev. Lett., 60, 1797, doi: `10.1103/PhysRevLett.60.1797`

—. 1990, Phys. Reps., 197, 67

Upadhyay, A. K., Oman, K. A., & Trager, S. C. 2021, A&A, 652, A16, doi: `10.1051/0004-6361/202141036`

Vale, A., & Ostriker, J. P. 2006, MNRAS, 371, 1173, doi: `10.1111/j.1365-2966.2006.10605.x`

Vallés-Pérez, D., Planelles, S., & Quilis, V. 2020, MNRAS, 499, 2303, doi: `10.1093/mnras/staa3035`

van de Sande, J., Kriek, M., Franx, M., et al. 2013, ApJ, 771, 85, doi: `10.1088/0004-637X/771/2/85`

van der Wel, A., Holden, B. P., Zirm, A. W., et al. 2008, ApJ, 688, 48, doi: `10.1086/592267`

van der Wel, A., Franx, M., van Dokkum, P. G., et al. 2014, ApJ, 788, 28, doi: `10.1088/0004-637X/788/1/28`

van Dokkum, P. G. 2001, PASP, 113, 1420, doi: `10.1086/323894`

van Dokkum, P. G., Franx, M., Kriek, M., et al. 2008, ApJL, 677, L5, doi: `10.1086/587874` van Dokkum, P. G., Nelson, E. J., Franx, M., et al. 2015, ApJ, 813, 23, doi: `10.1088/0004-637X/813/1/23`

Vaughan, S. P., Tiley, A. L., Davies, R. L., et al. 2020, MNRAS, 496, 3841, doi: `10.1093/mnras/staa1837`

Vernaleo, J. C., & Reynolds, C. S. 2006, ApJ, 645, 83, doi: `10.1086/504029`

Vikhlinin, A., Kravtsov, A. V., Burenin, R. A., et al. 2009, ApJ, 692, 1060, doi: `10.1088/0004-637X/692/2/1060`

Virtanen, P., Gommers, R., Oliphant, T. E., et al. 2020, Nature Methods, 17, 261, doi: `10.1038/s41592-019-0686-2`

Walcher, J., Groves, B., Budavári, T., & Dale, D. 2011, Ap&SS, 331, 1, doi: `10.1007/s10509-010-0458-z`

Weinberg, S. 2008, Cosmology (Oxford University Press., Oxford)

Wetzel, A. R., Tinker, J. L., Conroy, C., & van den Bosch, F. C. 2013, MNRAS, 432, 336, doi: `10.1093/mnras/stt469`

Whitaker, K. E., Labbé, I., van Dokkum, P. G., et al. 2011, ApJ, 735, 86, doi: `10.1088/0004-637X/735/2/86`

White, M., Zheng, Z., Brown, M. J. I., Dey, A., & Jannuzi, B. T. 2007, ApJL, 655, L69, doi: `10.1086/512015`

White, S. D. M., & Rees, M. J. 1978, MNRAS, 183, 341, doi: `10.1093/mnras/183.3.341`

Wilkins, S. M., Gonzalez-Perez, V., Baugh, C. M., Lacey, C. G., & Zuntz, J. 2013, MNRAS, 431, 430, doi: `10.1093/mnras/stt192`

Williams, R. J., Quadri, R. F., Franx, M., et al. 2010, ApJ, 713, 738, doi: `10.1088/0004-637X/713/2/738`

Wilman, D. J., Fossati, M., Mendel, J. T., et al. 2020, ApJ, 892, 1, doi: `10.3847/1538-4357/ab7914`

Wilson, G., Muzzin, A., Yee, H. K. C., et al. 2009, ApJ, 698, 1943, doi: `10.1088/0004-637X/698/2/1943`

Wong, T., & Blitz, L. 2002, ApJ, 569, 157, doi: `10.1086/339287`

Yang, H. Y. K., & Reynolds, C. S. 2016, ApJ, 829, 90, doi: `10.3847/0004-637X/829/2/90`

Yoon, H., Chung, A., Smith, R., & Jaffé, Y. L. 2017, ApJ, 838, 81, doi: `10.3847/1538-4357/aa6579`

Zwicky, F. 1933, Helvetica Physica Acta, 6, 110

—. 1937, Phys. Rev., 51, 290, doi: `10.1103/PhysRev.51.290`